PHASE MATCHING FOR DIFFERENCE FREQUENCY GENERATION USING NANOSTRUCTURED METAMATERIALS

by

Naser Abdulhavid Otman

Submitted in partial fulfillment of the requirements
for the degree of Doctor of Philosophy

at

Dalhousie University
Halifax, Nova Scotia
May 2020

Table of Content

List of Figures

Abstract

The mid-IR frequency region is highly intriguing due to its transition response to gas molecules. To date, this region has provided numerous applications, such as gas detection, atmospheric monitoring, and environmental trace for toxic vapors. In general, mid-IR frequency sources are more complex to make compared to visible and near-IR sources. To generate mid-IR frequencies from visible or near-IR frequencies, difference frequency generation (DFG) of optical nonlinear frequency conversion is used. This can be done through a material with relatively high nonlinear properties, such as gallium arsenide (GaAs). GaAs is a crystal of semiconductor materials with a broad mid-IR transparency region. The further development of technology has made GaAs the optimal choice for mid-IR generation.

However, one major drawback in using DFG is phase velocity mismatching between interacting waves, which results from optical frequency conversion. Phase-mismatch essentially degrades the conversion efficiency. The anisotropic properties of some nonlinear crystals can overcome the phase-mismatch using birefringent phase matching (BPM). Unfortunately, because GaAs is an isotropic crystal, its lack of anisotropic properties prevents the use of BPM with GaAs. Modifications to the GaAs crystal are thus required through the addition of another material, rendering the modified crystal anisotropic.

If metallic nanowires of silver (Ag) are embedded in GaAs, the composite structure is characterized as a metamaterial with anisotropic properties. The structure is optically characterized by full wave simulation using the finite difference time domain (FDTD) method to compute the refractive indices from the scattering parameters (*S*-parameters) in order to investigate it for phase matching. The resultant phase-matched mid-IR frequencies are broad and tunable from 2.8 μm to 11 μm. The tuning is performed by varying the pump and the signal wavelength.

A structure of GaAs with periodic arrays of longitudinal nanoholes is investigated for phase matching. The refractive indices of the structure are determined from the *S*-parameters using FDTD simulation. The longest wavelength achieved is 16.2229 μm and the shortest is 3.2961 μm. The results of the FDTD simulation are compared with results obtained from the effective medium theory, using the Maxwell Garnett model. The comparison shows excellent agreement.

List of Abbreviations and Symbols Used

DFG	Difference Frequency Generation
SFG	Sum Frequency Generation
SHG	Second Harmonic generation
Mid-IR	Medium Infrared
Near-IR	Near Infrared
BPM	Birefringent Phase Matching
QPM	Quasi Phase Matching
MDPM	Modal Dispersion Phase Matching
PPLN	Periodically Poled Lithium Niobate
KTP	Potassium Titanyl Phosphide
BBO	Barium Borate
GaAs	Gallium Arsenide
InP	Indium Phosphide
AlGaAs	Aluminum Gallium Arsenide
AlAs	Aluminum Arsenide
FDTD	Finite Difference Time Domain
TE	Transverse Electric Field
TM	Transverse Magnetic Field
μm	Micrometers
cm	Centimeters
M	Transfer Matrix
r_{12}	Reflection Coefficient
r_{23}	Reflection Coefficient
t_{12}	Transmission Coefficient
t_{23}	Transmission Coefficient
γ_{eff}	Effective Damping frequency
KV	Kilovolts
nm	Nanometers
A	Absorption

R	Reflections
T	Transmission
Ag	Silver
o-waves	Ordinary Waves
e-waves	Extraordinary Waves
S-Parameters	Scattering Parameters
Re	Real
Im	Imaginary
$E_{\parallel}$	Parallel Electric Field
$E_{\perp}$	Orthogonal Electric Field
λ_p	Plasma Wavelength
f_p	Plasma frequency
ω_p	Plasma frequency
λ	Wavelength
P^{NL}	Nonlinear Polarization
P^{L}	Linear Polarization
$n^{\parallel}$	Parallel Refractive Index
$n^{\perp}$	Orthogonal Refractive Index
$\chi^{(2)}_{xyz}$	Second Order Nonlinear Coefficient
ε	Electric Permittivity
μ	Magnetic Permeability
Z	Wave Impedance
$\varepsilon^{\parallel}$	Parallel Permittivity
$\varepsilon^{\perp}$	Orthogonal Permittivity
ε_{GaAs}	Primitivity of Gallium Arsenide
ε_{Ag}	Permittivity of Silver
c	Speed of Light
ε_o	Permittivity of the free space
σ_{Ag}	Silver Conductivity
d	Wires and Holes Period

r	Hole Radius
a	Wire Radius
E_p	Pump Electric Field
E_s	Signal Electric Field
E_i	Idler Electric field
$\parallel$	Parallel
$\perp$	Orthogonal
n_p	Pump Wave Refractive Index
n_s	Signal Wave Refractive index
n_i	Idler Wave Refractive index
λ_p	Pump Wave Wavelength
λ_s	Signal Wave Wavelength
λ_i	Idler Wave Wavelength
k_p	Pump Wave Wavenumber
k_s	Signal Wave Wavenumber
k_i	Idler Wave Wavenumber
ω_p	Pump Wave Frequency
ω_s	Signal Wave Frequency
ω_i	Idler Wave Frequency
ε_{eff}	Effective Permittivity
n_{eff}	Effective Refractive Index
k	Wavenumber
L	Length
S_{11}	Scattering Parameter
S_{21}	Scattering Parameter
Δk	Phase Mismatch
η	Efficiency
I_p	Pump Wave Intensity
p_s	Signal Wave Power
p_i	Idler Wave Power

d_{eff}	Contracted Symbol for Nonlinear Coefficient
eff	Effective
α_p	Absorption Coefficient for Pump Wave
α_s	Absorption Coefficient for Signal Wave
α_i	Absorption Coefficient for Idler Wave
N	Integer Number
m	Integer Number
q	Depolarization Factor

Acknowledgements

I would like to thank my supervisor Dr. Michael Cada for his support throughout my PhD research. I am very grateful to him for providing me and the rest of our group with the most advanced CAD tools through his CMC Microsystems subscription. Without these CAD tools, we could not have succeeded in achieving our research results. In addition, I would like to acknowledge CMC Microsystems in Kingston, Canada, for providing the RSoft FullWAVE® Component Design Suite that facilitated my research, and the Government of Canada for its support of CMC Microsystems. I am also obliged to my committee members Dr. Guy Kember and Dr. Yuan Ma and would like to thank Dalhousie University for providing us access to thousands of recent books and research articles.

Chapter 1

Introduction

1.1 Preface

In this work, we investigate the possibility of achieving phase matching between three waves interacting nonlinearly by using the birefringent phase-matching (BPM) method in the nonlinear medium of gallium arsenide (GaAs), and by using nanostructure metamaterials to generate difference frequency generated (DFG) outcomes in the mid-IR spectrum region.

1.2 Introduction

Difference frequency generation (DFG) results from a three-wave nonlinear interaction process that occurs within an optical material exposed to very intense light. It is one of two possible results of the interaction, the other one being sum frequency generation (SFG). As one of the most important applications of nonlinear optics, DFG was first theoretically investigated in 1962 [1]. Nonlinear optics became possible after the discovery of the laser in 1960. Second-harmonic generation (SHG), which is a special case of SFG, was the first experiment performed in nonlinear optics [2]. The mid-IR frequencies spectrum region is more complex to generate using ordinary laser sources than the near-IR and visible spectrum region. DFG is an optical frequency conversion and is often used to generate mid-IR. The mid-IR spectral region from 3 μm to 20 μm is the vibration-transition region for many molecules, making this spectral region highly attractive in spectroscopy [3], [4].

Nonlinear optical conversions are generally very weak due to the small values of the nonlinear coefficients of materials. The conversion efficiency using DFG was studied in 1968 by [5]. They found that increasing the crystal length along the propagating direction of the interacting waves will increase the interaction volume while also increasing the conversion efficiency. However, phase-mismatch between the interacting waves impairs conversion efficiency. The phase-mismatch is a result of different waves with different frequencies traveling through a dispersive optical medium.

Phase matching, which involves momentum conservation of the photons, is an

important aspect to consider in nonlinear optical frequency conversions. In general, phase matching requires the medium to be a non-dispersive material. If the materials are dispersive, anisotropic properties of some nonlinear crystals might be used to overcome the phase-mismatch, using a birefringent phase-matching (BPM) method [6], [7]. BPM relies on the refractive index of the crystal to be different for different wave polarizations and propagations relative to crystal lattice axes. In this way, the phase-mismatched waves will propagate with different polarizations of different associated refractive indices in order to compensate the phase-mismatch.

Quasi-phase matching (QPM) is an alternative technique to birefringent phase matching[8], [9]. In QPM, the sign of the nonlinearity coefficient $\chi^{(2)}$ is modulated periodically positive and negative along the propagating directing of the interacting waves. Another technique for phase matching that is used only for waveguide nonlinear medium is modal dispersion phase matching (MDPM). Different nonlinear media use BPM and QPM, such as periodically poled lithium niobate (PPLN), potassium titanyl phosphate (KTP), and barium borate (BBO). Most DFG based on parametric wavelength conversion uses nonlinear crystals (e.g., PPLN, KTP, BBO) and lithium niobate [10], [11].

Semiconductor materials of relatively high nonlinear dielectric coefficient are alternatives for optical frequency conversion, such as GaAs and InP [12], [13]. GaAs with large second-order susceptibility $\chi^{(2)}$ and a wide transparent infrared optical window (from 1 μm to 17 μm) is a better selection for difference frequency generation in mid-IR frequencies generation [14]. Despite these advantages, it is not possible to use birefringence phase-matching techniques with GaAs or InP, due to their isotropic properties.

There are other methods for achieving phase matching in III-V semiconductors with a cubic lattice structure for difference frequency generation, such as quasi-phase matching, modal phase matching, domain-disordered quasi-phase matching, and suspended GaAs waveguides [15]–[18]. Tunable emissions from 6.7 μm to 12.7 μm have been demonstrated in a nonguided orientation patterned GaAs [19], and the longest wavelength was generated through DFG in an AlGaAs waveguide from 7.5 μm to 8.5 μm [20].

Phase matching using artificial anisotropy is possible if a strongly anisotropic structure can be obtained. Artificial birefringence using multi-layered GaAs/AlAs was first proposed

by J. P. van der Ziel [21]. Relatively large birefringence has been demonstrated with the multilayer structure of oxidized GaAs/AlAs [22]. Phase matching has been achieved for parametric amplification of down conversion by using artificial birefringence in multilayer waveguides of oxidized GaAs/AlAs[23]. Phase matching has also been demonstrated for a DFG by using artificial birefringence with a multilayer structure of GaAs/Al_x Ga_{1-x} As with three layers of Al_x Ga_{1-x} As and one layer of GaAs [24]. Obtaining a large birefringence or a strongly anisotropic structure has been challenging. The use of an optical metamaterial with metallic nanowires is an alternative method of obtaining a strongly anisotropic structure [25]–[29]

In the present research, we perform a theoretical investigation for the phase-matching aspect of DFG in two different nanostructure metamaterial media of GaAs as the host material, with inclusions of periodic arrays of silver nanowires and nanoholes to generate mid-infrared wavelengths (terahertz frequencies).

1.3 Thesis Objectives and Contributions

The first goal in the present study is to find a composite structure of GaAs as a nonlinear material with another material to make a uniaxial anisotropic medium in order to compensate the phase-mismatch that arises in the DFG process caused by dispersive and isotropic properties of GaAs. The difference frequency generation of three wave-mixing processes is one of the methods used to generate mid-IR frequencies. GaAs that possesses a relatively high nonlinearity coefficient and near- and mid-IR transparency regions are a good choice for the mid-IR generation using the DFG method.

The second goal, after a suitable structure has been selected, is to meet the requirements that the generated mid-IR frequencies should be frequency-tunable and cover the entire mid-IR transparency spectrum of GaAs.

As well, we theoretically characterize and investigate a nanostructure of GaAs and silver nanowires from the scattering parameters using an FDTD simulation. The study shows that the composite structure behaves as a uniaxial anisotropic medium, with a transparency region at near-IR spectrum for the electric field parallel to the wires, and transparency at near- and mid-IR for electric fields orthogonal to the wires. Phase matching is achieved in the structure of DFG for three-wave-mixing processes, generating waves of

mid-IR frequencies from two interacting waves of near-IR frequencies. The resultant generated mid-IR is broad and tunable by adjusting the two near-IR frequencies.

Further, the nanostructure of GaAs with nanoholes is characterized and investigated for phase matching of DFG for three wave-mixing processes. The study shows the structure promises very broad and tunable generated mid-IR frequencies.

1.4 Thesis Organization

The thesis presents a combination of nonlinear optics, especially DFG, as well as optical metamaterial structures.

Chapter 2 discusses nonlinear optics and its application of frequency conversion, coupled wave equations for DFG, and methods used to overcome the phase-mismatch of optical frequency conversions, such as birefringent phase matching and quasi-phase matching methods.

Chapter 3 is devoted to optical metamaterial, specifically principles and applications. It includes a description of the type of structures used in this work.

Chapter 4 covers linear optical properties as well as refractive and absorption indices of a composite metamaterial structure of GaAs and silver nanowires. The structure is characterized using scattering parameters computed by FDTD simulation and a retrieving method to determine the linear properties from the scattering parameters.

Chapter 5 shows how GaAs and silver nanowire structure satisfies the phase matching for DFG of three wave-mixing processes. It explains the proper selection of the polarizations of the three interacting waves in such a way as to minimize the ohmic loss of the metal wires.

Chapter 6 introduces another structure of GaAs with nanoholes. FDTD simulation is used to characterize this structure, showing how it is a more suitable option than GaAs/silver structure for use as a uniaxial anisotropic structure and to compensate phase-mismatch.

Chapter 7 provides a summary of the study's achievements in relation to the thesis' objectives, and suggests possible research directions for future work.

Chapter 2

Nonlinear Optics

2.1 Introduction

In most cases, the optical response of optical materials to non-high intense light is linear, such as refraction, absorption or scattering, whereas when the light has a very high intensity, a nonlinear response arises, producing frequency conversion. The nonlinear coefficient $\chi^{(2)}$ is very small compared to the linear coefficient $\chi^{(1)}$. When an optical field is applied to materials, dipole moments of atoms or molecules are created, making the material polarized. If the applied field E is not very high, it will result in linear polarization P^L:

$$P^L = \varepsilon_o \chi^{(1)} E \tag{2.1}$$

where $\chi^{(1)}$ is the ordinary or linear susceptibility. If the optical electric field is too high, nonlinear polarization P^{NL} will arise, and the medium will be linearly and nonlinearly polarized. The scalar form of the total polarization P^T is [30]:

$$P^T = P^L + P^{NL} = \varepsilon_o\left(\chi^{(1)}E + \chi^{(2)}EE + \chi^{(3)}EEE + \cdots.\right) \tag{2.2}$$

The displacement current D is related to the total polarization by:

$$D = \varepsilon_o E + P^T \tag{2.3}$$

If we assume the medium is nonmagnetic ($\mu = \mu_o$) and source-free ($\rho_v = J = 0$), the polarization P^T, the optical field E, and the medium constitutes (ε_o, μ_o) are related by Maxwell's equations:

$$\nabla \times \mathrm{E} = -\mu_o \frac{\partial H}{\partial t} \tag{2.4}$$

$$\nabla \times \mathrm{H} = -\frac{\partial(\varepsilon_o E + P^T)}{\partial t} \tag{2.5}$$

We can then take the curl of Eq. (2.4) and apply Eq. (2.5) into the resultant equation:

$$\nabla \times (\nabla \times \mathrm{E}) = -\mu_o \frac{\partial}{\partial t}\left[\frac{\partial(\varepsilon_o E + P^T)}{\partial t}\right] \tag{2.6}$$

Next, we can substitute $P^T = \varepsilon_o \chi^{(1)} E + P^{NL}$ into Eq. (2.6):

$$\nabla \times (\nabla \times \mathrm{E}) + \varepsilon_r \varepsilon_o \mu_o \frac{\partial^2 E}{\partial t^2} = -\mu_o \frac{\partial^2 P^{NL}}{\partial t^2} \tag{2.7}$$

where $\varepsilon_r = 1 + \chi^{(1)}$ is the relative permittivity of materials. If we substitute $\varepsilon_o \mu_o = 1/c^2$, where c is the speed of light, we get:

$$\nabla \times (\nabla \times \mathrm{E}) + \frac{\varepsilon_r}{c^2}\frac{\partial^2 E}{\partial t^2} = -\frac{1}{\varepsilon_o c^2}\frac{\partial^2 P^{NL}}{\partial t^2} \tag{2.8}$$

Equation (2.8) is the general wave equation of nonlinear optics. It can be simplified based on some special assumptions. The left-hand side of Eq. (2.8) can be written as:

$$\nabla \times (\nabla \times \mathrm{E}) = \nabla(\nabla \cdot E) - \nabla^2 E \tag{2.9}$$

The term $\nabla \cdot E$ on the right-hand right can be ignored for the assumption of the transverse field of infinite plane waves or slow varying amplitude approximation [6], [30], [31]. However, the nonlinear wave equation in (2.8) can simplified as:

$$\nabla^2 E - \frac{\varepsilon_r}{c^2}\frac{\partial^2 E}{\partial t^2} = \frac{1}{\varepsilon_o c^2}\frac{\partial^2 P^{NL}}{\partial t^2} \tag{2.10}$$

2.2 Coupled Wave Equations for DFG

Difference frequency generation (DFG) is a process of interaction of three waves. Two of them are applied and the third one is generated. The two applied waves are named, by convention, the pump and the signal waves, with frequencies of ω_p and ω_s, respectively. The generated wave is referred to as an idler wave of frequency ω_i, where $\omega_i = \omega_p - \omega_s$ and $\omega_p > \omega_s > \omega_i$. Also, sum frequency generation (SFG) can be achieved depending on how the conservation of photon momentum is satisfied. Figure 2.1 illustrates the DFG schematically.

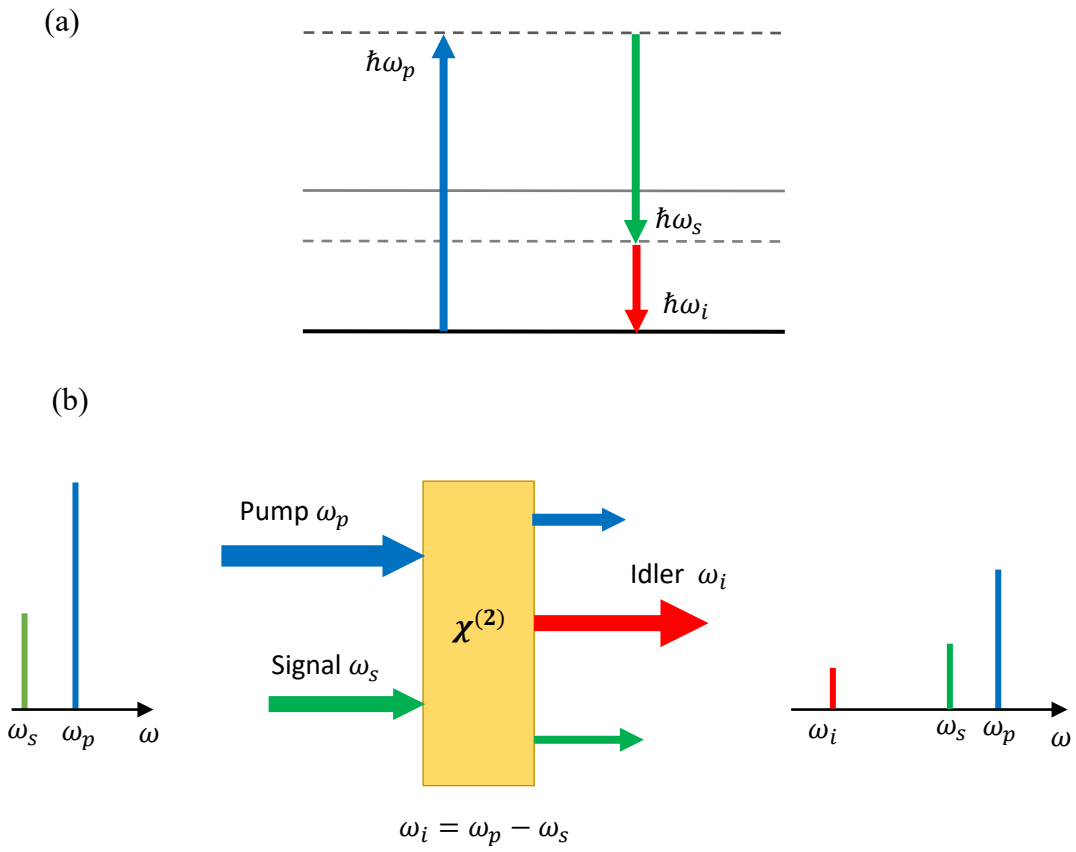

Figure 2.1: (a) Energy diagram describing DFG; (b) geometry of DFG

We can rewrite the scalar form of the total polarization, linear and nonlinear, given in Eq. (2.2) in a vectoral and tensor form, ignoring the third-order susceptibility response, as:

$$P_a^T = P_a^L + P_a^{NL} = \varepsilon_o\left[\sum_b \chi_{ab}^{(1)} E_b + \sum_{bc} \chi_{abc}^{(2)} E_b E_c\right] \tag{2.11}$$

where a, b, and c are geometrical axes of the coordinate system. If a nonlinear medium is excited with a pump wave of frequency ω_p, an electric field E_p, a signal wave of frequency ω_s, and an electric field E_s, the generated nonlinear polarization for the DFG will oscillate

with a frequency of ω_i. From Eq. (2.11), we can write the generated nonlinear polarization for the difference frequency as:

$$P_a^{NL}(\omega_i) = \varepsilon_o\left[\chi_{abc}^{(2)}E_b(\omega_p)E_c^*(\omega_s) + \chi_{abc}^{(2)}E_b^*(\omega_s)E_c(\omega_p)\right] \tag{2.12}$$

If, for simplicity's sake, an effective second-order susceptibility $\chi_{eff}^{(2)}$ is used along all the coordinates axes and a special case of the pump and signal waves are parallel, Eq. (2.12) can be rewritten in the following form by replacing $\chi_{eff}^{(2)}$ with the most common contracted form of d_{eff}, where $\chi_{eff}^{(2)} = 2d_{eff}$:

$$P^{NL}(\omega_i) = 4\varepsilon_o d_{eff}E_pE_s^* \tag{2.13}$$

If the idler wave with frequency ω_i propagates along the $+z$ direction, then the solution of the wave equation (2.10), in the absence of the nonlinear polarization, is:

$$E_i(z,t) = A_i e^{j(k_i z-\omega_i t)} + \text{c. c.} \tag{2.14}$$

where A_i and k_i are the amplitude and the wavenumber of the idler wave, respectively,

$$k_i = \frac{n_i\omega_i}{c} \tag{2.15}$$

and where n_i is the refractive index of the medium at the idler wave frequency ω_i. A similar solution will work for the applied waves, the pump and the signal:

$$E_p(z,t) = A_p e^{j(k_p z-\omega_p t)} + \text{c. c.} \tag{2.16}$$

$$E_s(z,t) = A_s e^{j(k_s z-\omega_s t)} + \text{c. c.} \tag{2.17}$$

where A_p and A_s are the amplitudes of the pump and signal waves, respectively, and k_p and k_s are the wavenumbers of the pump and the signal waves, respectively:

$$k_p = \frac{n_p\omega_p}{c} \tag{2.18}$$

$$k_s = \frac{n_s\omega_s}{c} \tag{2.19}$$

Here, n_p and n_s denote the refractive indices of the nonlinear medium at the frequencies ω_p and ω_i, respectively. The nonlinear polarization $P^{NL}(\omega_i)$ in Eq. (2.13) can be rewritten after applying Eq. (2.16) and Eq. (2.17) into Eq. (2.13), where $\omega_i = \omega_p - \omega_s$ and $\omega_i > \omega_p > \omega_s$:

$$P^{NL}(\omega_i) = 4\varepsilon_o d_{eff} A_p A_s^* e^{j[(k_p - k_s)z - \omega_i t]} + \text{c. c.} \tag{2.20}$$

Next, we can substitute Eqs. (2.20) and (2.14) into the wave equation (2.10). Using only d^2/dz^2 (because the fields depend only on the z coordinate), the resultant wave equation after omitting the time dependence is:

$$\frac{d^2 A_i}{dz^2} + 2jk_i \frac{dA_i}{dz} = \frac{-4\omega_i^2 d_{eff}}{c^2} A_p A_s^* e^{j(k_p - k_s - k_i)z} \tag{2.21}$$

The first term on the left-hand side of Eq. (2.21) can be neglected under the approximation of slowly varying amplitude [6]:

$$\left|\frac{d^2 A_i}{dz^2}\right| \ll \left|2jk_i \frac{dA_i}{dz}\right| \tag{2.22}$$

Equation (2.21) can be rewritten after the approximation as:

$$\left[\frac{dA_i}{dz}\right] = \frac{2jd_{eff}^{(2)}\omega_i^2}{c^2 k_i} A_p A_s^* e^{\mathrm{j}\Delta kz} \tag{2.23}$$

where Δk is the phase or momentum mismatch between the three interacting waves

$$\Delta k = k_p - k_s - k_i \tag{2.24}$$

by integrating Eq. (2.23) from 0 to the L, where L is the propagation length, we get:

$$A_i = \frac{2jd_{eff}\omega_i^2 A_p A_s^*}{c^2 k_i}\left(\frac{e^{\mathrm{j}\Delta kL} - 1}{\mathrm{j}\Delta kL}\right) \tag{2.25}$$

Next, by squaring both sides of Eq. (2.25) and replacing the squares of amplitudes A_i^2, A_p^2, and A_s^2 by I_i, I_p and I_s, based on the relation $I = 2n\varepsilon_o c|A|^2$, the resultant equation is [6]:

$$I_i = \frac{8d_{eff}\omega_i^2 I_p I_s}{n_i n_p n_s \varepsilon_o c^2} L^2 \mathrm{sinc}^2\left(\frac{\Delta kL}{2\pi}\right) \tag{2.26}$$

The efficiency η of the DFG can be defined as:

$$\eta = \frac{I_i}{I_s} = \frac{8d_{eff}\omega_i^2 I_p}{n_i n_p n_s \varepsilon_o c^2} L^2 \mathrm{sinc}^2\left(\frac{\Delta kL}{2\pi}\right) \tag{2.27}$$

The efficiency η of the difference generation system is dependent on the phase-mismatch Δk through the sinc function by the factor $\mathrm{sinc}^2(\Delta kL/2\pi)$, as shown in Fig. (2.2).

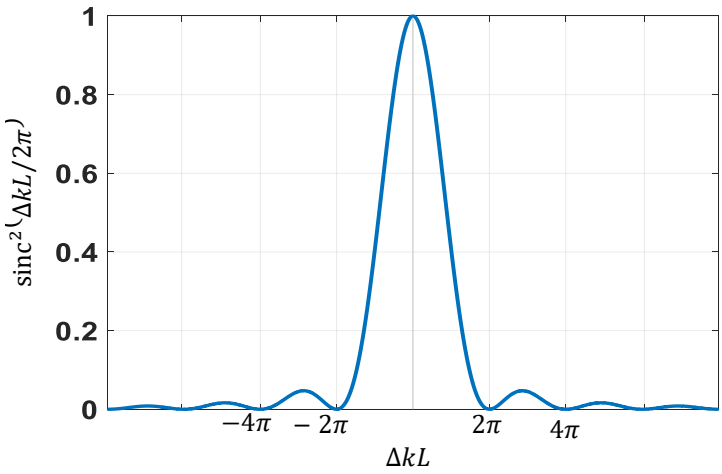

Figure 2.2: $\mathrm{Sinc}(\Delta kL/2\pi)$ factor by which the generated wave intensity I_i is reduced.

If we consider the collinear interaction where the three interacting waves propagate in the same directions, then the phase-mismatch for the DFG can be written after applying Eqs. (2.15), (2.18), and (2.19) into Eq. (2.24) as:

$$\Delta k = \frac{1}{c}\left(n_p\omega_p - n_s\omega_s - n_i\omega_i\right) \tag{2.28}$$

Note that the DFG conversion must satisfy the photon energy conservation law as well:

$$\omega_i = \omega_p - \omega_s \tag{2.29}$$

I_i will increase if the interacting waves travel at the same velocity or are phase-matched ($\Delta k = 0$). If the phase matching is not satisfied ($\Delta k \neq 0$), the accumulated energy of the

DFG wave (idler wave) will be transferred back to the pump and signal waves as they travel through the medium. The idler wave intensity will fluctuate between maximum and zero as a kind of oscillation. Figure (2.3) illustrates how the generated wave intensity increases at phase matching and oscillates between maximum and zero when phase matching is not satisfied. The idler intensity reaches its first maximum at a certain length (called the coherence length [30] L_{coh}) before declining again to zero:

$$L_{coh} = \pi/|\Delta k| \tag{2.30}$$

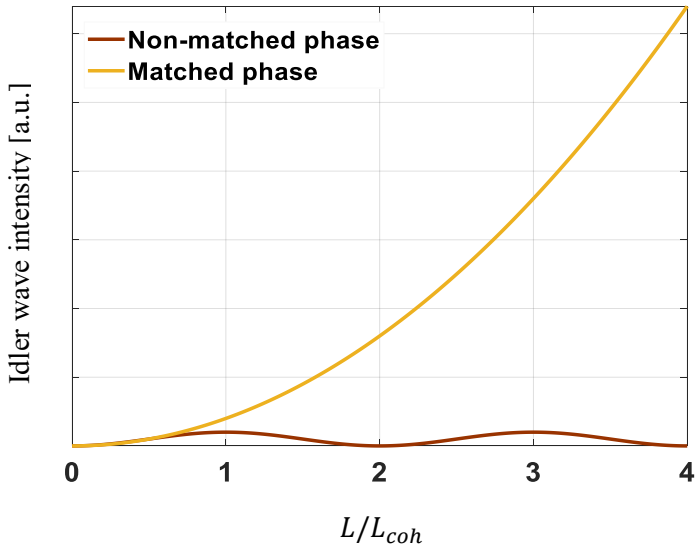

Figure 2.3: Idler wave intensity as a function of propagation length L. In non-matched phase cases, the energy flows backward and forward between the idler and the applied waves and the pump and the signal every $2L_{coh}$. In the matched phase case, the intensity increases with the propagation length L.

Although phase matching can be achieved where the medium is not dispersive in such a manner as $n_p = n_s = n_i$, most crystals in nature are dispersive.

2.3 Phase Matching

Phase matching is achieved only if the three interacting waves travel at the same velocity. Unfortunately, this will occur only if the nonlinear medium is nondispersive. There are two

main methods to overcome phase mismatching: birefringence phase matching (BPM) and quasi-phase matching (QPM).

2.3.1 Birefringent Phase Matching (BPM)

This method uses the anisotropic properties of nonlinear crystals, such as uniaxial or biaxial properties, to compensate the phase-mismatch caused by the dispersion. The crystals are usually characterized by three principal indices n_x, n_y, and n_z along three principal axes x, y, and z, respectively. If the crystal is uniaxial, it is characterized by two equal principal indices, known as ordinary indices n_o, $n_o = n_x = n_y$, while the third one (which is different) is known as the extraordinary index n_e, $n_e = n_z$, where $n_e \neq n_o$. The waves associated with n_e are called extraordinary waves (e-waves), while the waves associated with n_o are called ordinary waves (o-waves).

Let us consider a second-harmonic generation wave as the simplest example to show how the anisotropic properties of dispersive crystal would overcome a phase-mismatch. An efficient second-harmonic wave with a frequency of ω_2 can be generated from a wave of fundamental frequency $\omega_1$if the energy and momentum conservation laws $\omega_2 = 2\omega_1$ and $\omega_2 n(\omega_2) = 2\omega_1 n(\omega_1)$, respectively, are satisfied. If the crystal is dispersive and isotopic, as shown in Fig. 2.4(a), it is not possible to fulfill the momentum condition, since $n(\omega_2) \neq n(\omega_1)$, but the anisotropic properties in Fig. 2.4(b) would satisfy the condition as $n(\omega_2) = n(\omega_1)$. In such cases, the fundamental wave is an e-wave and the second-harmonic wave is an o-wave. The same situation can be applied to the DFG phase-matching condition. There are two main classification for DFG phase matching: type I is where the idler and the signal waves are parallel, and type II is where the idler and the signal are orthogonal. Equations (2.31) and (2.32) denote the momentum conservation conditions for DFG and apply type I and type II phase matching, respectively.

$$\omega_i n_o(\omega_i) = \omega_p n_e(\omega_p) - \omega_s n_o(\omega_s) \tag{2.31}$$

$$\omega_i n_o(\omega_i) = \omega_p n_o(\omega_p) - \omega_s n_e(\omega_s) \tag{2.32}$$

Equations (2.31) and (2.32) can be satisfied by tuning the pumping frequency ω_p or the signal frequency ω_s, or by adjusting the crystal temperature or the incident angle of the pump wave with respect to the optic axis of crystal [7], [30], [32], [33].

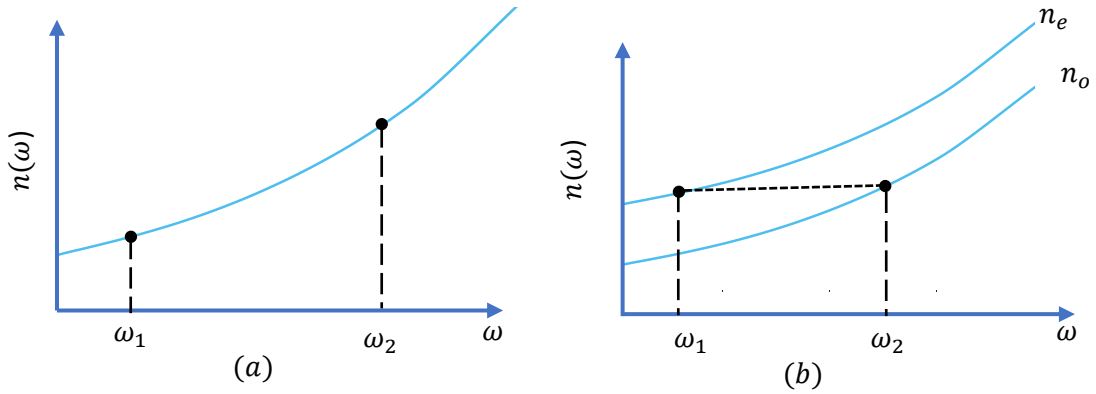

Figure 2.4: (a) Typical dispersion relation of an isotopic crystal showing that it is not possible to achieve the momentum conservation law, $\omega_2 n(\omega_2) = 2\omega_1 n(\omega_1)$, because of $n(\omega_2) \neq n(\omega_1)$. (b) Anisotropic-dispersion properties show that $n(\omega_2) = n(\omega_1)$ to satisfy the conservation law of photon momentum, $\omega_2 n(\omega_2) = 2\omega_1 n(\omega_1)$.

2.3.2 Quasi-Phase Matching (QPM)

QPM uses a periodic structure of modulated nonlinear coefficient d_{eff} alternating between positive and negative at each coherence length $L_{coh} = \pi/|\Delta k|$, with period $\Lambda = 2L_{coh}$. The accumulated phase-mismatch is compensated by adding π at each coherence length L_{coh}, as shown in Fig. 2.5. It is more convenient to write the phase-matching condition in Eq. (2.28) in terms of wavelengths instead of frequencies by including the QPM term:

$$\Delta_{QPM} = \Delta k - \frac{2\pi}{\Lambda} = n_p \frac{2\pi}{\lambda_p} - n_s \frac{2\pi}{\lambda_s} - n_i \frac{2\pi}{\lambda_i} - \frac{2\pi}{\Lambda} \tag{2.33}$$

Figure (2.6) shows how the QPM boosts the idler generated wave intensity I_i, compared with the case of phase-mismatch.

By comparing QPM with BPM, we can see the advantages and disadvantages of both methods. In QPM, it is not necessary to choose specific polarization directions of the applied waves to achieve phase matching, while it is necessary in BPM. On the other hand,

the fabrication of the QPM crystal is a drawback compared with BPM which exists in some crystals in nature [34]–[36].

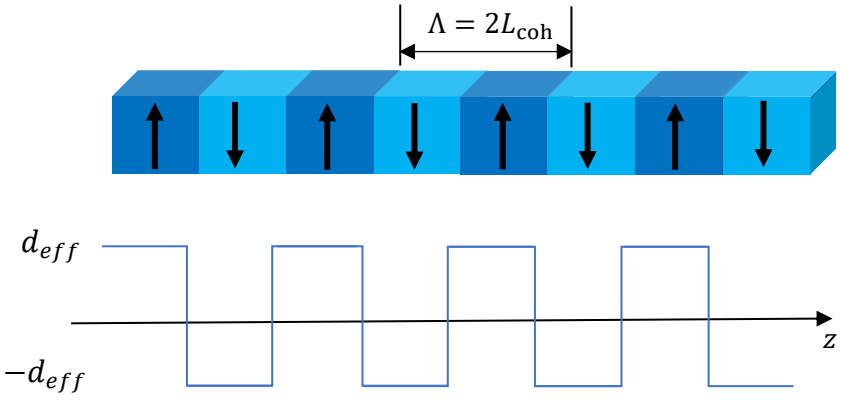

Figure 2.5: Nonlinear crystal with modulated nonlinear coefficient d_{eff}, alternating between positive and negative at each coherence length $L_{coh} = \pi/|\Delta k|$, with period $\Lambda = 2L_{coh}$.

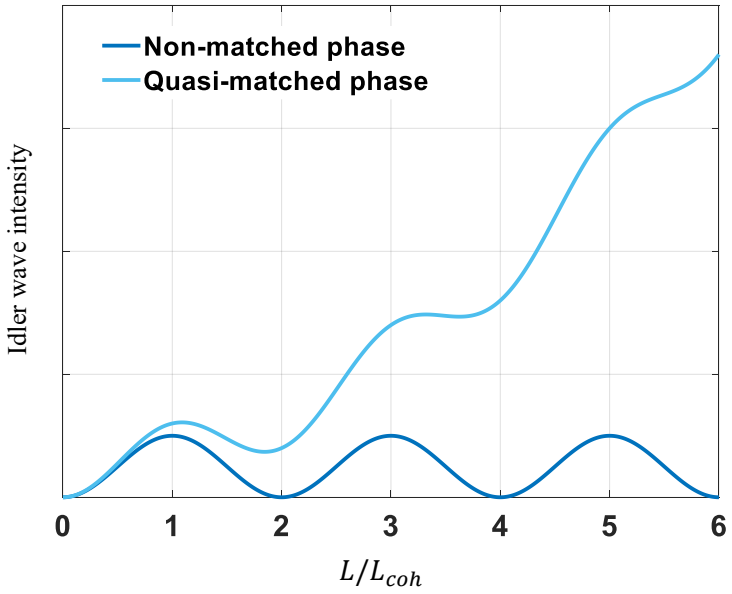

Figure 2.6: Quasi-phase matching and non-phase matching curves showing how the QPM boosts the generated intensity compared with an oscillation in the phase-mismatching case.

Chapter 3

Optical Metamaterials

3.1 Introduction

Metamaterial is generally defined as a composite structure of subwavelength particles of different materials and is usually built in a periodic manner of the particles. The size and shape of the particles, along with the constituent materials, determine the metamaterial's characteristics. An optical metamaterial medium is treated as inhomogeneous at the microscopic scale, but its electromagnetic response is expressed in terms of homogenized effective constituent parameters (permittivity and permeability) at the macroscopic scale [25].

The first mention of metamaterials occurred in 2000, in a paper by Smith et al.[37] . The research experiment demonstrated the existence of a negative index of a split-ring-resonator (SRR) structure at microwave frequencies. A negative index medium does not exist in nature, which is why it is called a metamaterial [25]. The term "negative index material" was first used in 1968 by [38], who showed theoretically the possibility to have a material with negative permittivity and permeability that results in a negative index. Note that it is not necessary for a structure to have a negative index property in order for it to be considered a metamaterial. Metamaterials can be any structure of metals, dielectric or semiconductors whose particle size and separation are at the subwavelength scale.

There are two main approaches to characterizing metamaterial structures in terms of their electromagnetic constitutive parameters: electric permittivity ε and magnetic permeability μ. The first approach uses the effective medium theory, while the second extracts them from scattering parameters. Both methods are presented in this chapter.

3.2 Effective Medium Theory

The effective medium theory determines macroscopically the electromagnetic parameters (permittivity, permeability) of a composite structure by averaging the constitutive parameters of its particles that are subwavelength in size. Some articles refer to the particles as "scatters" [39]–[41]. In the optical fields where the wavelengths are in the range of

hundreds of nanometres, the particles are nanoparticles. Figure 3.1 shows the simplest particle shape of a spherical with permittivity ε_p, embedded in a host material with permittivity ε_s. The particle is much smaller in size compared with the wavelength, $a \ll \lambda$; however, the interaction of the particle with electromagnetics can be analyzed by quasi-static approximation [42]–[44].

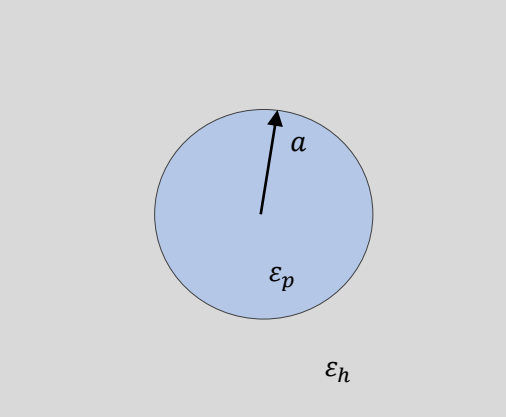

Figure 3.1: Spherical particle with permittivity $\varepsilon_p$embedded in a host material with permittivity ε_h.

The effective permittivity of the spherical particle and the host material is given by [28], [45]:

$$\varepsilon_{eff} = \varepsilon_h \frac{f\varepsilon_h(\varepsilon_p - \varepsilon_h)}{\varepsilon_h + (1-f)(\varepsilon_p - \varepsilon_h)\frac{1}{3}} \tag{3.1}$$

where f is the filling ratio of the particles inside the host. The relation in Eq. (3.1) is known as Maxwell-Garnett. If the particle is not spherical, the relation in Eq. (3.1) should be modified to be in a more general form by adding a geometrical parameter known as the depolarization factor q_i:

$$\varepsilon_{eff} = \varepsilon_h \frac{f\varepsilon_h(\varepsilon_p - \varepsilon_h)}{\varepsilon_h + (1-f)(\varepsilon_p - \varepsilon_h)q_i} \tag{3.2}$$

where $i = 1$, 2, and 3 represents the three principal axes of the particle, with the corresponding depolarization factors of q_1 q_2, and q_3 [40]. The depolarization factors of a particle shape depend on the ratio of its principal axes, not on their absolute values, and must satisfy $q_1 + q_2 + q_3 = 1$. If the particle is a sphere, then $q_1 = q_2 = q_3 = 1/3$ and the effective permittivity ε_{eff} will be as in Eq. (3.1). The depolarization factors of different shapes of ellipsoids and circular cylinder can be found in [41], [46]–[48]. A needle shape is a special case of ellipsoid and has the depolarization factors of $q_1 = 0$ and $q_2 = q_3 = 1/2$, while a disk is a special case of a circular cylinder and has depolarization factors of $q_1 = 1$ and $q_2 = q_3 = 0$. Cylindrical nanowires and longitudinal holes are special cases of a circular cylinder shape with depolarization factors of $q_1 = 0$ and $q_2 = q_3 = 1/2$.

3.3 Drude Model-Effective Permittivity

The plasma frequency in a bulk of conductors such as metals depends on the electron density and mass. It is usually in the spectrum region of near ultraviolet (UV) or visible [25]. In [49], Pendry showed that the plasma frequency can be shifted toward lower frequencies up to the far-infrared spectrum region by using arrays of periodic infinite thin metallic wires. Figure 3.2 shows a two-dimensional cubic periodic array of thin metal wires with conductivity σ, radius r, and period d, embedded in a host material of permittivity ε_h. The wire boundary reduces the average electron density and increases the effective electron mass, thus reducing the plasma frequency [25], [49]. The Drude model effective permittivity for fields parallel to the wires is given by [25], [49]:

$$\varepsilon_{eff} = \varepsilon_h - \frac{\omega_p^2}{\omega(\omega + j\varepsilon_o d^2 \omega_p^2 / \pi a^2 \sigma)} \tag{3.3}$$

where the plasma frequency of the wire media given by:

$$\omega_p^2 = \frac{2\pi c^2}{d^2 \, ln(d/a)} \tag{3.4}$$

However, the above-mentioned methods for finding effective permittivity have some restrictions. Using the effective medium theory makes it difficult to find the depolarization factors for some complex shapes, while the Drude model method determines the

permittivity only along the wires and the orthogonal permittivity is approximated to be equal to the host material permittivity ε_h.

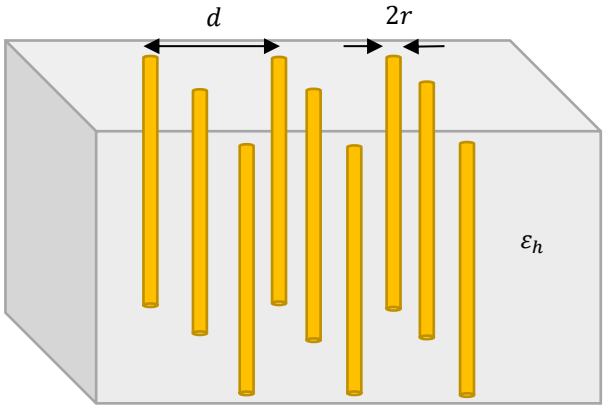

Figure 3.2: Two-dimensional arrays of infinite thin metal wires of radius r and period d, embedded in a host material of permittivity ε_h.

3.4 Extracting Effective Permittivity from Scattering Parameters

Metamaterial is a structure with geometrical properties that are much smaller than the operating wavelength. It is important to compute the effective electromagnetic parameters of metamaterial, such as permittivity ε, permeability μ, refractive index n, and wave impedance η. These four parameters are interrelated complex quantities. The parameters ε and μ form the constitutive relations of the electromagnetic response of material to its excitation and are part of the Maxwell's equations. The other parameters, n and η, are mostly related to the wave propagation and boundary conditions between different materials within a structure.

Although metamaterial structure is treated as inhomogeneous at the microscopic scale, its electromagnetic macroscopic response is expressed in terms of homogenized effective parameters. Figure 3.3 shows a schematic of a symmetrically homogenous slab of thickness L that represents a metamaterial with macroscopic scattering parameters (S-parameters) [50]. Due to the symmetry properties of the slab, $S_{22} = S_{11}$and $S_{12} = S_{21}$.

These scattering parameters are entirely related to the electromagnetic parameters, μ , n , and η.

There are numerous ways to determine complex effective electromagnetic parameters from a macroscopic response. One method uses *S*-parameters and only requires knowing the magnitude and phase of the parameters. S_{11} and S_{21}, as shown in Fig. 3.3, represent the reflection and transmission parameters, respectively. S_{11} is a fraction of the incident field that is reflected, while $S_{21}$is a fraction of the transmitted field through the slab thickness L. *S*-parameter terminology is primarily used at microwave frequencies but can be used at optical frequencies as well.

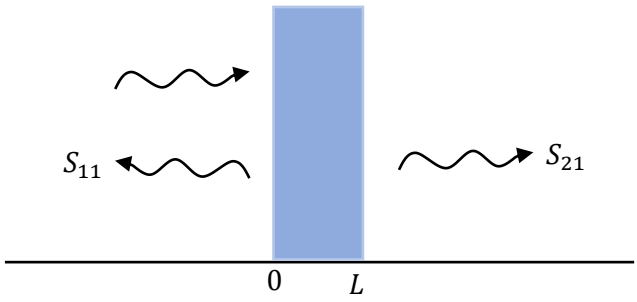

Figure 3.3: Symmetrically homogenous metamaterial structure slab.

The method relies on the measurements or full-wave numerical simulation of a slab of metamaterial structure to compute the *S* -parameters. If the homogenous slab of thickness L in Fig. 3.3 is placed in a vacuum (free space), and a plane wave with wavenumber k_o is applied normally to the slab, the index n and the wave impedance η will be related to the *S* -parameters S_{11} and S_{21} in accordance with the following equations [50]:

$$n = \pm\frac{1}{k_o L}cos^{-1}\left(\frac{1}{2S_{21}^2}[1 - S_{11}^2 + S_{21}^2]\right) \tag{3.5}$$

$$\eta = \pm\sqrt{\frac{(1+S_{11})^2 - S_{21}^2}{(1-S_{11})^2 - S_{21}^2}} \tag{3.6}$$

where k_o is a free space wavenumber. The index n and the impedance η are related to the *S*-parameters based on Fresnel's equations. The index n in Eq. (3.5) is a complex number,

with $Re(n)$ referring to the refractive index and $Im(n)$ referring to the absorption index, as given in equations (3.7) and (3.8), respectively:

$$Re(n) = \pm Re\left\{\frac{1}{k_o L} cos^{-1}\left(\frac{1}{2S_{21}^2}[1 - S_{11}^2 + S_{21}^2]\right)\right\} + \frac{2m\pi}{k_o L} \tag{3.7}$$

$$Im(n) = \pm Im\left\{\frac{1}{k_o L} cos^{-1}\left(\frac{1}{2S_{21}^2}[1 - S_{11}^2 + S_{21}^2]\right)\right\} \tag{3.8}$$

The sign of the $Im(n)$ in Eq. (3.8) is selected to be positive in order to satisfy the causality condition. This condition requires the imaginary part of the index to be positive for any passive material. The sign selected in Eq. (3.8) must also be applied to Eq. (3.7), since they are both one complex solution of Eq. (3.5).

In the real part of the index $Re(n)$ in Eq. (3.7), it is possible to have a positive or negative sign., based on the causality condition that passive materials have positive or negative refractive indices. Caution should be used to select the sign of $Re(n)$, as the positive and negative values are possible solutions. To choose the correct sign, it is essential to be familiar in advance with the expected value of $Re(n)$, and $Re(n)$ must be continuous across a wide range of wavelengths [25]. The boundaries of the slab and thickness L should be carefully selected to obtain the right results. The *S*-parameters are strongly related to the boundary locations of the slab and thickness, in that S_{11} depends on the boundary location and S_{21} depends on the thickness L.

Another method is proposed by [51] to retrieve n from the *S* -parameters given by:

$$Re(n) = \frac{1}{k_o L}\{Im[ln(e^{jnk_o L})] + 2m\pi\} \tag{3.9}$$

$$Im(n) = -j\frac{1}{k_o L}\{Re[ln(e^{jnk_o L})]\} \tag{3.10}$$

where

$$e^{jnk_o L} = \frac{S_{21}}{1 - S_{11}\frac{\eta - 1}{\eta + 1}} \tag{3.11}$$

This method starts by obtaining the wave impedance η in Eq. (3.6), and then applying η in Eq. (3.11) to compute the complex exponential function $e^{jnk_o L}$. The sign of the impedance η is selected such that the imaginary part of the index $Im(n)$ in Eq. (3.10) must be positive for the causality condition. Both methods were used in this work for the same goal. Based

on the results obtained using the two methods, the first one was more robust and had fewer errors.

Selecting the thickness of the slab L had a huge impact on the achieved results. The main criterion used to determine whether we had the correct results was the continuity of the retrieved results over a range of wavelength of interest. The effective medium theory was used as a third method, mainly as a comparison to verify our retrieved results from the *S*-parameters. The structures investigated in this work are periodic, and it was found that the corrected results were obtained when we used the thickness L as being equal to one period length of the structure.

The permittivity ε and permeability μ can be found using the retrieved index n and the impedance η, based on the following relations [25], [50], [51]:

$$\varepsilon = \frac{n}{\eta} \tag{3.12}$$

$$\mu = n\eta \tag{3.13}$$

The parameters ε and μ are constitutive parameters that relate the material response to its excitation. If the magnetic response of a material at optical frequencies is negligible [25], then we might use $\mu = 1$, the value of the free space medium. Therefore, we need only to compute ε. Combining equations (3.12) with (3.13) and using $\mu = 1$, the effective permittivity ε is given by:

$$\varepsilon = n^2 \tag{3.14}$$

Effective medium theories relate the permittivity of individual elements of a composed structure to obtain the resultant effective one. The relation in Eq. (3.14) was used to compute the permittivity obtained by the retrieval method from the *S*-parameters with that obtained by the effective medium theory.

Chapter 4

Optical Analysis of GaAs and Ag Nanowire Metamaterial from Scattering Parameters at Near- and Mid-IR Frequencies

4.1 Abstract

Phase matching in optical difference frequency generation (DFG) with the nonlinear medium gallium arsenide (GaAs) is unachievable due to the dispersion and isotropic properties of GaAs. However, an anisotropic property can compensate for the dispersion. This study optically characterizes an anisotropic metamaterial nanostructure of silver (Ag) nanowires embedded in GaAs, by using finite difference time domain (FDTD) simulation. A transparent region with very low losses is defined for DFG waves with polarization parallel and orthogonal to the wires.

4.2 Introduction

A zinc-blende (cubic) lattice structure with isotropic linear properties has a large second-order nonlinear susceptibility $\chi^{(2)}$ and a wide optical transmission window of λ = 1 μm to 17 μm[14]. These properties make GaAs a good choice for nonlinear optical interaction processes of three-wave mixing (parametric interaction processes) in the mid-IR spectrum, for example, optical frequency conversion, optical parametric amplification, or optical parametric oscillation [17], [18], [20], [23]. A nonlinear interaction process involves an energy exchange among the waves to be mixed. An efficient interaction requires energy and momentum conservation of the mixed waves. Energy conservation involves frequency matching, while momentum conservation involves phase matching.

Phase matching among waves with different frequencies is not achievable in an isotropic dispersive GaAs medium, because the waves travel with different velocities. However, birefringence with an anisotropic medium can compensate for the dispersion[52]. Inserting metal nanowires such as silver (Ag) nanowires into a GaAs medium results in a medium with an anisotropic linear property. Phase-matched difference generated wavelengths from 2.8 μm to 11

μm have been achieved by using artificial birefringence in a structure of GaAs with silver nanowires[53].

It has been demonstrated that a composite of metal nanowires in a polymer structure can be used to achieve extreme anisotropic properties at optical and near-IR frequencies [26]. A homogeneous effective anisotropic medium can be realized via a 3D nanowire medium in the optical frequency region [29]. It has been shown that parallel wire media possess very strong spatial dispersion effects at any frequency[54]. The periodic arrangement of thin metallic wires has been analyzed numerically and characterized at microwave frequencies as a low loss medium for waves with polarization parallel to the wires [55]. In addition, a theoretical analytical and numerical study has investigated thermal emission from a finite metamaterial medium of silver nanowires for waves with polarization parallel to the wires [56]. A bulk medium of silver nanowires has demonstrated that the medium exhibits negative refraction at any angle of light incidence in the visible frequencies[28].

In the present study, a metamaterial nanostructure medium of GaAs with embedded silver nanowires is characterized at the frequencies of the optical transparency region of GaAs, from λ = 1 μm to 17 μm, for an *E* field polarized parallel ($E_{\parallel}$) and orthogonally ($E_{\perp}$) to the nanowires. The characterization is defined by the linear properties of the refractive and absorption indices. A finite difference time domain (FDTD) method was employed to determine the scattering parameters (*S*-parameters) used to find the refractive and absorption indices. The aim of this research is to contribute to an understanding of the GaAs and Ag nanowire medium by characterizing it at near- and mid-IR frequencies, for field polarizations parallel and orthogonal to the wires.

4.3 Computing Optical Linear Properties from the *S*-Parameters

Although a metamaterial medium is treated as inhomogeneous at the nanoscale, its electromagnetic response is expressed in terms of homogenized effective parameters. Fig.4.1(a) shows the metamaterial structure of GaAs and a two-dimensional square of embedded arrays of silver nanowires, with period d and radius a.

A thin slab of metamaterial medium is selected to compute the *S*-parameters [50], [51], [57]. Fig. 4.1 (b) illustrates the top view of a slab of the medium of thickness d, with wires along the x-axis with period d. It is necessary to compute the complex index n, $n =$

$Re(n) + jIm(n)$ from the S-parameters for the E field polarized parallel ($E_{\parallel}$) and orthogonally ($E_{\perp}$) to the wires. $Re(n)$ represents the refractive index and $Im(n)$ represents the absorption index for passive materials.

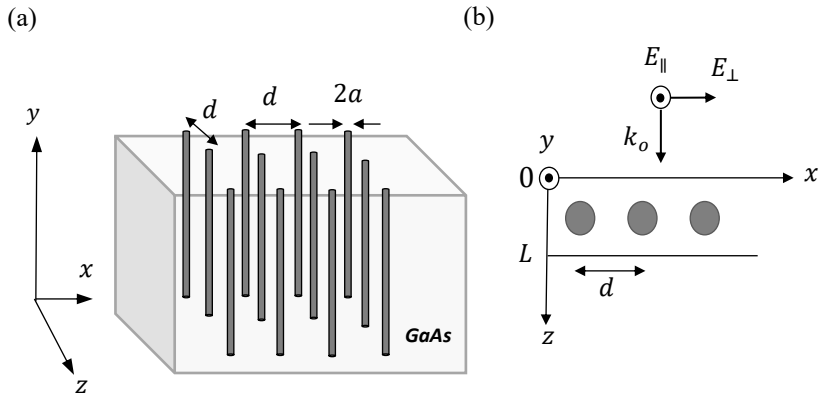

Figure 4.1: (a) Nanostructure of GaAs as host medium with embedded square arrays of silver nanowires with period d and radius a. (b) Top view of a slab of the structure.

If a plane wave is applied normally to the boundary of the slab at the origin $z = 0$, the structure index n and impedance η are related to the *S*-parameters S_{11} (reflection coefficient) and S_{21} (transmission parameter) in accordance with the following equations[51]:

$$\eta = \pm\sqrt{\frac{(1+S_{11})^2 - S_{21}^2}{(1-S_{11})^2 - S_{21}^2}} \tag{4.1}$$

$$e^{jnk_oL} = \frac{S_{21}}{1 - S_{11}\frac{\eta-1}{\eta+1}} \tag{4.2}$$

The real and imaginary parts of the index n, $Re(n)$, and $Im(n)$ are derived from Eq. (4.1) and Eq. (4.2) as follows[51] :

$$Re(n) = \frac{1}{k_oL}\left\{Im\left[ln\left(e^{jnk_oL}\right)\right] + 2m\pi\right\} \tag{4.3a}$$

$$Im(n) = -j\frac{1}{k_oL}\left\{Re\left[ln\left(e^{jnk_oL}\right)\right]\right\} \tag{4.3b}$$

Here L and k_o are the slab thickness and the wave number of the incident wave in free space, respectively, and m is an integer number. Due to the symmetry properties of the

slab, S_{22}=S_{11} and S_{12}=S_{21}. The sign of the impedance η in Eq. (4.1) is chosen so that the imaginary part of the index $Im(n)$ in Eq. (4.3b) is positive, to satisfy the causality condition. The causality condition requires the imaginary part of the index to be positive for any passive material [58], [59]. The FDTD simulation was applied to the slab by using the commercial software tool RSoft FullWAVE®. A periodic boundary condition was implemented in the transverse direction along the x-axis, perpendicular to the propagating wave, as shown in Fig.4.1(b). The wires extend unbounded along the y-axis. Experimentally measured data for the refractive and absorption indices of GaAs [60] and Ag [61], from $\lambda = 1$ μm to 17 μm, were used in the FDTD simulation. Fig. 4.2(a) shows the real and imaginary parts of the Ag indices $Re(n_{Ag})$ and $Im(n_{Ag})$, respectively. Fig.4.2(b) illustrates the real refractive index of GaAs, $Re(n_{GaAs})$, where the imaginary part is negligible.

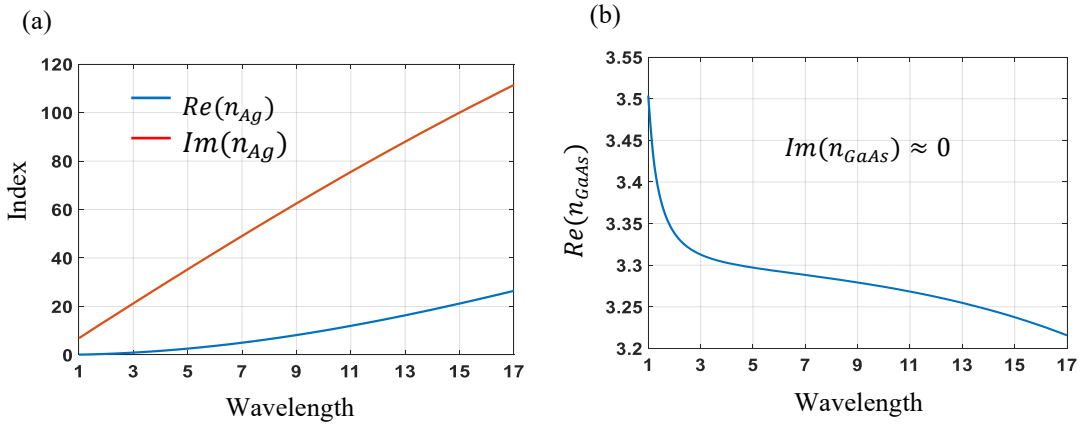

Figure 4.2: Experimental measured data of the refractive and the absorption indices, from 1 μm to 17 μm. (a) Silver. (b) GaAs.

Fig. 4.3 shows the computed S-parameters, magnitude and phase, for $E_{\parallel}$ and $E_{\perp}$, at $d = 150$ nm and $a = 25$ nm.The geometric parameters d and a have been chosen based on the long wavelength limit for metamaterials, $(d, a) \ll \lambda$. For $E_{\parallel}$, as the wavelength decreases below 2 μm, the reflection declines and the transmission increases, implying that the structure tends to behave as a transparent medium with very little loss. At longer wavelengths, with much stronger interaction between the parallel fields and the wires, the structure acts as a reflector. For $E_{\perp}$, transmission is high for the entire region of interest,

from $\lambda = 1$ µm to 17 µm, especially for $\lambda > 3$ µm. At shorter wavelengths of $\lambda < 3$ µm, the structure behaves as a transparent dielectric with little absorption.

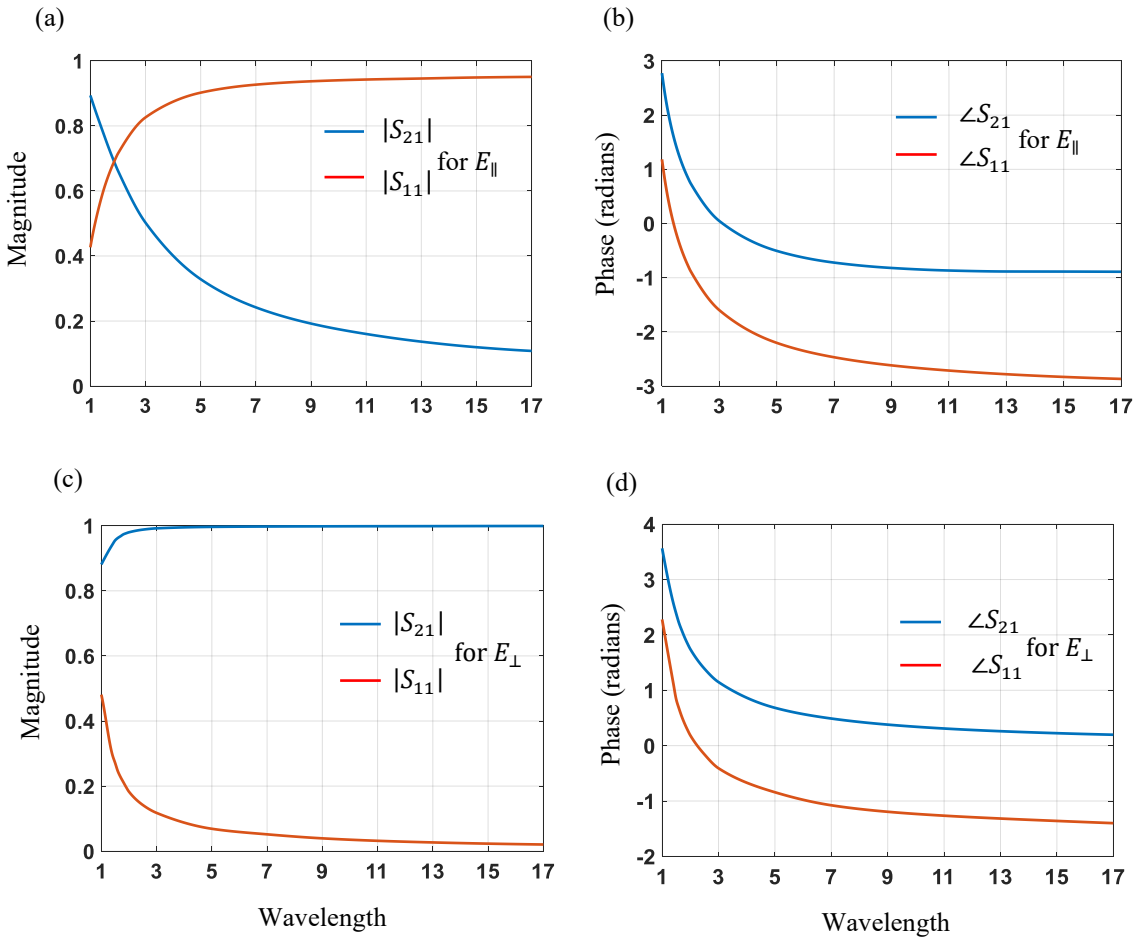

Figure 4.3: S-parameters at $d = 150$ nm and $a = 25$ nm, for parallel polarization $E_\parallel$ and orthogonal polarization $E_\perp$. (a) Magnitude of S_{21} and S_{11} for $E_\parallel$. (b) Phase of S_{21} and S_{11} for $E_\parallel$. (c) Magnitude of S_{21} and S_{11} for $E_\perp$. (d) Phase of S_{21} and S_{11} for $E_\perp$.

Fig.4.4 illustrates the two-dimensional electric field distribution for the parallel polarization $E_\parallel$, represented by E_y, at $d = 200$ nm and $a = 35$ nm, for $\lambda = 1$ µm and 1.8 µm. The field distribution was obtained using FDTD simulation by applying a plane wave of unity intensity. Additional details on FDTD simulation using the RSoft tool are given in Appendix A. The distribution illustrated in Fig. 4.4(b) is at $\lambda = 1.8$ µm, which shows that the transmission has declined compared with the distribution of $\lambda = 1$ µm depicted in Fig. 4.4(a). This implies that the loss will increase at longer wavelengths. The

distribution also indicates that the wavelengths inside the structure for the corresponding free space incident wavelengths, $\lambda = 1$ μm and $\lambda = 1.8$ μm, became shorter, with values of 0.3 μm and 1.25 μm, respectively. As a result, the effective refractive indices are 3.33 and 1.44 for $\lambda = 1$ μm and 1.8 μm, respectively. This indicates strong normal dispersion

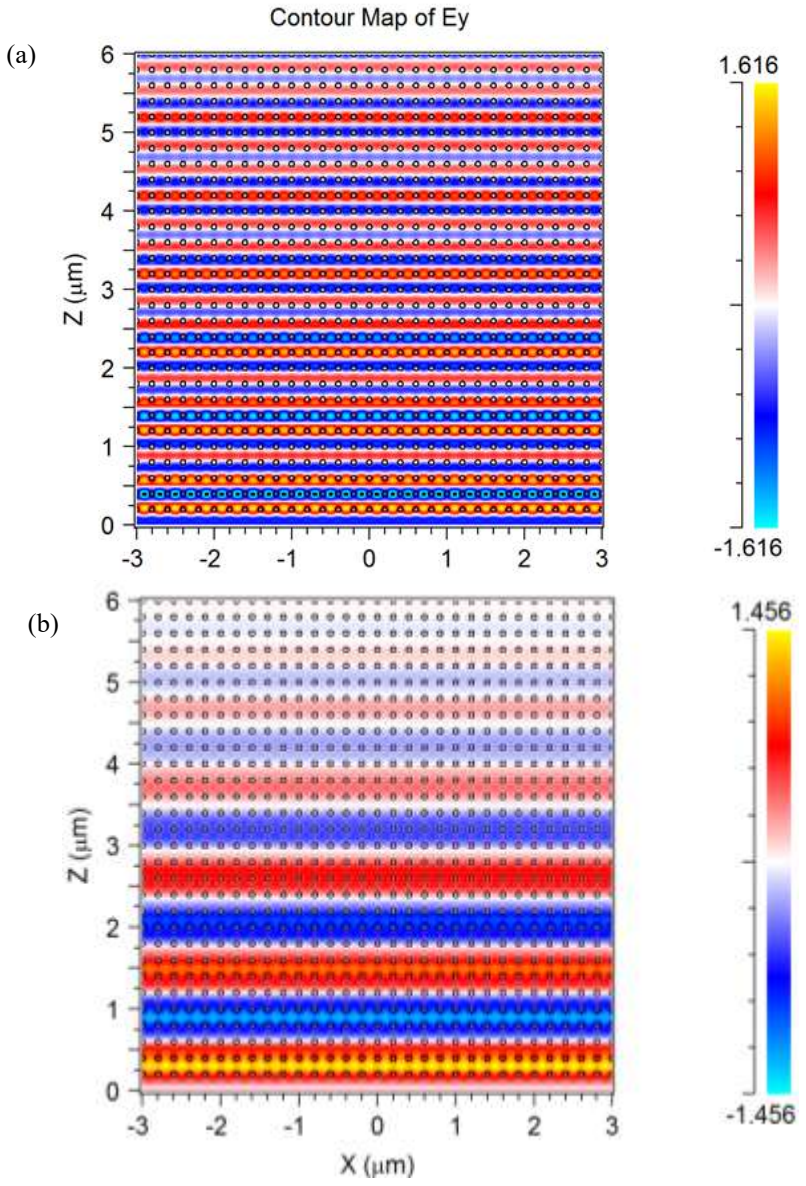

Figure 4.4: Field distribution for the parallel polarization $E_{\parallel}$ represented by E_y. at $d = 200$ nm and $a = 35$ nm. (a) $\lambda = 1$ μm. (a). (b) $\lambda = 1.8$ μm.

, as the refractive index decreases with longer wavelengths. Figure (4.5) illustrates the two-dimensional electric field distribution for the orthogonal polarization $E_{\perp}$, represented by E_x, at $d = 200$ nm and $a = 35$ nm, for $\lambda = 1$ µm and 1.8 µm. The distribution depicted in Fig. 4.5b is for $\lambda = 1.8$ µm, which shows that the transmission has increased compared with $\lambda = 1$ µm depicted in Fig 4.5a.

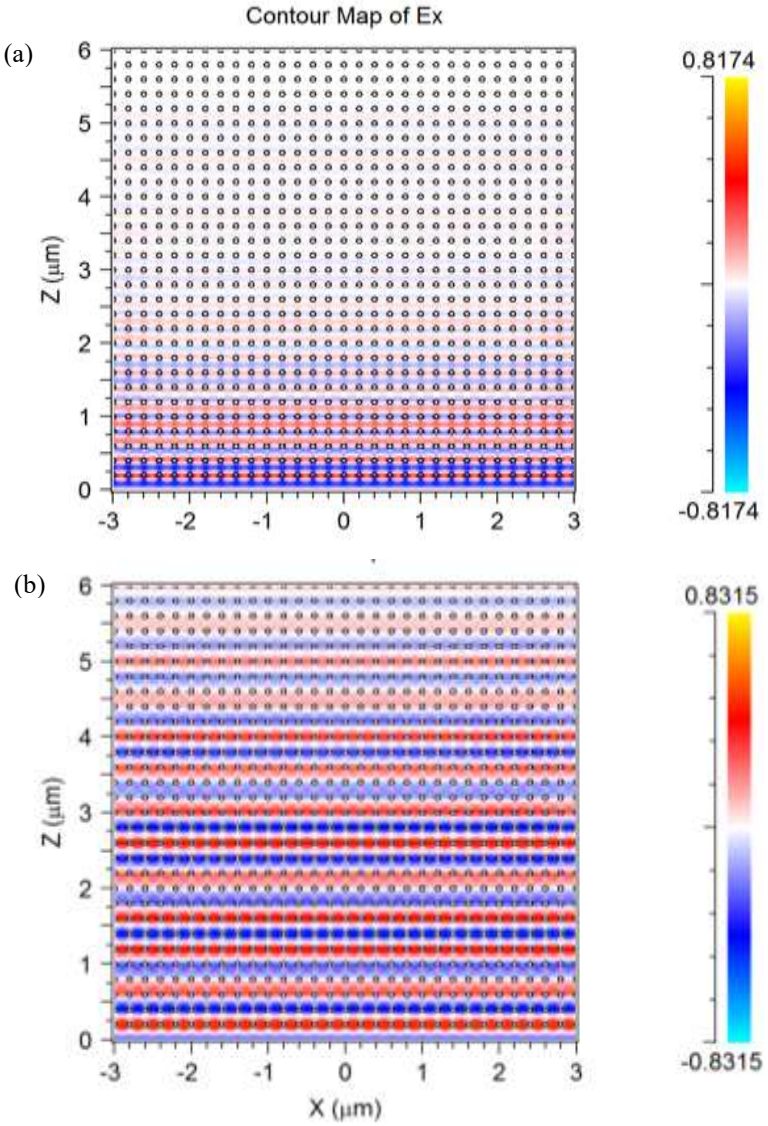

Figure 4.5: Field distribution for the orthogonal polarization $E_{\perp}$ represented by E_x at $d = 200$ nm and $a = 35$ nm. (a) $\lambda = 1$ µm. (a). (b) $\lambda = 1.8$ µm.

.

The wavelengths inside the structure for the corresponding free space incident wavelengths, $\lambda = 1$ μm and $\lambda = 1.8$ μm, became shorter, with values of 0.22 μm and 0.25 μm, respectively. As a result, the effective refractive indices are 4.54 and 4, for $\lambda = 1$ μm and 1.8 μm, respectively. This indicates that the normal dispersion is not strong.

Figure 4.6 shows the electric field distribution for parallel E_y and orthogonal E_x polarizations at $d = 200$ nm and $a = 35$ nm, for $\lambda = 3.5$ μm. It is obvious that the parallel polarized field E_y is highly reflected and decaying inside the structure, while the orthogonal polarized field E_x is partially reflected and propagating through the structure. The parallel polarization is attenuated due to the high absorption by the silver nanowires, whereas the wires have less effect on the orthogonal polarization. As result, the longer wavelengths of parallel polarization experience higher loss compared to the shorter wavelengths, and vice-versa for the orthogonal polarizations.

Figure 4.7 shows the real and imaginary refractive and absorption indices for $E_{\parallel}$ and $E_{\perp}$. $Re(n^{\parallel})$, $Im(n^{\parallel})$, $Re(n^{\perp})$ and $Im(n^{\perp})$ were computed from the *S*-parameters presented in Fig.4.3 by using the equations (4.3a) and (4.3b). It can be seen from $Re(n^{\parallel})$ and $Re(n^{\perp})$ in Figures 4.7(a) and 4.7(b), respectively, that the structure can be characterized as an anisotropic medium with uniaxial properties.

The $Re(n^{\parallel})$ dispersion function shown in Fig. 4.7(a) changes from normal dispersion to anomalous dispersion at the plasma frequency f_p of the plasma wavelength $\lambda_p = 1.93$ μm. At wavelengths shorter than the plasma wavelength, $\lambda < \lambda_p$, $Re(n^{\parallel})$ represents normal dispersion, the $Im(n^{\parallel})$ shown in Fig. 4.7(c) is very small, and the structure behaves as a transparent dielectric. For $\lambda > \lambda_p$, $Re(n^{\parallel})$ represents anomalous dispersion, $Im(n^{\parallel})$ increases, and the structure acts as a strong reflector and absorber.

For $E_{\perp}$interactions, $Re(n^{\perp})$ in Fig. 4.7(b) represents normal dispersion, the $Im(n^{\perp})$ shown in Fig.4.7(d) is very small especially for $\lambda > 3\ \mu m$, and the structure behaves as a dielectric over the entire range of $\lambda = 1$ μm to 17 μm.

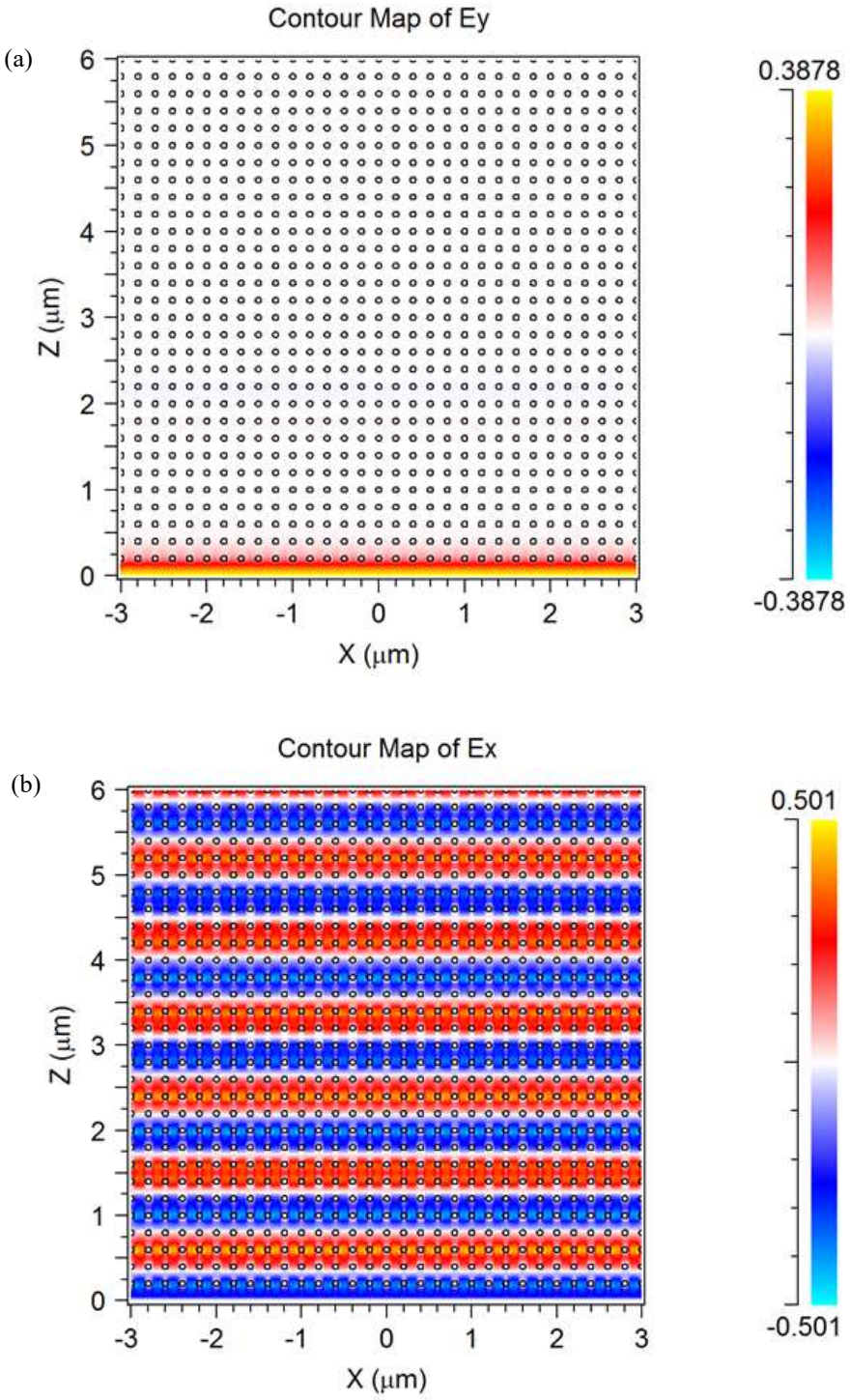

Figure 4.6: Field distribution at $d = 200$ nm and $a = 35$ nm, and $\lambda = 1$ μm. (a) Parallel polarization to the wires $E_{\parallel}$ represented by E_y. (b) Orthogonal polarization to the wires $E_{\perp}$ represented by E_x.

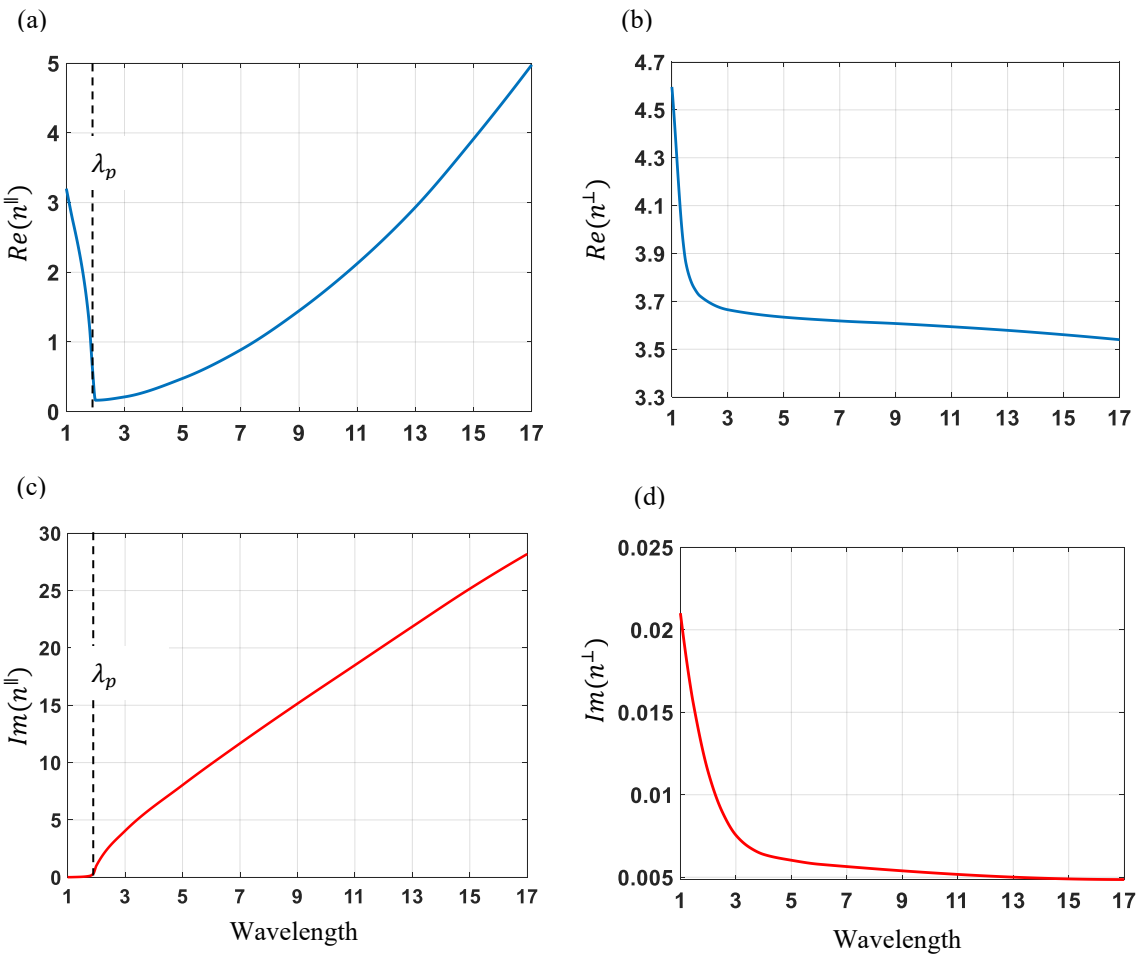

Figure 4.7: Refractive and absorption indices at $d = 150$ nm and a= 25 nm, for parallel polarization $E_{\parallel}$ and orthogonal polarization $E_{\perp}$. (a) and (c) show $Re(n^{\parallel})$ and $Im(n^{\parallel})$ for $E_{\parallel}$, respectively. (b) and (d) show $Re(n^{\perp})$ and $Im(n^{\perp})$ for $E_{\perp}$,

The achieved contrasting dispersion results of $Re(n^{\parallel})$ and $Re(n^{\perp})$ are very promising for the use of this structure in birefringent phase matched optical DFG. DFG for GaAs requires the three interacting waves to be orthogonal, based on the nonzero elements of the second-order susceptibilities of GaAs $\chi^{(2)}_{xyz} = \chi^{(2)}_{yzx} = \chi^{(2)}_{zxy}$ [62]. Mid-IR waves with wavelengths longer than 3 μm are generated by the DFG of two near-IR waves with wavelengths shorter than 2 μm. Due to the very small losses of the structure at wavelengths shorter than 2 μm for $E_{\parallel}$, one of the two applied near-IR waves is polarized parallel to the wires, while the second applied near-IR wave and the generated mid-IR waves are orthogonally polarized.

The magnetic permeability of natural materials at optical frequencies is always close to the free space value of unity ($\mu = 1$) [25]. Some structures with sub-wavelength dimensions may achieve a magnetic response. However, since no magnetic response is expected for the structure under consideration, the permittivity ε is determined by $\varepsilon = n^2$ [55], [63]. Figures 4.8 and 4.9 show the real and imaginary parts of the parallel and orthogonal permittivity computed from the corresponding refractive indices shown in Fig. 4.7.

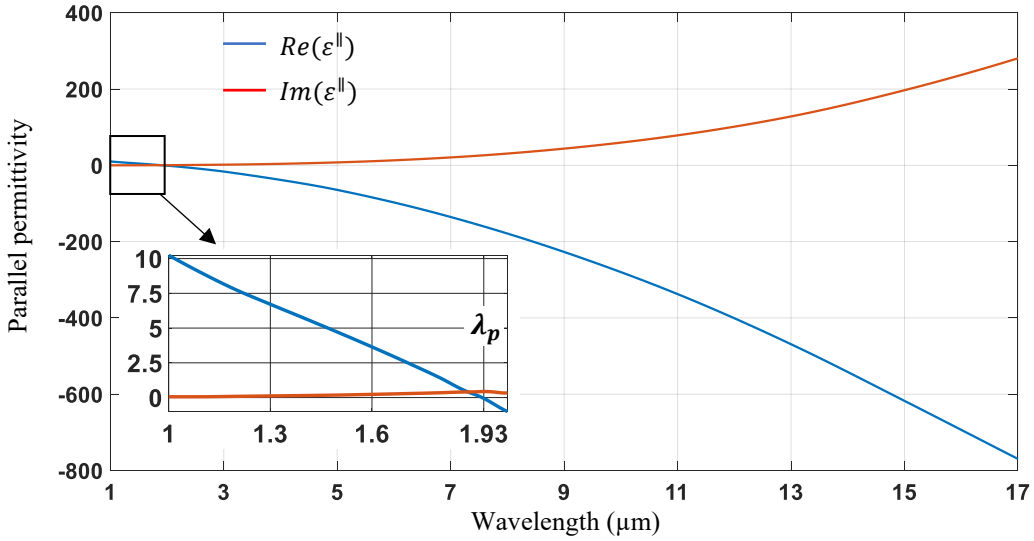

Figure 4.8: $Re(\varepsilon^{\parallel})$ and $Im(\varepsilon^{\parallel})$ at $= 150$ nm and $a = 25$ nm, computed from the corresponding refractive indices that are shown in Fig. 4.7 (a) and Fig.4.7(c).

$Re(\varepsilon^{\parallel})$ in Fig.4.8 exhibits a decrease from positive values to negative values, with a value of zero at the plasma wavelength $\lambda_p = 1.93$ μm. This is the plasma wavelength also shown in Fig.4.7, where the refractive index changes from normal to anomalous dispersion. The corresponding imaginary permittivity at the plasma wavelength is $Im(\varepsilon^{\parallel}) = 0.42$. At wavelengths longer than the plasma wavelength, $\lambda > \lambda_p$, $Re(\varepsilon^{\parallel})$ becomes negative, $Im(\varepsilon^{\parallel})$ increases, and the structure acts as a strong reflector. In Fig.4.9, $Re(\varepsilon^{\perp})$ is positive and $Im(\varepsilon^{\perp})$ is very small, especially for $\lambda > 3$ μm.

The transparent region for parallel polarization waves can be widened either by decreasing the wire radius a, or by increasing the period d. Fig.4.10 shows different *S*-

parameter results for $E_{\parallel}$, at wire radii $a = 15$ nm, 25 nm, and 35 nm, with a fixed period of $d = 150$ nm. Fig.4.11 shows $Re(n^{\parallel})$ and $Im(n^{\parallel})$ computed from the *S*-parameters. A smaller radius causes the plasma wavelength to redshift and widens the transparent region.

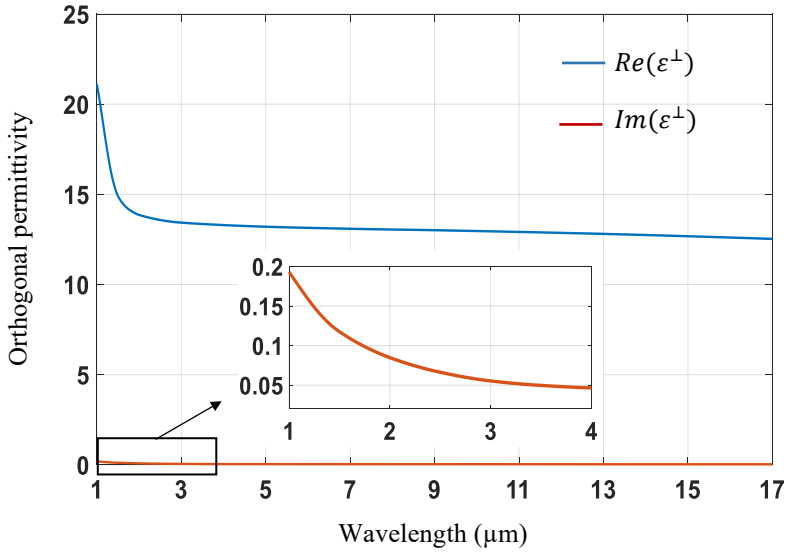

Figure 4.9: $Re(\varepsilon^{\perp})$ and $Im(\varepsilon^{\perp})$ at $d = 150$ nm and $a = 25$ nm, computed from the corresponding refractive indices shown in Fig. 4.7 (b) and Fig.4.7(d).

4.4 Comparison with Drude Model Results

The Drude model approximation is another method for finding only the parallel effective permittivity of a wire medium, as shown in Fig. 4.1(a). If the structure satisfies the long wavelength limit $(a, d) \ll \lambda$, the effective parallel permittivity along the wires is represented by the Drude model as [49], [56]:

$$\varepsilon^{\parallel} = \varepsilon_{GaAs} - \frac{\omega_p^2}{\omega(\omega + j\varepsilon_o d^2 \omega_p^2 / \pi a^2 \sigma_{Ag})} \tag{4.4}$$

where ω_p is the plasma frequency, defined as:

$$\omega_p^2 = \frac{2\pi c^2}{d^2 \, ln(d/a)} \tag{4.5}$$

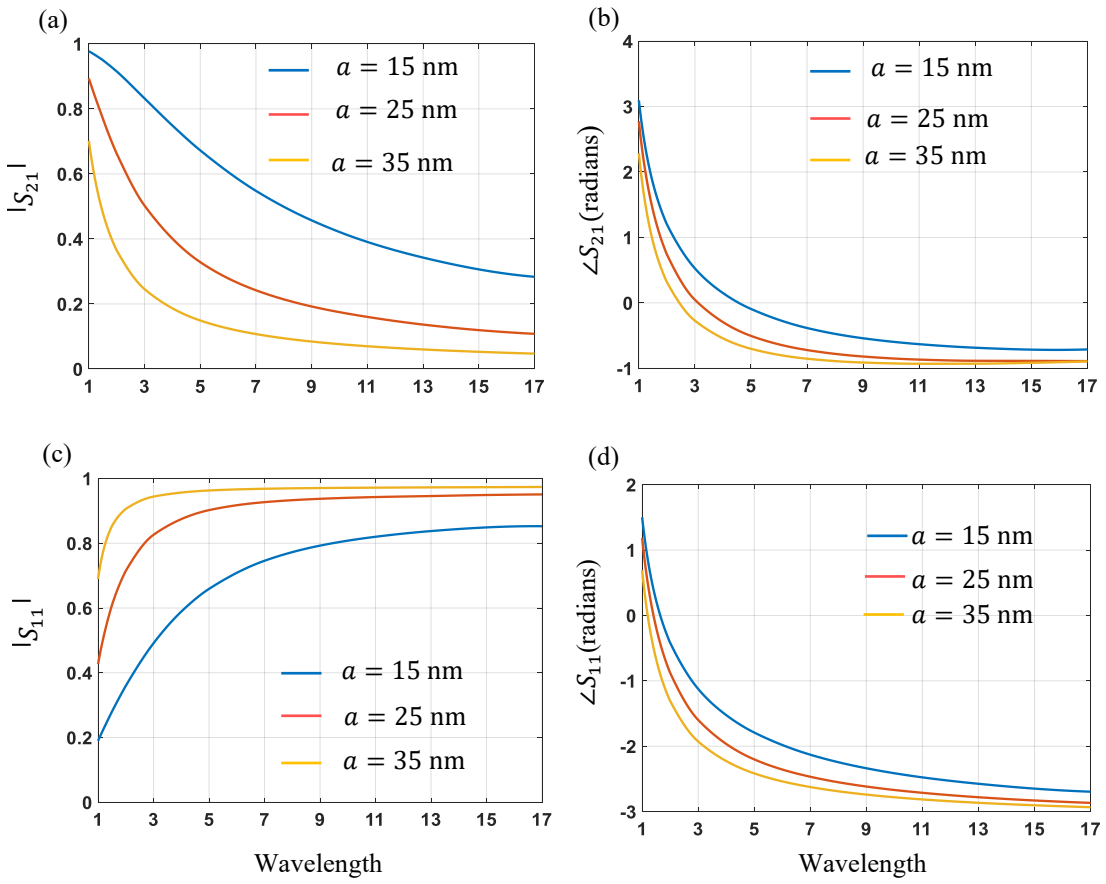

Figure 4.10: S-parameters for wire radius $a = 15$ nm, 25 nm, and 35 nm, with a fixed period of $d = 150$ nm, for parallel polarization $E_{\parallel}$. (a) Magnitude of S_{21}. (b) Phase of S_{21}. (c) Magnitude of S_{11}. (d) Phase of S_{11}.

ε_{GaAs} is the permittivity of GaAs, and σ_{Ag} represents the electrical conductivity of silver. The experimental data for GaAs permittivity used for the Drude model are the same as those used in the FDTD simulation. The corresponding index is defined as $n^{\parallel} = \pm\sqrt{\varepsilon^{\parallel}}$. Because the structure is passive, the sign of the square root is selected so that the imaginary part is positive. Fig. 4.12 compares the refractive indices obtained via the Drude model with those obtained from the FDTD simulation, at $d = 150$ nm and $a = 25$ nm. The silver conductivity σ_{Ag} in Eq. (4.4) is $6.28 \times 10^{7}\Omega^{-1}\mathrm{m}^{-1}$. The comparison shows excellent agreement at the short wavelengths, with a slight discrepancy at longer wavelengths.

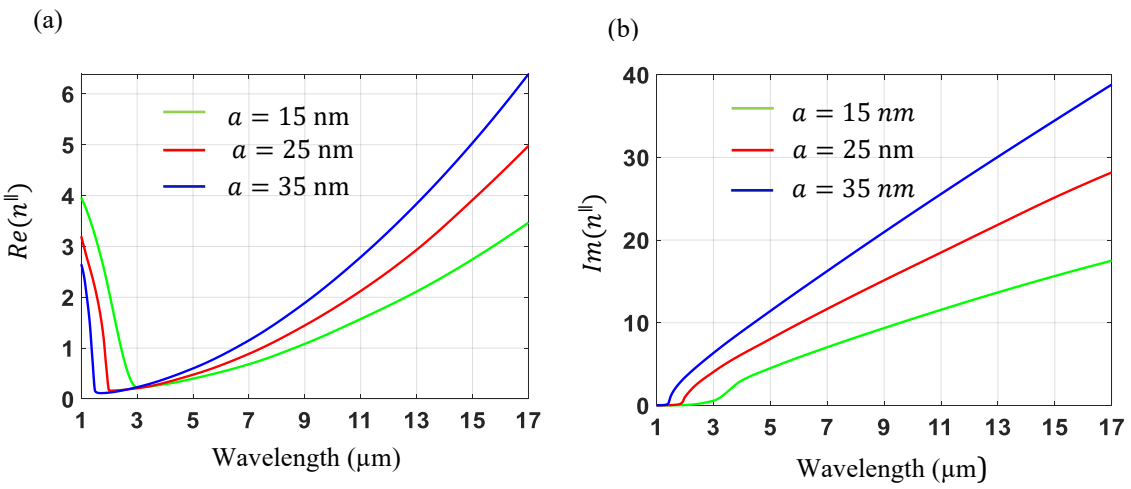

Figure 4.11: $Re(n^{\parallel})$ and $Im(n^{\parallel})$ for wire radius $a = 15$ nm, 25 nm, and 35 nm, with a fixed period of $d = 150$ nm, computed from the *S*-parameters presented in Fig. 4.10, for $E_{\parallel}$. (a) $Re(n^{\parallel})$. (b) $Im(n^{\parallel})$.

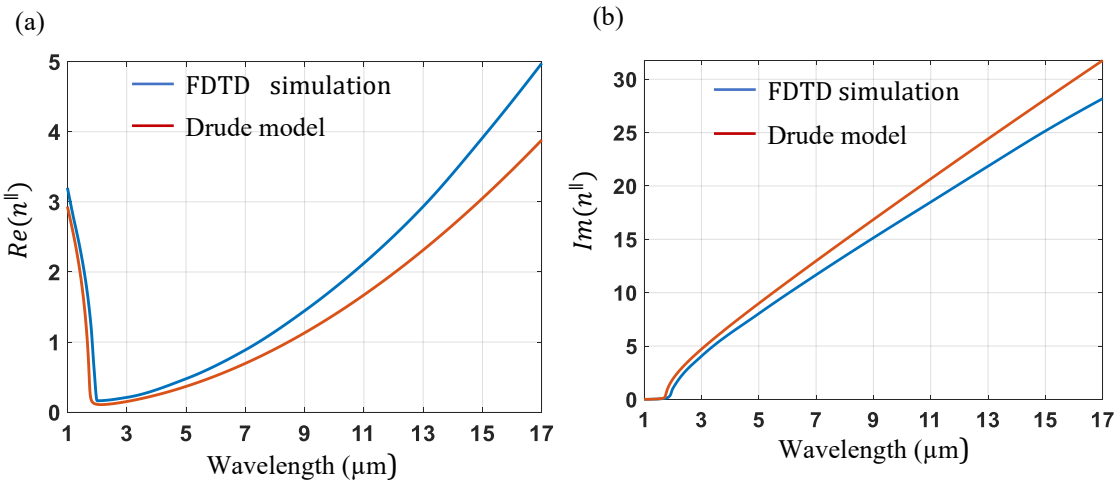

Figure 4.12: Comparison of parallel refractive and absorption indices obtained from the FDTD simulation and the Drude model, at $d = 150$ nm and a $= 25$ nm. (a) $Re(n^{\parallel})$. (b) $Im(n^{\parallel})$.

4.5 Conclusions

Optical linear properties of a GaAs and silver nanowire metamaterial have been characterized by determining the refractive and absorption indices from the S-parameters. A retrieval method was used to extract the indices from the S-parameters. The results show

a transparent region for waves with polarization parallel to the nanowires at near-IR frequencies. The near-IR transparent region and the anisotropic properties of the nanowires can be utilized to compensate for phase mismatching of three-wave mixing in the isotropic-dispersive GaAs. One of the two near-IR waves is applied with polarization parallel to the nanowires, while the second near-IR wave and the generated mid-IR waves are polarized orthogonally to the wires. The transparent near-IR region can by widened either by decreasing the radius or by increasing the period of the nanowires. To verify the results, the FDTD simulation results were compared with those obtained via the Drude model. Excellent agreement was achieved at the short wavelengths, with a slight discrepancy at longer wavelengths.

Chapter 5

Phase Matching for Difference Frequency Generation in GaAs Via an Artificial Birefringence Technique Using Silver Nanowires

Published in IEEE Photonics Journal, June 2018, Vol. 10, No. 3., 1300110
DOI:10.1109/JPHOT.2018.2841983

5.1 Abstract

The lack of anisotropic properties in GaAs prevents the use of birefringence as a phase matching technique in three-wave mixing with GaAs as a nonlinear medium. When metallic nanowires are embedded in GaAs, the composite structure is characterized as a metamaterial with anisotropic properties, if the separation distance between the nanowires is less than the wavelengths of the mixed waves. The effective permittivity is used to investigate this metamaterial structure with its anisotropic properties theoretically in terms of phase matching for difference frequency generation (DFG). The resultant difference frequencies, which are in the mid-infrared region, are broadly tunable from 2.8 μm to 11 μm. This tuning is performed by varying the pump and the signal wavelengths in the range between 1μm to 2 μm. The losses of the structure due to absorption are included using the transfer matrix method.

5.2 Introduction

Phase matching, which involves momentum conservation of the photons, is the most important aspect to consider in nonlinear optical frequency mixing[6]. In general, phase matching requires the medium to be a non-dispersive material. Although the materials are dispersive, phase matching is achieved by using birefringence and quasi-phase matching techniques in media made of materials such as periodically poled lithium niobate (PPLN), potassium titanyl phosphate (KTP), and barium borate (BBO). Difference frequency generation is used to generate optical frequencies that cannot be generated by using ordinary laser sources. Most difference frequency generation (DFG) based on parametric

wavelength conversion uses nonlinear crystals, such as PPLN, KTP, BBO, and lithium niobate[10], [11]. GaAs and InP, with a cubic lattice structure from the III-V semiconductor group, are alternative for optical frequency mixing[34]. Optical mixing based on InP material for second harmonic generation and optical rectification were experimentally verified for 1.55 μm fundamental wavelength[13]. GaAs, with larger second-order susceptibility $\chi^{(2)}$ and wide transparent infrared optical window, from 1 μm to 17 μm, is a better candidate for difference frequency generation[14]. Despite these advantages, it is not possible to use birefringence phase matching techniques with GaAs or InP, due to their isotropic properties.

There are other methods for achieving phase matching in III-V semiconductors with a cubic lattice structure, for difference frequency generation, such as quasi-phase matching, modal phase matching, domain-disordered quasi-phase matching, and suspended GaAs waveguides [14], [16]–[18], [64]. Tunable emissions from 6.7 μm to 12.7 μm have been demonstrated in a nonguided orientation patterned GaAs [19], and the longest wavelength was generated through DFG in AlGaAs waveguide from 7.5 μm to 8.5 μm [20].

Phase matching by using artificial anisotropy is possible if a strongly anisotropic structure can be obtained. Artificial birefringence using multi-layered GaAs/AlAs was first proposed by J. P. van der Ziel [21]. Relatively large birefringence has been demonstrated with the multilayer structure of oxidized GaAs/AlAs [22]. Phase matching has been achieved for parametric amplification of down conversion by using artificial birefringence in multilayer waveguides of oxidized GaAs/AlAs [23]. Phase matching has been demonstrated for a DFG by using artificial birefringence with a multilayer structure of GaAs/Al_x Ga_{1-x} As, with three layers of Al_x Ga_{1-x} As and one layer of GaAs [24]. Obtaining a large birefringence or a strongly anisotropic structure has been challenging. The use of an optical metamaterial with metallic nanowires is an alternative method of obtaining a strongly anisotropic structure[25]–[29].

In the present research, we performed a theoretical investigation of the phase matching aspect of DFG in a slab medium of a metamaterial structure of GaAs with permittivity ε_{GaAs} as the host material, with inclusions of periodic arrays of silver nanowires. To our knowledge, there have been no published attempts made to use nanowires with GaAs

metamaterials structure for phase matching to generate mid-infrared wavelengths (terahertz frequencies).

5.3 Theory

The metamaterial structure that is composite of a dielectric and very thin periodic metallic wires could have an effective plasma frequency below the bulk plasma frequency which is generally in the ultraviolet (UV) range. The effective plasma frequency is changeable and could be reduced to IR, THz, or GHz by changing the period of the wires[49], [56], [65]. In metamaterial structures, where metal and dielectric nanoparticles are intermixed together within the scale of nanometers, finding the optical response of such structures by solving Maxwell's equations is impossible because of the complexity of the boundary conditions. An inhomogeneous structure with a scale less than the wavelength is treated as one macroscopically uniform medium using the approximation of the effective medium approach [25]. Under this approximation, the scattering response by individual metal and dielectric nanoparticles is determined from the average response of the whole system using the effective permittivity[25].

The geometry analyzed in this work is a slab of a composite structure of periodic arrays of silver nanowires of a period d and a radius a embedded in GaAs with electric permittivity ε_{GaAs} as a host medium, as shown in Fig.5.1(a). Fig.5.2(b) shows the Miller indices of the GaAs lattice structure as defined in Cartesian coordinates and illustrates the polarizations and propagation of the three waves to be mixed. The three waves are defined as the pump wave ω_p, with electric field E_p; the signal wave ω_s, with electric field E_s; and the idler wave $\omega_i(\omega_i = \omega_p - \omega_s)$, with electric field E_i, where $\omega_p > \omega_s > \omega_i$.

We consider the applied waves at normal incidence to the wires, with the electric field polarized parallel to the wires along $[001]$ for the pump wave E_p, and orthogonally polarized along $[\bar{1}10]$ for the signal wave E_s. Based on the second order susceptibilities $\chi^{(2)}_{xyz}$ and $\chi^{(2)}_{yzx}$ of GaAs, the resultant difference wave E_i will be orthogonally polarized along $[\bar{1}10]$. If the waves are propagating orthogonally to the wires and the electric field is parallel, with the limit $d \ll \lambda$, the effective permittivity of the structure in the direction parallel to the wires can be modeled by lossy Drude model [49], [56], [65] as:

$$\varepsilon_z = \varepsilon^{\parallel} = \varepsilon_{GaAs}\left[1 - \frac{\omega_{plasma}^2}{\omega(\omega + i\gamma_{eff})}\right] \tag{5.1}$$

$$\gamma_{eff} = \frac{\varepsilon_o}{\sigma}\frac{2c^2}{a^2 ln(d/a)} \;,\; \omega_{plasma}^2 = \frac{1}{\varepsilon_{GaAs}}\frac{2\pi c^2}{d^2\, ln(d/a)} \tag{5.2}$$

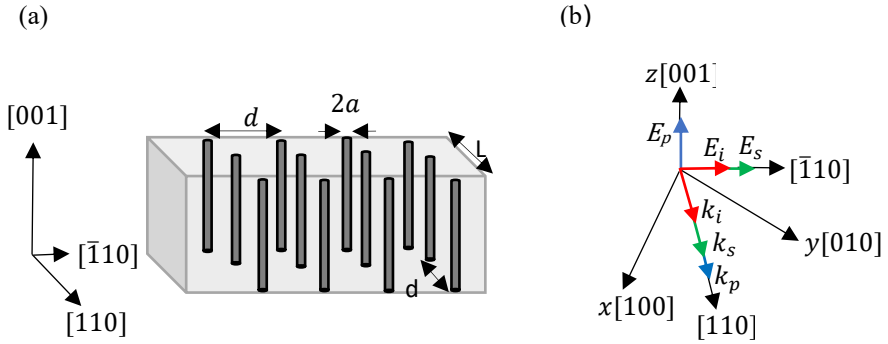

Figure 5.1: (a) Structure of silver nanowires of period d embedded in GaAs medium of electric permittivity ε_{GaAs}, with a thickness $L = Nd$, and semi-infinite height and width, where N is the number of wires columns. (b) Illustration of Miller indices of GaAs lattice structure with Cartesian coordinates, wave propagation directions, and polarizations.

Here γ_{eff} is the effective damping frequency, ω_{plasma} is the effective plasma frequency, and σ is the static conductivity of silver. The effective damping frequency γ_{eff} strongly depends on the wire radius a, which offers more degree of freedom to modify the absorption properties of the structure. If the wires radii are very thin compared to the wavelength ($a \ll \lambda$), their orthogonal polarization can be neglected, and the orthogonal permittivity will be the same as the host medium ε_{GaAs} [54]:

$$\varepsilon_x = \varepsilon_y = \varepsilon^{\perp} = \varepsilon_{GaAs} \tag{5.3}$$

The TE polarization has the electric field directed along the z-axis; and the TM polarization has the electric field oriented parallel to the xy plane, which thus has components in x the and y directions. The idler wave ω_i and the signal wave ω_s are TM polarized with wavevectors k_i and k_s, respectively. They propagate in the plane xy, making an angle of 45° with respect to the x and y axes. The pump wave ω_p is TE polarized

in the z-direction with a wavevector k_p according to the following Type-I coupling interaction:

$$E_p(TE) - E_s(TM) \xrightarrow{\chi^{(2)}_{xzy}=\chi^{(2)}_{yzx}} E_i(TM) \tag{5.4}$$

Type-I coupling is a polarization configuration where the signal polarization is parallel to the idler polarization; while in type-II, the signal and the idler polarizations are orthogonal[66]. Efficient difference frequency generation requires large second-order susceptibility $\chi^{(2)}$ and phase matching between the three wavevectors; $k_p(\omega_p)$, $k_s(\omega_s)$, and $k_i(\omega_i)$. The phase matching condition is expressed in terms of the wavevectors as $\Delta k = k_p(\omega_p) - k_s(\omega_s) - k_i(\omega_i)$.This structure can be successfully fabricated using electrochemically growing of metallic nanowires in porous alumina template [67]–[70], where the holes are filled with the metals such as silver (Ag). In the following stage the host alumina matrix is removed, and the free-standing wires are filled with another material such as GaAs [69], [70].

5.4 Results and Discussions

We investigated the structure within the optical transmission window of GaAs, in the spectral region from 1 μm to 17 μm. The pump wave has the shortest wavelength, the idler wave has the longest wavelength, and the wavelength of the signal wave is between the other two. The structure is tuned by varying the pump wave frequency ω_p and the signal wave frequency ω_s. The idler wave is the wave with the difference frequency $\omega_i = \omega_p - \omega_s$ that satisfies the phase matching condition. We used experimentally measured data for GaAs permittivity [60]. The structure parameters values have been chosen for the diameter $2a = 35$ nm and the period $d = 350$ nm, as a compromise between the absorption and the longest achievable difference frequency at the matching.

Fig.5.2 shows the real and imaginary parts of the parallel and the orthogonal permittivities $\varepsilon^{\parallel}$ and $\varepsilon^{\perp}$. As the pump wave is parallel polarized, the real and imaginary parts of the parallel permittivity are plotted with respect to the pump-wave wavelengths; at the same time, the orthogonal permittivity is plotted with respect to the idler-wave wavelengths or the signal-wave wavelengths because of their orthogonal polarization. The orthogonal permittivity is just the plot of the experimental measured data of GaAs

permittivity, with only the real part values and neglecting the imaginary part[60]. The silver conductivity in Eq. (5.1) is $6.28*10^{7}\Omega^{-1}m^{-1}$.

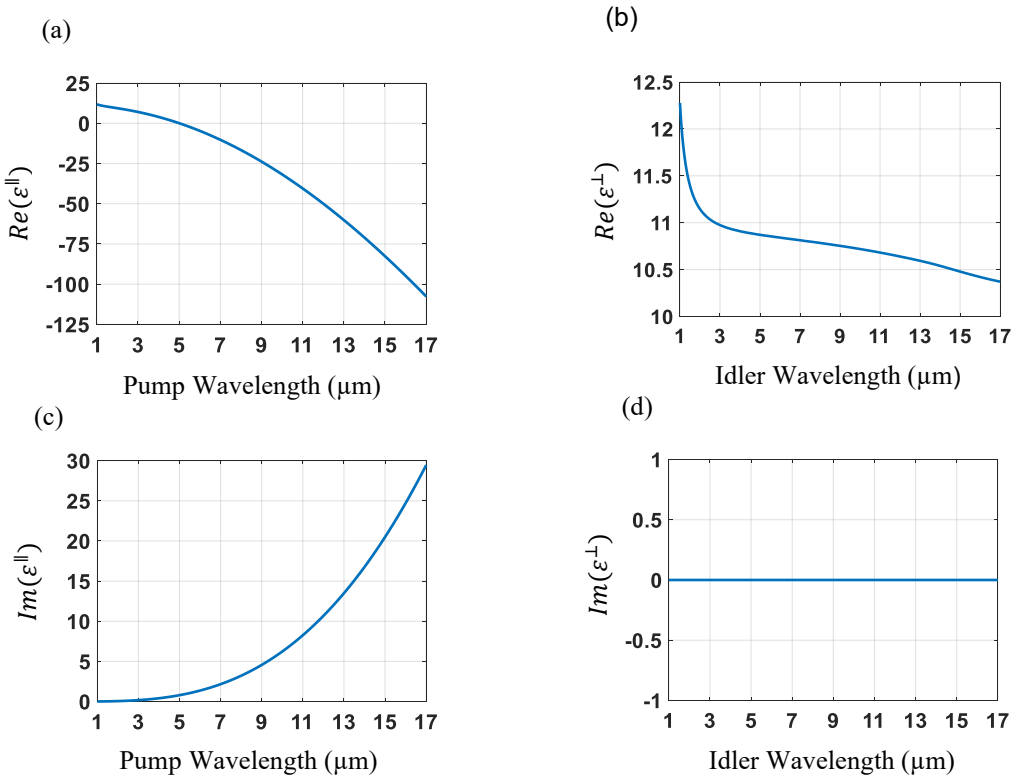

Figure 5.2: Parallel and perpendicular permittivity $\varepsilon^{\parallel}$ and $\varepsilon^{\perp}$ for wires dimeter $2a = 35\,\text{nm}$ and period $d = 350\,\text{nm}$; (a), (b) real parts of parallel and orthogonal permittivity. (c), (d) imaginary parts of parallel and orthogonal permittivity.

To examine the phase matching aspect, it is necessary to deal with the refractive indices, $n^{\parallel} = Re\left(\pm\sqrt{\varepsilon^{\parallel}}\right)$ and $n^{\perp} = Re\left(\pm\sqrt{\varepsilon^{\perp}}\right)$. The square root has two possible solution values, positive or negative (negative refractive index). Since the orthogonal permittivity is the permittivity of GaAs $(\varepsilon^{\perp} = \varepsilon_{GaAs})$, this indicates a positive refractive index. In the case of the parallel permittivity $\varepsilon^{\parallel}$, the causality requires the imaginary part of the refractive index to be positive for any passive material [25], [58], [59], which results in a positive refractive index. Fig.5.3 shows the parallel and perpendicular refractive indices. The parallel refractive index $n^{\parallel}$ has strongly dispersive properties because of the effect of the metal nanowires, while the perpendicular $n^{\perp}$, which is the experimentally measured data of the refractive index of GaAs [60], is less dispersive. These contrasting refractive indices

along the principal axes provide a possibility of achieving phase matching for three waves mixing and, specifically, generating frequencies in the mid-infrared region.

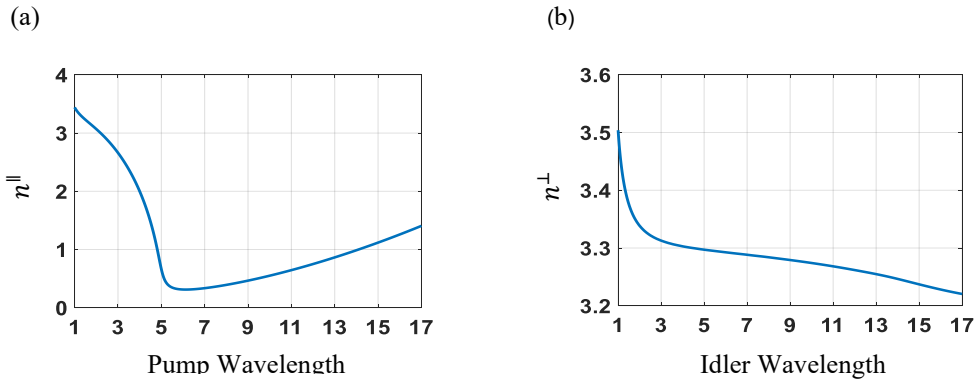

Figure 5.3: Parallel $n^{\parallel}$ and orthogonal $n^{\perp}$ indices for wires dimeter $2a = 35$ nm and period $d = 350$ nm; (a) parallel index, (b) orthogonal index.

The transfer matrix method was used to compute the absorption through the structure medium as it is treated as macroscopically uniform medium [25], with a complex effective refractive index $\tilde{n}^{\parallel} = \sqrt{\varepsilon^{\parallel}}$. The system is three layers media as shown in Fig.5.4. The structure of thickness L and complex refractive index $\tilde{n}^{\parallel}$ is impressed in a layer of index n_o. Three transfer matrices needed to find and multiplied to get the complete transfer matrix. First, we find the transfer matrices at the two interfaces:

$$M_{12} = \frac{1}{t_{12}}\begin{bmatrix} 1 & r_{12} \\ r_{12} & 1 \end{bmatrix} \tag{5.5}$$

$$M_{23} = \frac{1}{t_{23}}\begin{bmatrix} 1 & r_{23} \\ r_{23} & 1 \end{bmatrix} \tag{5.6}$$

The transfer matrix of the structure layer between the interfaces is as following:

$$M_2 = \begin{bmatrix} e^{j\delta} & 0 \\ 0 & e^{-j\delta} \end{bmatrix} \tag{5.7}$$

where $r_{12} = -r_{23} = r = \frac{n_o - \tilde{n}^{\parallel}}{n_o + \tilde{n}^{\parallel}}$, $t_{12} = \frac{2n_o}{n_o + \tilde{n}^{\parallel}}$, $t_{23} = \frac{2\tilde{n}^{\parallel}}{n_o + \tilde{n}^{\parallel}}$, and $\delta = \frac{2\pi}{\lambda}\tilde{n}^{\parallel}L$. The complete transfer matrix $M = M_{12}M_{23}M_2$:

$$M = \begin{bmatrix} b_{11} & b_{12} \\ b_{21} & b_{22} \end{bmatrix} = \frac{e^{j\delta}}{t_{12}t_{23}} \begin{bmatrix} 1 - r^2 e^{-j2\delta} & -r(1 - e^{-j2\delta}) \\ r(1 - e^{-j2\delta}) & -r^2 + e^{-j2\delta} \end{bmatrix} \tag{5.8}$$

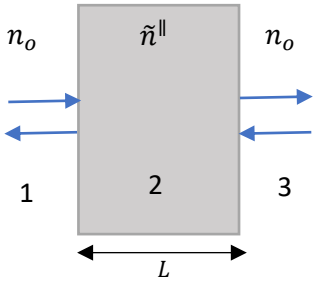

Figure 5.4: Three layers system to find reflectance R and transmittance T.

This three -layers system behaves as Fabry-Perot etalon illuminated by one incident light from the left of the structure, then the reflectance R and transmittance T are defined from the matrix M as following:

$$R = \left|\frac{b_{21}}{b_{11}}\right|^2 = \left|\frac{r(1-e^{-j2\delta})}{1-r^2e^{-j2\delta}}\right|^2 \tag{5.9}$$

$$T = \left|\frac{1}{b_{11}}\right|^2 = \left|\frac{t_{12}t_{23}e^{-j\delta}}{1-r^2e^{-j2\delta}}\right|^2 \tag{5.10}$$

Fig. 5.5 shows the absorption $A = 1 - R - T$ of the structure for thickness $L = Nd =$ 35 μm with $N = 100$ (number of wire columns), where $d = 35$nm. R is the reflectance, and T is the transmittance, assuming $n_o = 1$ for the surrounding medium. The pump waves whose electric field is parallel to the wires experience absorption, while the signal and idler waves whose electric fields are orthogonal to the wires do not experience absorption due to neglecting the orthogonal polarization of the thin wires[54] .

It is obvious from the real part of the parallel permittivity $Re(\varepsilon^{\parallel})$ in Fig.5.2(a), or the absorption A in Fig.55, that the plasma wavelength of the structure, $\lambda_{plasma} = c/\omega_{plasma}$, is around 5 μm. The absorption is extremely high at the plasma wavelength, while in the region of the wavelengths that are much shorter than the plasma wavelength ($\lambda \ll \lambda_{plasma}$) the absorption is low, in which case the real part of the parallel permittivity is positive, the imaginary part is very small, and the optical transmission is dominant. In the region where

the wavelengths are much longer than the plasma wavelength, the optical reflection is dominant. The pump-wave wavelengths λ_p that satisfy the phase matching are in the range of the spectrum from 1 μm to 1.2277 μm, which are shorter in wavelength than the plasma wavelength.

In the spectrum region $\lambda < 3$ μm, narrow oscillations (Fabry–Perot oscillations) occur in the absorption. These oscillations exist because of the coherent interference between the partial internal reflected waves. The oscillations disappear in the spectrum region $\lambda > 3$ μm because the imaginary part of the parallel permittivity $Im(\varepsilon^{\parallel})$ in Fig.5.2(c) becomes valuable, thus the absorption resonance starts to dominate, while the partial internal reflections will disappear.

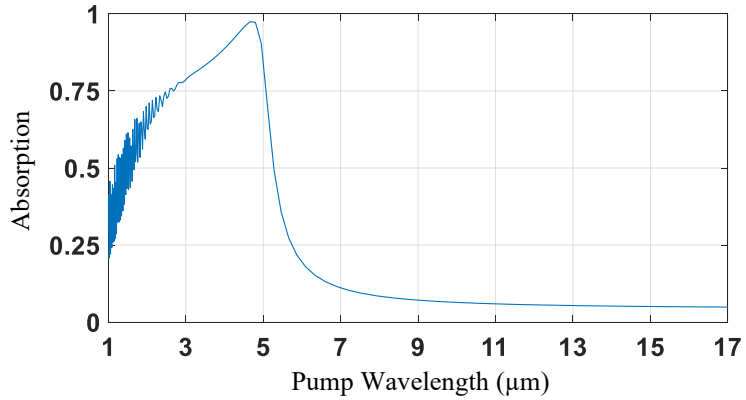

Figure 5.5: Absorption of structure for wires diameter $2a = 35\ nm$, period $d = 350$ nm, $n_o = 1$, and thickness $L = Nd = 35$ μm with $N = 100$ (number of wire columns).

Based on the refractive indices, we can determine the phase mismatch between the waves according to:

$$\Delta k = n^{\parallel}(\omega_p)\frac{\omega_p}{c} - n^{\perp}(\omega_s)\frac{\omega_s}{c} - n^{\perp}(\omega_i)\frac{\omega_i}{c} \tag{5.11}$$

The phase mismatch Eq. (5.11) was tested by varying the pump frequency ω_p and signal frequency ω_s. When the phase mismatch $\Delta k = 0$, the difference frequency ω_i is assigned to be the third frequency that satisfies the conservation of energy and momentum. Fig. 5.6 shows the

case of the phase mismatch plot ($\Delta k/k_p$) as a function of the idler wavelength λ_i, at three different values of the pump wavelengths $\lambda_p = 1$ µm, 1.069 µm, and 1.1923 µm.

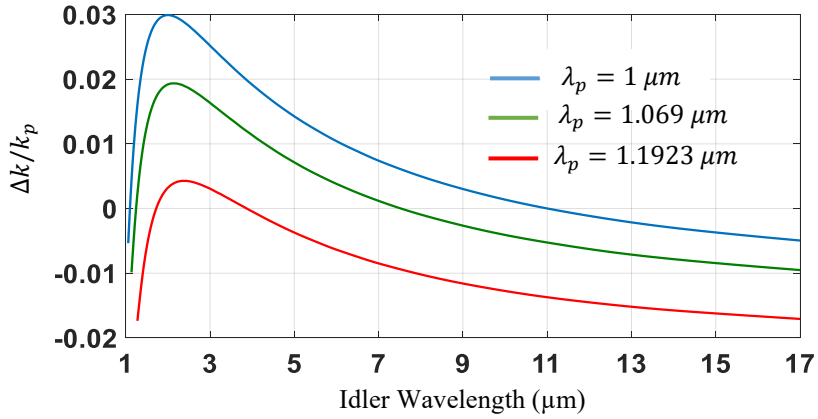

Figure 5.6: Mismatch plot ($\Delta k/k_p$) as function of idler wavelength λ_i at three different values of pump wavelengths $\lambda_p = 1$ µm, 1.069 µm, and 1.1923 µm, where $\Delta k = k_p - k_s - k_i$ and k_p is wavevector of the pump signal. Matching is achieved at the signal wavelengths $\lambda_s = 1.0997$ µm, 1.2455 µm, and 1.7222µm, respectively. Resulting idler wavelengths are $\lambda_i = 11.033$ µm, 7.5406 µm, and 3.875 µm , respectively.

It was found that the phase matching is satisfied at the following idler wavelengths $\lambda_i =$ 11.033 µm, 7.5406 µm, and 3.875 µm, respectively. The corresponding signal wavelengths at the matching are $\lambda_s = 1.0997$ µm, 1.2455 µm, and 1.7222µm, respectively. The tuning relationship between the three wavelengths that satisfied the phase matching and the energy conservation in the entire spectrum from 1 µm to 17 µm is shown in Fig. 5.7.

It is clear from this tuning relationship that the possible tuned range of the idler wavelengths, which is in the mid-infrared range, is broad, and extends from 11 µm as the longest wavelength to the shortest wavelength of 2.8 µm. The pump-wave wavelengths vary from 1 µm to 1.2277 µm, while the signal-wave wavelengths changes from 1.0997 µm to 2.1809 µm. This is a very interesting result since the pump and the signal wavelengths lie in the spectrum region from 1 µm up to 2 µm, in which the conventional tunable laser sources are available.

Nonlinear conversion processes are generally very weak due to small nonlinear coefficients of materials. The conversion efficiency at phase matching $\Delta k = 0$ in a plane-wave approximation, nondepleted pump approximation, and including the effects of linear absorption is given by [71]:

$$\eta = \frac{P_i}{P_s} = \eta^o e^{[-(\alpha_p+\alpha_s+\alpha_i)L/2]} \frac{sinh^2[(\alpha_p+\alpha_s-\alpha_i)L/4]}{[(\alpha_p+\alpha_s-\alpha_i)L/4]^2}, \quad \eta^o = \frac{8\pi^2 d_{eff}^{(2)} L^2 I_p}{\varepsilon_o n_p n_s n_i c \lambda_i^2} \tag{5.12}$$

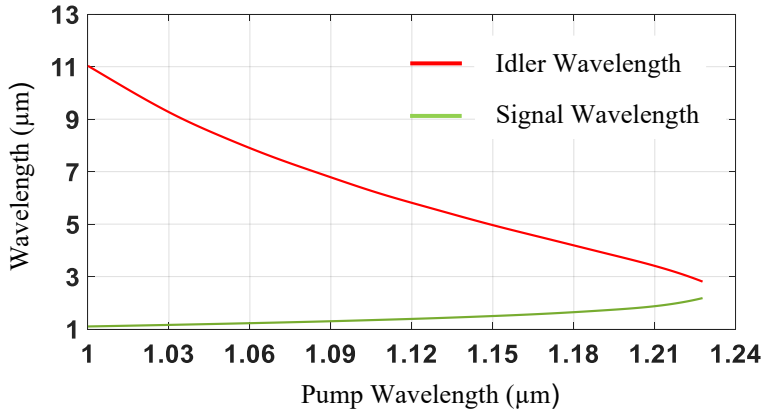

Figure5.7: Tuning relationship between three wavelengths that satisfy the phase matching condition. Pump wavelengths vary from 1 μm to 1.2277μm, signal wavelengths change from 1.0997 μm to 2.1809 μm , and idler wavelength extend from 11.033 μm to 2.8091 μm.

η^o is the lossless efficiency. α_p, α_s, and α_i are absorption coefficients for pump, signal, and idler waves, respectively. n_p, n_s, and n_i are refractive indices for pump, signal, idler waves, respectively. If the signal and the idler waves absorptions are neglected because of their negligible interaction to the tiny nanowires, the normalized efficiency to the pump intensity I_p is given as:

$$\frac{\eta}{I_p} = \frac{8\pi^2 d_{eff}^{(2)} L^2}{\varepsilon_o n_p n_s n_i c \lambda_i^2} e^{\left(\frac{-\alpha^{\parallel} L}{2}\right)} \frac{sinh^2\left(\frac{\alpha^{\parallel} L}{4}\right)}{\left(\frac{\alpha^{\parallel} L}{4}\right)^2} \tag{5.13}$$

$\alpha^{\parallel}$ is the absorption coefficient along the nanowires, and $\alpha^{\parallel} = \alpha_p = 4\pi * im\left(\sqrt{\varepsilon^{\parallel}}\right)/\lambda_p$. Fig. 5.8 shows the absorption coefficient $\alpha^{\parallel}$ versus the pump wavelength at phase matching, from 1 μm to 1.2277 μm. Absorption causes a propagation loss to the pump wave of 0.05 dB/μm at the wavelength of 1μm, and 0.075 dB/μm at wavelength 1.2μm.

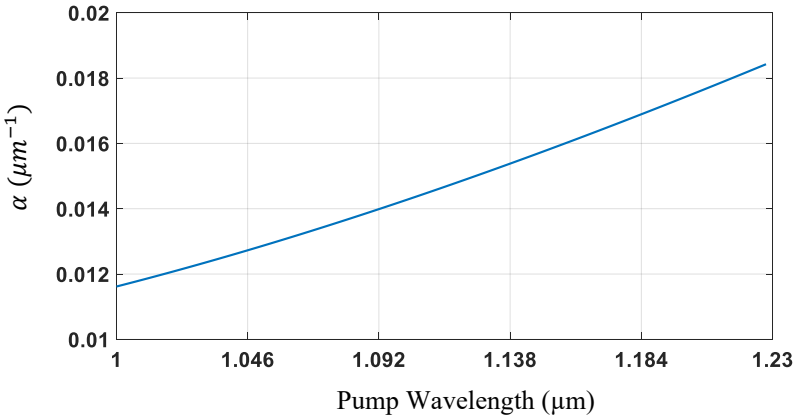

Figure 5.8: Absorption coefficient α with respect to the pump wavelength for $L = 35$ μm and $d = 350$ nm.

Fig.5.9 shows the normalized efficiency η/I_p versus the propagation length with the following parameters: $\lambda_i = 11\mu m$, $n_p = 3.4415$, $n_s = 3.4591$, $n_i = 3.2678$, and $d_{eff}^{(2)} = 370$ pm/V [6]. The efficiency is very week and limited with the propagation distances because of the ohmic loss at the pump wavelengths. Larger refractive indices and longer idler wavelengths decrease the efficiency.

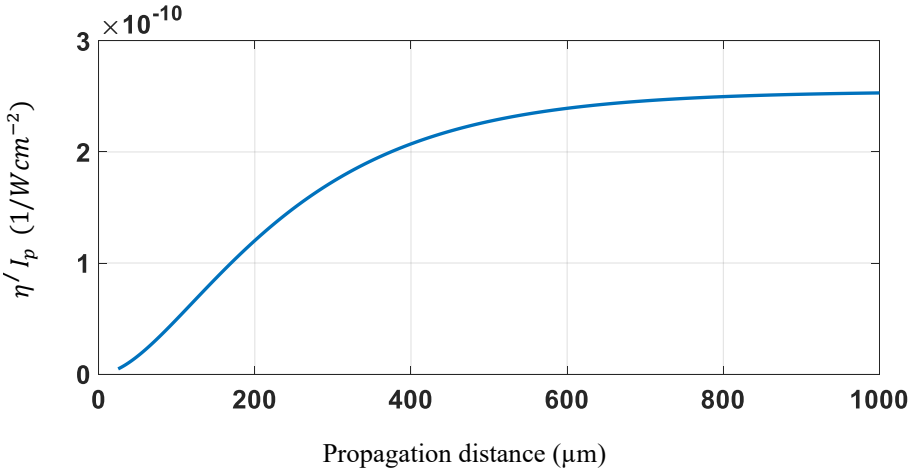

Figure 5.9: Normalized efficiency η/I_p

This efficiency could be higher if pump depletion is assumed. Practically, the propagation loss of metallic nanowires, e.g. silver, is much less than the theoretically calculated [72]. We expect, based on the results in [72], the propagation loss in our structure be much less than theoretically calculated; this will increase the efficiency as well as the propagation length.

5.5 Conclusions

We have investigated the phase matching condition for DFG by using a composite structure of metamaterial of mixing GaAs as a nonlinear material with periodic arrays of silver nanowires. The structure exhibits extreme optical anisotropy along the principle axes due to the higher parallel polarization along the wires compared with the orthogonal polarization. Phase matching was achieved for generating tunable broad mid-infrared wavelengths from $2.8\ \mu m$ to $11\ \mu m$. The pump and the signal wavelengths lie in the spectrum range from $1\ \mu m$ to $2\ \mu m$. The absorption by metallic nanoparticles is a challenging problem in metamaterials. Here, we applied the pump wave of the shortest wavelengths, from $1\ \mu m$ to $1.2277\ \mu m$, as parallel polarized wave along the wires, in which the absorption is minimum. To shift the spectrum, the period d should be changed to larger values for the redshift and lower for the blueshift.

This investigated region of the mid-infrared from $2.8\ \mu m$ to $11\ \mu m$ is a part of the mid-infrared spectrum $3 - 20\ \mu m$, which is very interesting in science and technology. It is the wavelengths region of vibrational resonances of many molecules, making the mid-infrared sources very important in spectroscopy, chemical and biomolecular sensing. Also, it lies in the two of the optical transmission windows of the atmosphere $3 - 5\ \mu m$ and $8 - 13\ \mu m$, which are important in remote sensing.

Chapter 6

Phase-matched Mid-infrared Difference Frequency Generation Using A Nanostructured Gallium Arsenide Metamaterial with Nanoholes

Published in IEEE Photonics Journal, June 2020, Vol. 12, No. 3., 5900110
DOI:10.1109/JPHOT.2020.2992192

6.1 Abstract

Phase-matched wavelength conversion is achieved in difference frequency generation (DFG) in a structure of gallium arsenide (GaAs) with periodic arrays of nanoholes. Linear properties (refractive indices) of the structure are determined from the *S*-parameters of the structure. Finite difference time domain (FDTD) simulation is used to calculate the *S*-parameters. The longest wavelength achieved is 16.2229 μm and the shortest is 3.2961 μm. The results of the FDTD simulation are compared with results obtained from the effective medium theory by using the Maxwell Garnett model. The comparison shows excellent agreement.

6.2 Introduction

Due to the vibrational transition of many molecules, the mid-infrared (mid-IR) spectral region is an interesting area of spectroscopy. Nonlinear optical difference frequency conversion is one of the most functional techniques for generating coherent, broad, and discrete light sources for spectroscopy in the mid-IR region [4]. Mid-IR conversion via DFG involves a coupling between two waves with different frequencies to generate a difference frequency through a nonlinear medium.

Most available difference frequency generation methods based on parametric wavelength conversion use nonlinear crystals, such as periodically poled lithium niobate (PPLN), potassium titanly phosphate (KTP), and barium borate (BBO) [10], [11]. Birefringence phase matching and quasi-phase matching techniques are used to achieve

efficient conversion [8], [73], [74]. Semiconductors, of special interest for monolithic integration, have greater optical nonlinearity properties than commonly used crystals such as PPLN, KTP, and BBO. GaAs, with its wide transparent optical window, from 1 μm to 17 μm, is the best choice for mid-infrared conversion using difference frequency generation [13], [14], [34], [60]. Phase matching between the waves to be mixed is a crucial factor for strong coupling and efficient frequency conversion. Unfortunately, it is not possible to achieve phase matching for DFG in GaAs, due to its natural isotropic properties. This problem can be solved via a multilayered structure of GaAs with other materials. Different approaches to achieve phase matching in GaAs structures include quasi-phase matching[15][16], modal phase matching [75][76], Bessel laser beam phase matching [17], and suspended GaAs waveguides [18].

Birefringence phase matching based on artificial anisotropy properties is possible. Artificial anisotropy properties in semiconductors were first proposed with multilayered GaAs/AlAs [21], and relatively large birefringence has been demonstrated for a multilayered GaAs/AlAs structure [22]–[24]. Tunable wavelengths from 6.7 μm to 12.7 μm using quasi-phase matching have been demonstrated in orientation-patterned GaAs [19]. Wavelengths from 7.5 μm to 8.5 μm were generated through a multilayered AlGaAs waveguide [20]. Phase-matched difference generated wavelengths from 2.8 μm to 11 μm have been achieved by using artificial birefringence in a structure of GaAs with silver nanowires [53].

In this work, we present a determination of wide, phase-matched, mid-IR generation in a structure of GaAs with nanoholes. FDTD simulation with the RSoft tool is used to calculate the scattering (*S*) parameters of the structure. Refractive indices are determined from the *S*-parameters by using a retrieving algorithm. This type of structure can be fabricated via a metal-assisted chemical etching technique [77]–[79].

6.3 Wave Mixing and Phase Mismatch

Difference frequency generation employs the difference in frequency of two waves applied through an optical nonlinear medium. The two waves are defined as a pump wave of frequency ω_p , electric field E_p, and wave vector k_p, and a signal wave of frequency ω_s, electric field E_s ,and wave vector k_s. The difference frequency wave that is generated is

referred to as an idler wave of frequency ω_i, electric field E_i, and wave vector k_i, where $\omega_p > \omega_s > \omega_i$. In this study, the nonlinear medium used is a nanostructured GaAs metamaterial with two-dimensional square arrays of cylindrical nanoholes, with period d and radius r, as shown in Fig. 6.1 (a). The structure has a length L along the direction of wave propagation. Fig.6.2(b) shows the wave propagation directions k_p, k_s, and k_i, and the polarization orientations of the waves with respect to the GaAs crystal axes. The basic unit cell of the structure is illustrated in Fig.6.1(c).

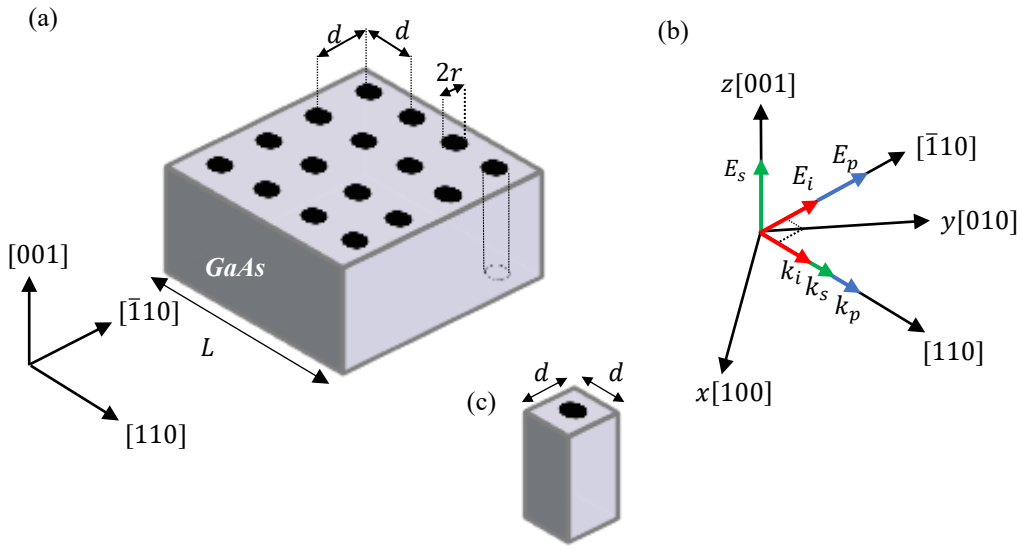

Figure 6.1: (a) GaAs structure with nanoholes of period d and radius r. The structure has a length L along the direction of wave propagating. (b) Illustration of Miller indices of the GaAs lattice structure with Cartesian coordinates, wave propagation directions, and polarizations. (c) Unit cell of the structure.

By considering the colinear wave vectors of the interacting waves and accordance with the conservation laws of energy and momentum of the photons, $\omega_i = \omega_p - \omega_s$ and $k_i = k_p - k_s$, respectively, the colinear phase mismatching is defined as

$$\Delta k = n_p \frac{\omega_p}{c} - n_s \frac{\omega_s}{c} - n_i \frac{\omega_i}{c} \tag{6.1}$$

where $k_p = n_p \frac{\omega_p}{c}$, $k_s = n_s \frac{\omega_s}{c}$, and $k_i = n_i \frac{\omega_i}{c}$. n_p, n_s, and n_i are the refractive indices at the frequencies ω_p, ω_s, and ω_i, respectively. Based on this structure, only Type-II

coupling interaction satisfies the phase matching condition. Type-II coupling is a polarization configuration where the signal and idler polarizations are orthogonal; while in type-I, the signal and the idler polarizations are parallel. Based on Type-II polarizations, we consider the applied waves at normal incidence to the holes, with electric field polarized parallel($E_{\parallel}$) to the holes along $[001]$ for the signal wave E_s, and polarized orthogonal ($E_{\perp}$)to the holes along $[\bar{1}10]$ for the pump wave E_p. Based on nonzero elements of second-order susceptibilities of GaAs $\chi_{xyz}^{(2)} = \chi_{yzx}^{(2)} = \chi_{zxy}^{(2)}$ [6], the resultant difference wave of electric field E_i will be polarized orthogonal to the holes along $[\bar{1}10]$. The three waves propagate in the plane xy, making an angle of 45° with respect to the x and y axes. The orthogonal polarizations waves have the electric field oriented parallel to the xy plane, which thus has components in x the and y directions.

It is essential to know the effective refractive indices of a structure in order to determine the phase matching. There are two main approaches for finding the effective refractive indices of metamaterial structures. The first is to use effective medium theories[25], where the long wavelength limit should be satisfied. The second is to retrieve the refractive indices from the *S*-parameters [50], [51], or from the reflection and transmission coefficients [57]. In this work, the retrieving technique is the main method employed, while the effective medium theory is used for comparison purposes.

6.4 Computing Linear Properties of The Structure from *S*-Parameters by Using The retrieval Technique

Full wave simulation using FDTD is applied to determine the *S*-parameters of the structure. To find the *S*-parameters of a metamaterial structure via full wave simulation, it is necessary to use a thin slab of the structure and to characterize it as an effective homogeneous medium[25], [50], [51]. If the structure is periodic, usually a single cell is selected as the thinnest slab. For an incident plane wave normal to the structure, the *S*-parameters are Related to the refractive index n in accordance with the following equations [50]:

$$Re(n) = \pm Re\left\{\frac{1}{k_o L} cos^{-1}\left(\frac{1}{2S_{21}^2}[1 - S_{11}^2 + S_{21}^2]\right)\right\} + \frac{2m\pi}{k_o L} \tag{6.2}$$

$$Im(n) = \pm Im\left\{\frac{1}{k_o L} cos^{-1}\left(\frac{1}{2S_{21}^2}[1 - S_{11}^2 + S_{21}^2]\right)\right\} \tag{6.3}$$

Here L is the slab length, where $L = d$ if a single cell is considered. k_o is the wave number of the incident wave in free space and m is an integer number. Due to the symmetry properties of the slab, $S_{22} = S_{11}$and $S_{12} = S_{21}$. Because the structure is passive, with no negative index elements, the signs in Eq. (6.2) and Eq. (6.3) are determined so as to obtain positive real and imaginary values. Based on the long wavelength limit for metamaterials ($d, r \ll \lambda$) and achieving phase matching, the hole periods are almost in the range between $d = 115$ nm to 140 nm and the corresponding hole radius between $r = 0.1\,d$ to $0.25\,d$.

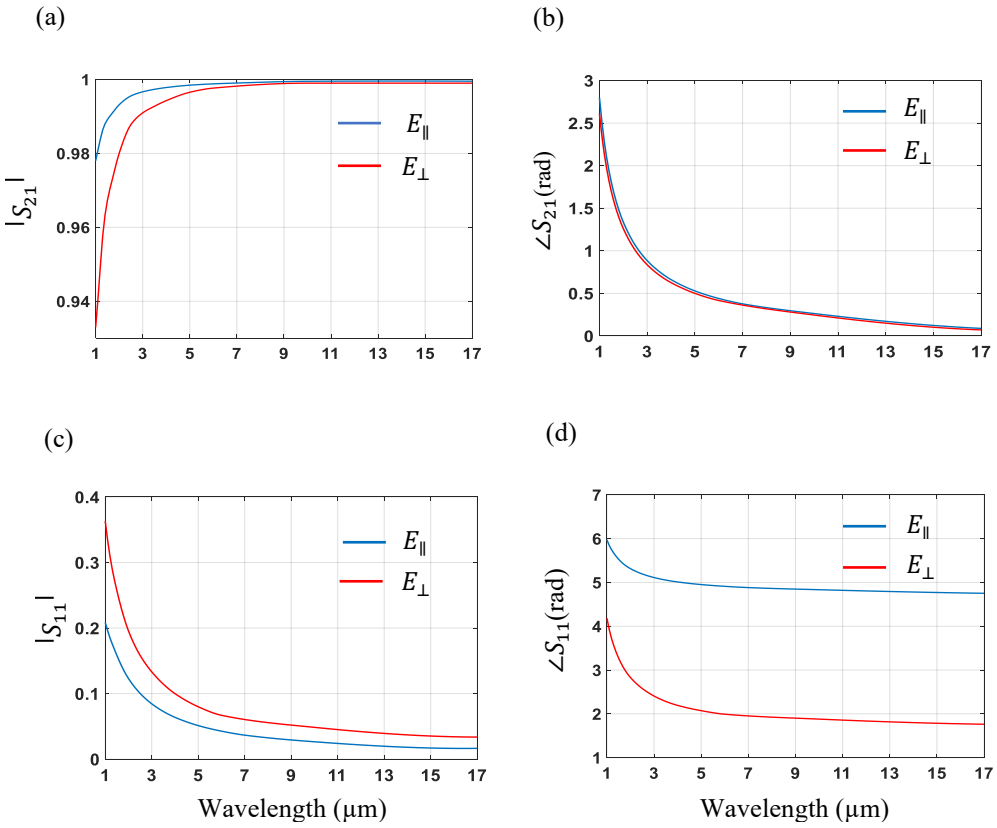

Figure 6.2: *S*-parameters at $d = 140$ nm and $r = 35$ nm, for parallel polarization $E_\parallel$ and orthogonal polarization $E_\perp$. (a) Magnitude of S_{21}. (b) Phase of S_{21}. (c) Magnitude of S_{11}. (d) Phase of S_{11}.

The *S*-parameters are computed by using a FDTD simulation of a thin one-cell layer of the structure, for incident waves polarized parallel and orthogonal to the holes, in the

entire spectrum of the GaAs optical transmission window, $\lambda = 1$ μm to 17 μm. Transverse periodic boundary conditions were applied in the direction perpendicular to the propagation direction of the incident waves. Experimentally measured data for the refractive index of GaAs [60] were used in the FDTD simulation.

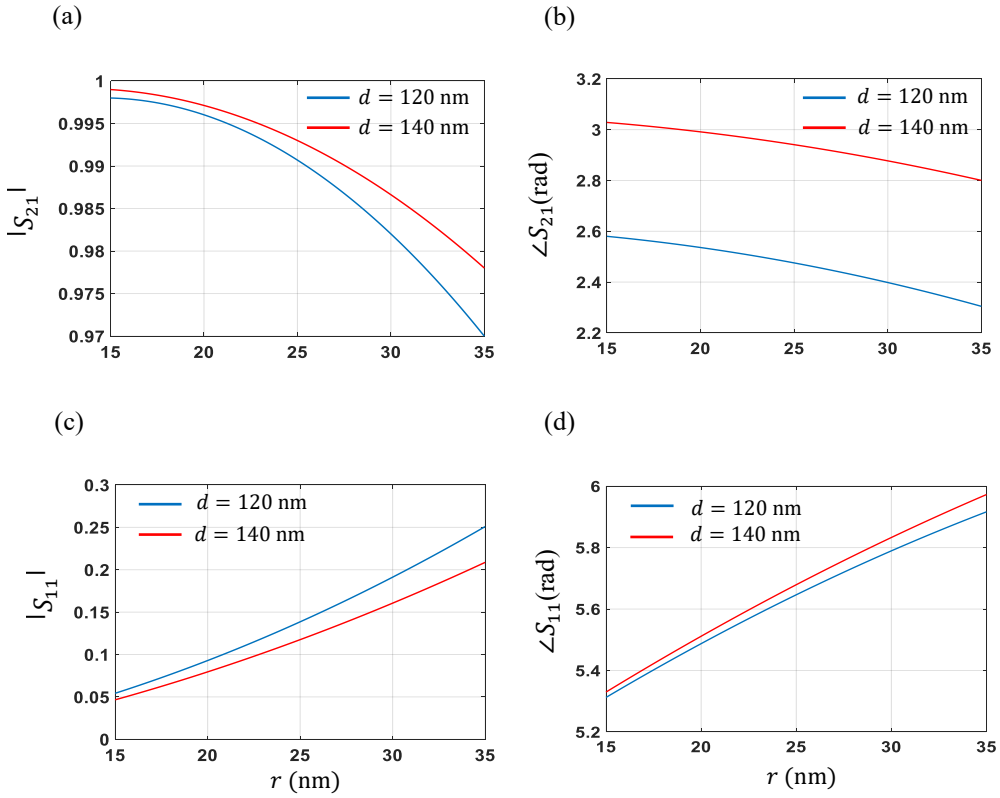

Fig.6.3: S-parameters as a function of r for parallel polarization $E_{\parallel}$ at $\lambda = 1$ μm, for $d = 120$ nm and 140 μm. (a) Magnitude of S_{21} (b) Phase of S_{21} (c) Magnitude of S_{11} and (d) Phase of S_{11}.

Fig.6.2 shows computed S-parameters of the structure, magnitude and phase, for the period $d = 140$ nm and radius $r = 35$ nm. The structure exhibits slightly more reflection with orthogonal polarization than parallel polarization, and greater transmission with parallel polarization than orthogonal polarization. As the wavelength increases, the transmission increases and the reflection decreases. Fig. 6.3 shows the S-parameters, magnitude and phase, as a function of r at $\lambda = 1$ μm for two different periods: $d = 120$ nm and 140 nm.

Since GaAs is nonadsorbing in its optical window, only real indices of the structure exist. Fig. 6.4 shows two retrieved real indices, $Re(n^{\parallel})$ and $Re(n^{\perp})$, computed from the S-parameters presented in Fig.6.2. $Re(n^{\parallel})$ represents the index parallel to the longitudinal axis of the nanoholes, and $Re(n^{\perp})$ represents the index perpendicular to the longitudinal axis of the nanoholes. The contrast between the indices, $Re(n^{\parallel})$ and $Re(n^{\perp})$ indicates that GaAs with nanoholes acts as an anisotropic medium. This promises well for birefringence phase matching in the structure.

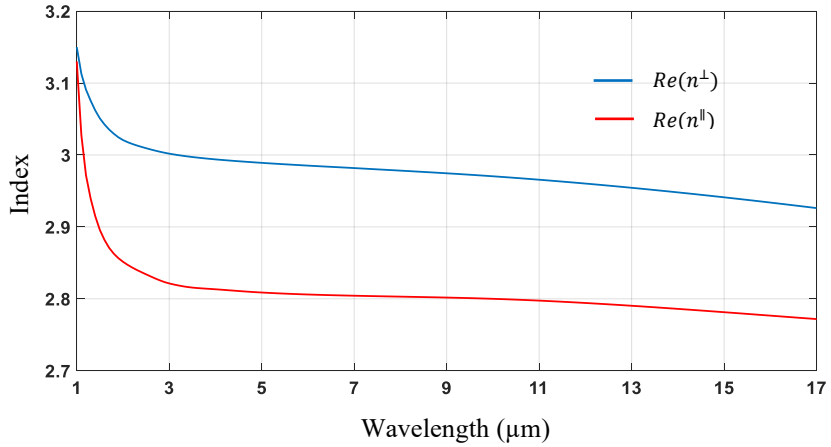

Figure 6.4: Real refractive indices $Re(n^{\parallel})$ and $Re(n^{\perp})$ at $d = 140$ nm and $r = 35$ nm.

Varying the parameters of the structure, d or r, will not change the refractive index profiles shown in Fig.6. 4; however, the values will be changed. Lowering the values of the indices relative to the GaAs index can be done by increasing the volume fraction of the nanoholes inside the structure. This can be achieved either by decreasing d or increasing r. Figures 6.5(a) and 6.5(b) show the refractive indices of the structure in relation to the GaAs index, for two different periods: $d = 120$ nm and 140 nm, and a radius of $r = 35$ nm.

Figure 6.6 illustrates the two-dimensional electric field distribution for the parallel polarization $E_{\parallel}$ and the orthogonal polarization $E_{\perp}$, at $d = 140$ nm and $a = 35$ nm, for $\lambda = 1$ μm

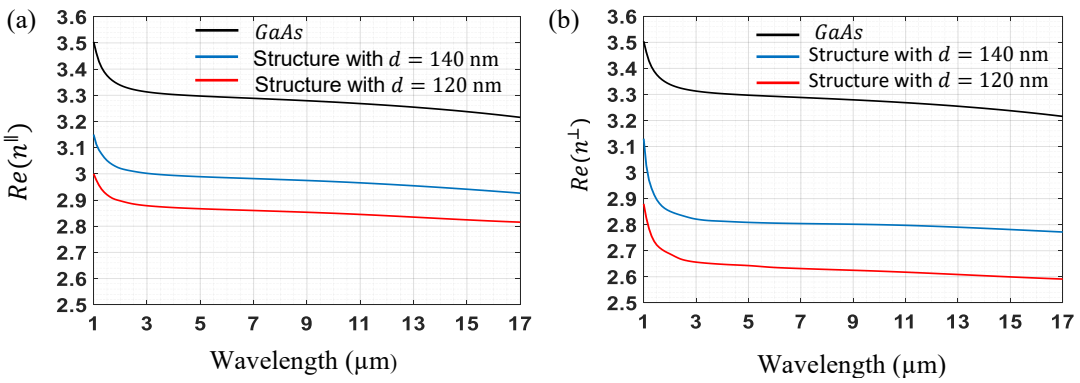

Figure 6.5: Real retrieved indices at $r = 35$ nm for periods $d = 120$ and 140 nm compared with GaAs refractive index. (a) Parallel index $Re(n^{\parallel})$. (b) Perpendicular index $Re(n^{\perp})$.

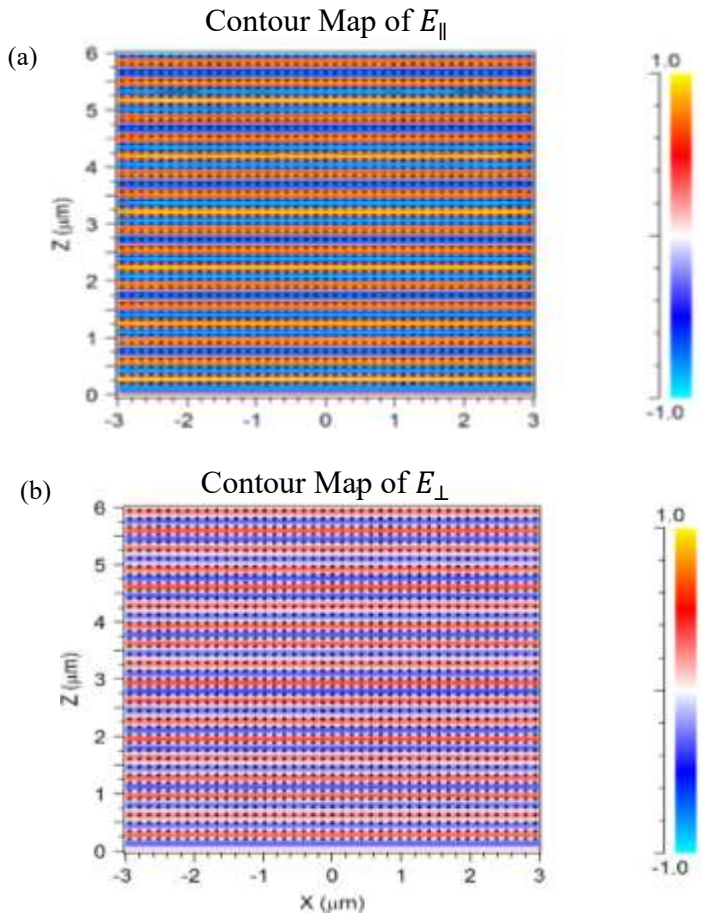

Figure 6.6: Field distribution at $d = 140$ nm and $a = 35$ nm, and $\lambda = 1$ μm. (a) Parallel polarization to the wires $E_{\parallel}$. (b) Orthogonal polarization to the wires $E_{\perp}$.

The field distribution was obtained using FDTD simulation by applying a plane wave of unity intensity. Additional details on FDTD simulation using the RSoft tool are given in Appendix A. The distribution illustrated in Fig. 6.6(a) is of $E_{\parallel}$, which shows that the parallel field is stronger than the orthogonal field $E_{\perp}$ depicted in Fig. 6.6(b).

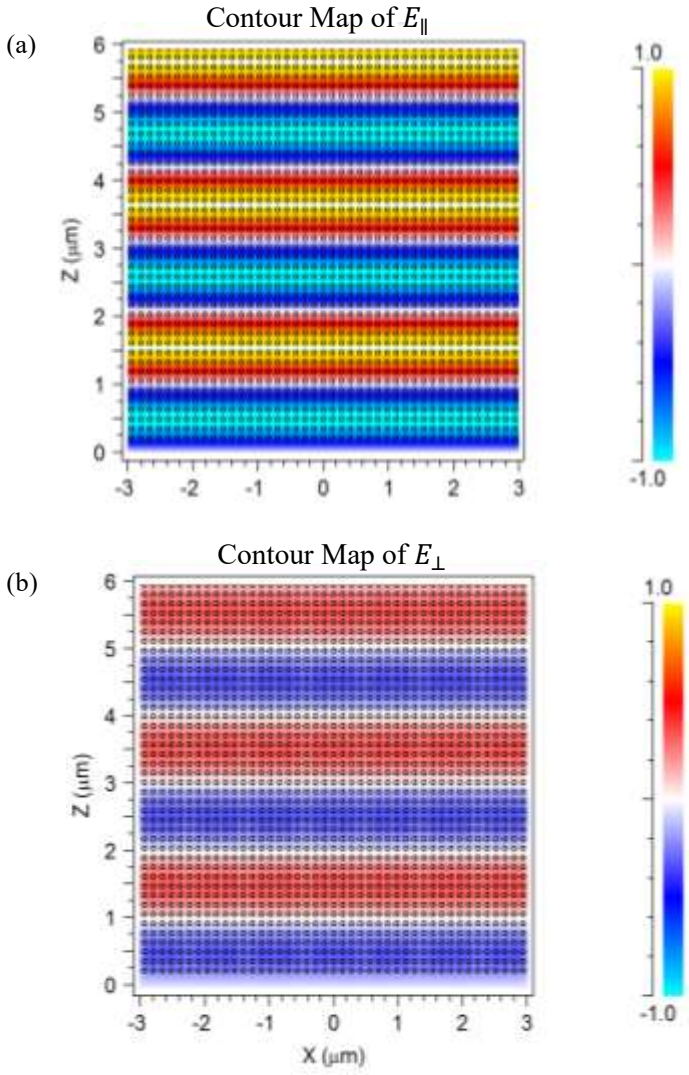

Figure 6.7: Field distribution at $d = 140$ nm and $a = 35$ nm, and $\lambda = 6$ μm. (a) Parallel polarization to the wires $E_{\parallel}$. (b) Orthogonal polarization to the wires $E_{\perp}$.

The distribution also indicates that the wavelengths inside the structure for $E_{\parallel}$ and $E_{\perp}$ of the corresponding free space incident wavelengths, $\lambda = 1$ μm, became shorter, with values of 0.32 μm and 0.31 μm, respectively. As a result, the effective refractive indices are 3.1

and 3.2 for $E_{\parallel}$ and $E_{\perp}$, respectively. Figure 6.7 displays $E_{\parallel}$ and $E_{\perp}$ fields distribution, at $d = 140$ nm and $a = 35$ nm, for $\lambda = 6$ μm, which shows that $E_{\parallel}$ is more intensive than $E_{\perp}$. The distribution indicates that the wavelengths inside the structure for $E_{\parallel}$ and $E_{\perp}$ are of the corresponding free space incident wavelengths, $\lambda = 6$ μm, became shorter, with values of 2.15 μm and 2μm, respectively. As a result, the effective refractive indices are 2.79 and 3 for $E_{\parallel}$ and $E_{\perp}$, respectively. The determined refractive indices from the wavelengths of the fields distribution inside the structure, at $\lambda = 1$ μm and $\lambda = 6$ μm, agree with the those retrieved from the *S*-parameters, that are shown in Fig. 6.4.

6.5 Achieving Birefringence Phase Matching in The Structure

Changing the optical properties of GaAs from isotropic to anisotropic through the inclusion of nanoholes is beneficial, since it permits the use of birefringence phase matching in the GaAs medium. The structure was tested for phase matching possibilities by varying the pump frequency, ω_p, and the signal frequency, ω_s. The difference frequency, ω_i, is assigned in accordance with energy and momentum conservation laws. The refractive indices plotted in Fig. 6.4 were applied in the phase mismatching relation given in Eq. (6.1). n_p and n_i correspond to the perpendicular index $n^{\perp}$, and n_s to the parallel index $n^{\parallel}$. Fig. 6.6 plots the mismatch function $(\Delta k/k_p)$ for three different pump wavelengths: $\lambda_p =$ 1.0333 μm, 1.1171 μm, and 1.3053 μm. k_p is the wave number of the pump wave at the selected λ_p. Each plot satisfies the energy conservation law. Momentum conservation is satisfied at phase matching $(\Delta k = 0)$. Figures 6.8 (a) and 6.8 (b) plot $(\Delta k/k_p)$ as a function of the idler wavelength, λ_i, and the signal wavelength, λ_s, respectively, at the specified pump wavelengths, λ_p. For these selected cases, the idler wavelengths at phase matching are $\lambda_i = 15.5875$ μm, 5.7537 μm, and 3.3195 μm, and the corresponding signal wavelengths are $\lambda_s = 1.067$ μm, 1.3863 μm, and 2.1511 μm, respectively. The structure was scanned for the entire GaAs transmission spectrum, from $\lambda = 1$ μm to $\lambda =$ 17 μm. The phase-matched wavelength curves, or tuning curves, that relate the three wavelengths λ_p, λ_s, and λ_i, are shown in Fig. 6.9. The tuning curves in Fig. 6.9 show that the pump wavelength, λ_p, extends from 1.0333 μm to 1.3983 μm. The signal wavelength, λ_s, ranges from 1.1067 μm to 2.7932 μm, and the idler wavelength, λ_i, ranges from

15.5875 µm to 2.8001 µm. This generated idler wavelength band is broad, continuous, and tunable through tuning of the input pump and/or signal wavelengths. The band can be redshifted or broadened by increasing d or decreasing r, or vice versa

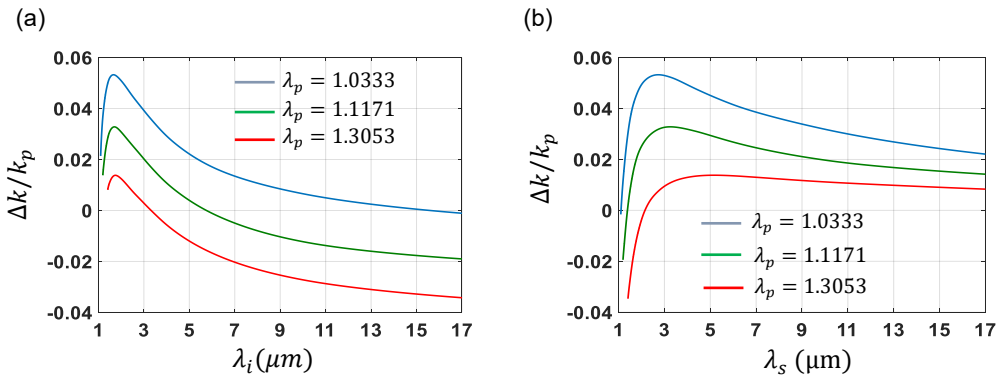

Figure 6.8: Mismatch function $(\Delta k/k_p)$ for three different pump wavelengths: $\lambda_p =$ 1.0333 µm, 1.1171 µm, and 1.3053 µm, at $d = 140$ nm and $r = 35$ nm. (a) $(\Delta k/k_p)$ as a function of the idler wavelength, λ_i, with phase-matched idler wavelengths: $\lambda_i =$ 15.5875 µm, 5.7537 µm, and 3.3195 µm. (b) $(\Delta k/k_p)$ as a function of the signal wavelength, λ_s, with the corresponding phase-matched signal wavelengths: $\lambda_s =$ 1.067 µm, 1.3863 µm, and 2.1511 µm.

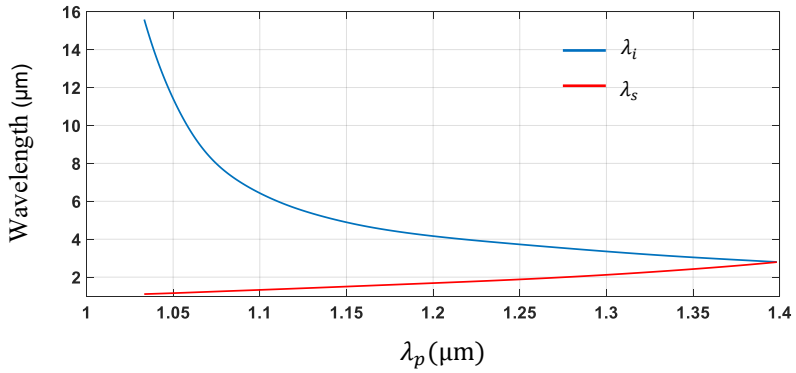

Figure 6.9: Phase-matched wavelength curves, or tuning curves, that relate idler wavelengths, λ_i, and signal wavelengths, λ_s to pump wavelengths, λ_p, at $d = 140$ nm and $r = 35$ nm.

.

Fig. 6.10 shows different phase-matched wavelength curves, or tuning curves, for idler and signal wavelengths as a function of the pump wavelength, at different values of r and d. The curves for different r and d values are plotted in different colors, while the idler wavelength curves are represented by dashed lines and the signal wavelength curves by

solid lines. As r decreases, the idler and signal wavelengths are broadened and redshifted. For example, for $d = 120$ nm and $r = 35$ nm (shown in black), the longest idler wavelength is 4.633 μm and the shortest is 2.4612 μm. However, if r is decreased to 25 nm, with d remaining at 120 nm (shown in green), the longest idler wavelength is 6.6704 μm and the shortest is 2.8993 μm.

The idler wavelengths are broadened considerably more by an increase in d than by a decrease in r, as shown by the green and blue dashed curves, which correspond to $d = 120$ nm and 140 nm, respectively, with r remaining constant at 25nm . At $d = 140$ nm, the longest idler wavelength is 16.2229 μm, as compared to 6.6704 μm at $d = 120$ nm.

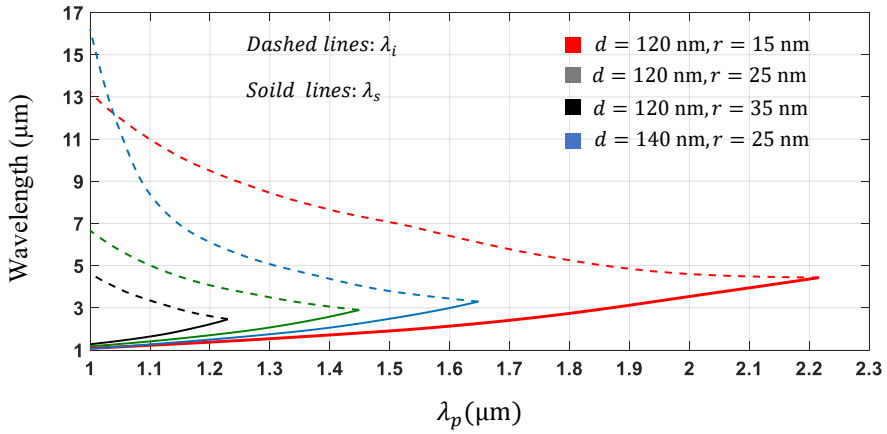

Figure 6.10: Phase-matched wavelength curves that relate λ_i and λ_s to λ_p, at different values of d and r. The signal wavelengths, λ_s, are represented by solid lines, while the idler wavelengths, λ_i, are represented by dashed lines. The colors red, green, and black correspond to $d = 120$ nm with $r = 15$ nm, 25 nm, and 35 nm, respectively. The color blue corresponds to $d = 140$ nm with $r = 25$ nm.

Nonlinear conversion processes are generally very weak due to small nonlinear coefficients of materials. Phase matching and longer interaction length will increase the efficiency. The conversion efficiency at phase matching ($\Delta k = 0$) for nondepleted pump assumption is given by[18], [71] :

$$\eta = \frac{P_i}{P_s} = \frac{8\pi^2 d_{eff}^{(2)} L^2 I_p}{\varepsilon_o n_p n_s n_i c \lambda_i^2} \tag{6.4}$$

P_i and P_s are the idler and signal powers, respectively, and I_p is the pump intensity; n_i,

n_s, and n_p are their refractive indices. Fig. 6.11 shows the efficiency $\eta[\%]$ versus the interaction length L, at the case $d = 140$ nm and $r = 35$ nm, with the following parameters at the phase matching condition: $\lambda_i = 15.5875\,\mu m$, $n_p = 3.0918, n_s = 3.1107$, $n_i = 2.8369$, and $d_{eff}^{(2)} = 370$ pm/V, with assumption $I_p = 1kW/cm^2$. The efficiency increases parabolically with the interaction length and linearly with the pump intensity. Longer interaction medium or more pump intensity will boost the generated idler wave.

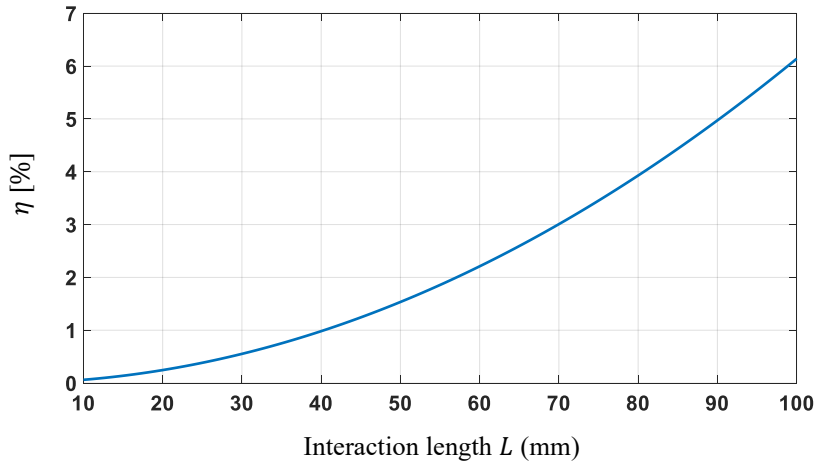

Figure 6.11: Efficiency $\eta[\%]$ versus the interaction length L for $I_p = 1kW/cm^2$.

6.6 Comparison with Effective Medium Theory Results

Effective medium theory provides a permittivity mixing formula that uses a quasi-static approximation approach to find the effective permittivity of a composite structure consisting of particles of different materials. In this study the Maxwell Garnett approximation was used to determine the effective permittivities parallel to, $\varepsilon_{\parallel}^{eff}$, And perpendicular to, $\varepsilon_{\perp}^{eff}$, the nanoholes of the structure illustrated in Fig.6.1 (a). To consider the two components of the metamaterial: GaAs and nanoholes, the following Maxwell Garnett formulas were used[28], [80]:

$$\varepsilon_{\parallel}^{eff} = f + (1-f)\varepsilon \tag{6.5a}$$

$$\varepsilon_{\perp}^{eff} = \varepsilon + \frac{2f\varepsilon\,(1-\varepsilon)}{2\varepsilon + (1-f)(1-\varepsilon)} \tag{6.5b}$$

Here f is the volume fraction of the nanoholes included in the GaAs medium, where $0 \leq f \leq 1$, $f = \pi r^2/d^2$, and ε is the permittivity of the GaAs. The experimental data used for the GaAs refractive index [60] were the same as those used in the FDTD simulation. In order to examine the phase matching aspect, it is necessary to take into account the effective refractive indices, $n_{\parallel}^{eff} = Re\left(\pm\sqrt{\varepsilon_{\parallel}^{eff}}\right)$ and $n_{\perp}^{eff} = Re\left(\pm\sqrt{\varepsilon_{\perp}^{eff}}\right)$. The square root has two possible solutions, positive and negative (corresponding to a negative refractive index). Because the structure does not include any negative index materials, the positive solution was selected. Fig. 6.12 compares the refractive indices obtained by using the FDTD simulation with those obtained via the Maxwell Garnett theory. One set of parameters was chosen to show: $d = 140$ nm with $r = 25$ nm for the FDTD simulation and the corresponding $f = 0.1002$ for the Maxwell Garnett.

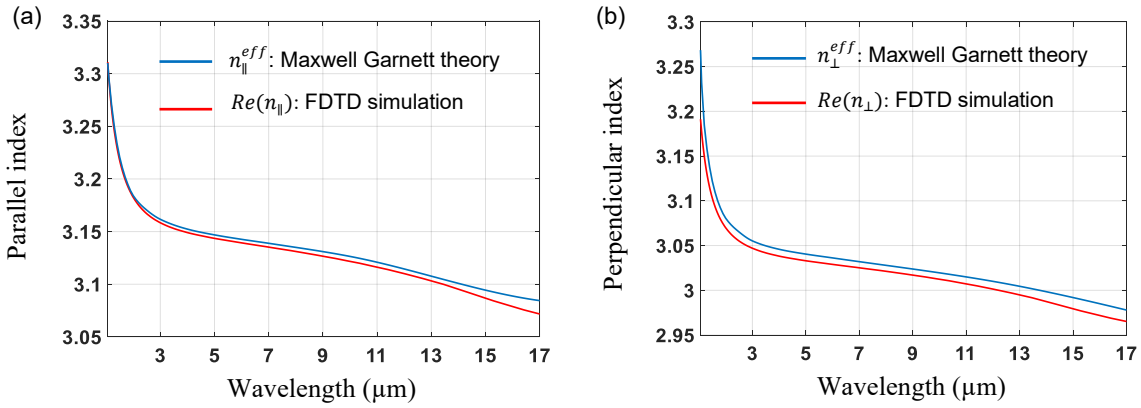

Figure 6.12: Comparison of refractive indices obtained from the FDTD simulation and the Maxwell Garnett theory. (a) and (b) Parallel and perpendicular indices, respectively, at $d = 140$ nm and $r = 25$ nm for the FDTD simulation, and at the corresponding $f = 0.1002$ for the Maxwell Garnett theory.

The comparison shows good agreement in the profiles, with slight disagreement in the magnitudes, seen slightly more for the perpendicular index. This slight disagreement is due to the fact that the Maxwell Garnett theory uses the proximation of the quasi-static approach while FDTD is full wave simulation.

6.7 Conclusions

The phase matching condition for DFG hast been investigated by using a nonlinear optical structure comprised of a GaAs with inclusions of periodic arrays of nanoholes. This structure, to our knowledge, has never been investigated for phase matching. FDTD simulation was used to determine the scattering (*S*) parameters of the composite structure. Linear properties (refractive indices) of the structure were then extracted from the *S*-parameters by using a retrieving algorithm. The structure exhibits optical anisotropy along the principal axes.

Phase matching was found at certain range of hole periods, from $\mathrm{d} = 115\ \mathrm{nm}$ to $140\ \mathrm{nm}$, and at the corresponding radius from $\mathrm{r} = 0.1\mathrm{d}$ to $0.25\mathrm{d}$. The generated mid-IR is broad and tunable through tuning of the input pump and/or signal wavelengths. The generated phase matched spectrum from 3.2961 μm to 16.2229 μm was achieved at $\mathrm{d} = 140\ \mathrm{nm}$ and $\mathrm{r} = 25\mathrm{nm}$. The pump and signal wavelengths are in the spectral range less than 3 μm. For comparison with the FDTD simulation results, the Maxwell Garnett theory was used to determine effective permittivities, the comparison shows an excellent agreement.

Chapter 7

Conclusions

The purpose of this study was to find a nanostructure that consists of GaAs and another material, so that the resultant structure behaves as an anisotropic medium to apply BPM for the DFG of the optical frequency conversion. The goal was to generate broad and frequency-tunable phase-matched mid-IR frequencies. The following section summarizes the results of this work.

7.1 Summary

A nanostructure of GaAs and periodic arrays of silver nanowires was characterized and analyzed by finding its refractive and absorption indices from *S*-parameters computed using an FDTD simulation. A retrieving method was used to extract the indices from the *S*-parameters. The characterization showed that the structure exhibits extreme optical anisotropy along its principal axes and possesses a near-IR transparency region in the fields parallel to the wires, and near- and mid-IR transparency regions in the orthogonal fields. Within these frequency regions, the structure acts as a dielectric with minimum ohmic loss. The regions were utilized to apply one of the interacting waves of near-IR frequency with polarization along the wires, while the other near- and mid-IR frequencies were orthogonally polarized to the wires in order to use BPM. A Drude model for metal wires media was employed for comparative purposes only in order to verify the results obtained by FDTD simulation.

In the study, a silver nanowire structure with GaAs was investigated for phase matching. The phase matching was achieved for generating tunable broad mid-infrared wavelengths from 2.8 μm to 11 μm at a wire period of 350 nm and a diameter of 35 nm. The pump and the signal wavelengths lie in the spectrum range from 1 μm to 2 μm. To shift the spectrum, the period of the wires should be changed to larger values for the redshift and lower ones for the blueshift. However, increasing or decreasing the wire period above or below certain values might lead to loss of phase matching. Even though the structure

has minimum loss at certain near-IR frequencies of parallel fields, the metal wires are still there, and the absorption is accumulated along the propagation distance.

A structure of GaAs with inclusions of periodic arrays of longitudinal nanoholes was characterized and investigated for phase matching DFG. An FDTD simulation was applied to a slab of the structure to compute the structure's *S*-parameters, after which the refractive indices were extracted from the *S*-parameters using a retrieving method. The structure exhibited optical anisotropy along the principal axes with transparency regions, which is the same as GaAs from 1 μm to 17 μm for electric fields parallel and orthogonally polarized to the wires. The phase matching was achieved only at a certain range of hole periods, from 115 nm to 140 nm, and at the corresponding radius from one-tenth to one-quarter of the hole period. The generated mid-IR is broad and frequency-tunable by varying the pump and/or signal frequencies.

A generated phase-matched spectrum from 3.2961 μm to 16.2229 μm was achieved at a period of 140 nm and a radius of 25 nm. The longest achieved wavelength can be shifted to longer values if the hole periods increase or the radius decreases. To enable a comparison with the FDTD simulation results, the Maxwell Garnett theory was used to determine effective permittivity, with the comparison showing excellent agreement.

The nanohole structure is much more practical than the silver nanowires, due to its lossless properties and longer mid-IR frequencies achievement. Furthermore, it is free of any plasma resonance which might occur in the wire media at certain wire media.

7.2 Future Work

Based on the results of the present study, the following research could be carried out in relation to this work:

1. Fabricating the structure of GaAs with longitudinal holes is highly recommended. The structure promises practical considerable phase-matching achievements for DFG.
2. Investigating the structure of GaAs with nanoholes as a waveguide medium for phase matching in DFG.

Bibliography

[1] J. A. Armstrong, N. Bloembergen, J. Ducuing, and P. S. Pershan, "Interactions between light waves in a nonlinear dielectric," *Phys. Rev.*, vol. 127, no. 6, pp. 1918–1939, 1962.

[2] P. A. Franken, A. E. Hill, C. W. Peters, and G. Weinreich, "Generation of optical harmonics," *Phys. Rev. Lett.*, vol. 7, no. 4, pp. 118–119, 1961.

[3] A. Schliesser, N. Picqué, and T. W. Hänsch, "Mid-infrared frequency combs," *Nat. Photonics*, vol. 6, no. 7, pp. 440–449, 2012.

[4] M. Vainio and L. Halonen, "Mid-infrared optical parametric oscillators and frequency combs for molecular spectroscopy," *Phys. Chem. Chem. Phys.*, vol. 18, no. 6, pp. 4266–4294, 2016.

[5] G. D. Boyd and D. A. Kleinman, "Parametric interaction of focused Gaussian light beams," *J. Appl. Phys.*, vol. 39, no. 8, pp. 3597–3639, 1968.

[6] R. W. Boyd, *Nonlinear Optics*. Elsevier Inc., 2008.

[7] W. Chen *et al.*, "Continuous-wave mid-infrared laser sources based on difference frequency generation," *Comptes Rendus Phys.*, vol. 8, no. 10, pp. 1129–1150, 2007.

[8] L. E. Myers *et al.*, "Quasi-Phasematched Optical Parametric Oscillators in Periodically Poled LiNbO_3," *Opt. Photonics News*, vol. 6, no. 12, p. 30, 1995.

[9] D. S. Hum and M. M. Fejer, "Quasi-phasematching," *Comptes Rendus Phys.*, vol. 8, no. 2, pp. 180–198, 2007.

[10] M. Cada, H. J., R. Normandin, H. Dai, and S. Janz, "Optical nonlinear devices," *Int. J. Nonlinear Opt. Phys*, vol. 3, no. 2, pp. 169–203, 1994.

[11] S. J. Wagner *et al.*, "Difference Frequency Generation by Quasi-Phase Matching in Periodically Intermixed Semiconductor Superlattice Waveguides," *IEEE J. Quantum Electron.*, vol. 47, no. 6, pp. 834–840, 2011.

[12] J. Garrison, R. Chiao, J. C. Garrison, and R. Y. Chiao, "Linear optical devices," *Quantum Opt.*, vol. 38, no. 8, pp. 237–264, 2008.

[13] M. Cada, "Optical harmonic mixers - Quantum Electronics, IEEE Journal of," vol. 31, no. 2, 1995.

[14] A. S. Helmy *et al.*, "Recent advances in phase matching of second-order nonlinearities in monolithic semiconductor waveguides," *Laser Photonics Rev.*, vol. 5, no. 2, pp. 272–286, 2011.

[15] S. J. B. Yoo, C. Caneau, R. Bhat, M. A. Koza, A. Rajhel, and N. Antoniades, "Wavelength conversion by difference frequency generation in AlGaAs waveguides with periodic domain inversion achieved by wafer bonding," *Appl. Phys. Lett.*, vol. 2609, no. 1996, p. 2609, 1995.

[16] A. Grisard, E. Lallier, and B. Gérard, "Quasi-phase-matched gallium arsenide for versatile

mid-infrared frequency conversion," *Opt. Mater. Express*, vol. 2, no. 8, 2012.

[17] P. Liu, W. Shi, D. Xu, X. Zhang, G. Zhang, and J. Yao, "Efficient phase-matching for difference frequency generation with pump of Bessel laser beams," *Opt. Express*, vol. 24, no. 2, p. 901, 2016.

[18] T. Stievate *et al.*, "Mid-infrared difference-frequency generation in suspended GaAs waveguides," *Opt. Lett.*, vol. 39, no. 4, pp. 945–948, 2014.

[19] C. R. Phillips *et al.*, "Widely tunable midinfrared difference frequency generation in orientation-patterned GaAs pumped with a femtosecond Tm-fiber system," *Opt. Lett.*, vol. 37, no. 14, p. 2928, 2012.

[20] D. F. Logan, M. Giguere, A. Villeneuve, and A. S. Helmy, "Widely tunable mid-infrared generation via frequency conversion in semiconductor waveguides," *Opt. Lett.*, vol. 38, no. 21, p. 4457, 2013.

[21] J. P. Van Der Ziel, M. Ilegems, and R. M. Mikulyak, "Optical birefringence of thin GaAs-AlAs multilayer films," *Appl. Phys. Lett.*, vol. 28, no. 12, pp. 735–737, 1976.

[22] A. Fiore *et al.*, "Huge birefringence in selectively oxidized GaAs/AlAs optical waveguides," *Appl. Phys. Lett.*, vol. 1320, p. 1320, 1995.

[23] E. Guillotel *et al.*, "Parametric amplification in GaAs/AlOx waveguide," *Appl. Phys. Lett.*, vol. 94, no. 17, 2009.

[24] A. Fiore, V. Berger, E. Rosencher, P. Bravetti, and J. Nagle, "Phase matching using an isotropic nonlinear optical material," *Nature*, vol. 391, no. 6666, pp. 463–466, 1998.

[25] C. Wenshan and V. Shalaev, *Optical Metamaterials: Fundamentals and Applications*. Springer, 2009.

[26] J. Elser, R. Wangberg, V. A. Podolskiy, and E. E. Narimanov, "Nanowire metamaterials with extreme optical anisotropy," *Appl. Phys. Lett.*, vol. 89, no. 26, pp. 5–7, 2006.

[27] J. Yao *et al.*, "Optical negative refraction in bulk metamaterials of nanowires," *Science (80-.).*, vol. 321, no. 5891, p. 930, 2008.

[28] Y. Liu, G. Bartal, and X. Zhang, "All-angle negative refraction and imaging in a bulk medium made of metallic nanowires in the visible region," *Opt. Express*, vol. 16, no. 20, p. 15439, 2008.

[29] A. Fang, T. Koschny, and C. M. Soukoulis, "Optical anisotropic metamaterials: Negative refraction and focusing," *Phys. Rev. B - Condens. Matter Mater. Phys.*, vol. 79, no. 24, pp. 1–7, 2009.

[30] G. New, *Introduction to Nonlinear Optics*, 1st ed. Combridge University Press, 2011.

[31] A. Yarif, *Quantum Electonics*, 3rd ed. John Wiley & Sons, 1989.

[32] P. E. Powers, *Field Guide to Nonlinear Optics*, SPIE. 2013.

[33] B. and T. M. Saleh, *Fundamentals of photonics*, 2nd ed. John Wiley & Sons, 2007.

[34] M. Cada, “Nonlinear optical devices,” *Opt. Pura y Apl.*, vol. 38, no. 3, 2005.

[35] H. Ishizuki and T. Taira, “Mg-doped congruent LiTaO3 crystal for large-aperture quasi-phase matching device,” *Opt. InfoBase Conf. Pap.*, vol. 16, no. 21, pp. 2531–2534, 2008.

[36] P. E. Powers, T. J. Kulp, and S. E. Bisson, “Continuous tuning of a continuous-wave periodically poled lithium niobate optical parametric oscillator by use of a fan-out grating design,” *Opt. Lett.*, vol. 23, no. 3, p. 159, 1998.

[37] D. R. Smith, W. J. Padilla, D. C. Vier, S. C. Nemat-Nasser, and S. Schultz, “Composite Medium with Simultaneously Negative Permeability and Permittivity,” *Phys. Rev. Lett.*, vol. 84, no. 18, pp. 4184–4187, 2000.

[38] V. G. Veselago, “THE ELECTRODYNAMICS OF SUBSTANCES WITH SIMULTANEOUSLY NEGATIVE VALUES OF ϵ AND μ,” *Sov. Phys. Uspekhi*, vol. 10, no. 4, pp. 509–514, 1968.

[39] T. C. CHOY, *Effective Medium Theory: Principles and Applications*, 2nd ed. Oxford University Press, 2016.

[40] A. Sihvola and J. A. Kong, “Effective permittivity of dielectric honeycombs,” *IEEE Trans. Geosci. Remote Sens.*, vol. 26, no. 4, pp. 420–429, 1988.

[41] A. Sihvola, “Dielectric polarization and particle shape effects,” *J. Nanomater.*, vol. 2007, 2007.

[42] C. F. BOHREN and D. R. HUFFMAN, *Absorption and Scattering of Light by Small Particles*. John Wiley & Sons, 1983.

[43] L. Novotny and B. Hecgt, *Principles of Nano-Optics*, 2nd ed. Cambridge University Press, 2012.

[44] S. A. Maier, *PLASMONICS: FUNDAMENTALS AND APPLICATIONS*. Springer, 2007.

[45] A. H. Sihvola, *Electromagnetic Mixing Formulas and Applications*. Institution of Electrical Engineers, 1999.

[46] M. Hartmann, *Light scattering by small particle*. Von H. C. VANDE HULST. New York: dover Publications, Inc, 1981.

[47] J. T. Michalak and H. Hu, “Demagnetizing Factors of the General Ellipsoid,” *P.H YS ICAL REV I EW*, vol. 67, no. 12, pp. 351–357, 1945.

[48] J. Venermo and A. Sihvola, “Dielectric polarizability of circular cylinder,” *J. Electrostat.*, vol. 63, no. 2, pp. 101–117, 2005.

[49] J. B. Pendry, A. J. Holden, W. J. Stewart, and I. Youngs, “Extremely low frequency plasmons in metallic mesostructures,” *Phys. Rev. Lett.*, vol. 76, no. 25, pp. 4773–4776, 1996.

[50] D. R. Smith, D. C. Vier, T. Koschny, and C. M. Soukoulis, “Electromagnetic parameter retrieval from inhomogeneous metamaterials,” *Phys. Rev. E - Stat. Nonlinear, Soft Matter Phys.*, vol. 71, no. 3, pp. 1–11, 2005.

[51] X. Chen, T. M. Grzegorczyk, B. I. Wu, J. Pacheco, and J. A. Kong, “Robust method to retrieve the constitutive effective parameters of metamaterials,” *Phys. Rev. E - Stat. Physics, Plasmas, Fluids, Relat. Interdiscip. Top.*, vol. 70, no. 1, p. 7, 2004.

[52] A. Rose and D. R. Smith, “Overcoming phase mismatch in nonlinear metamaterials [Invited],” *Opt. Mater. Express*, vol. 1, no. 7, p. 1232, 2011.

[53] N. A. Otman and M. Cada, “Phase Matching for Difference Frequency Generation in GaAs Via an Artificial Birefringence Technique Using Silver Nanowires,” *IEEE Photonics J.*, vol. 10, no. 3, pp. 1–10, 2018.

[54] C. R. Simovski *et al.*, “Strong spatial dispersion in wire media in the very large wavelength limit,” *Phys. Rev. B - Condens. Matter Mater. Phys.*, vol. 67, no. 11, p. 4, 2003.

[55] P. Markoš and C. M. Soukoulis, “Absorption losses in periodic arrays of thin metallic wires,” *Opt. Lett.*, vol. 28, no. 10, p. 846, 2003.

[56] G. D’Aguanno, N. Mattiucci, A. Alù, C. Argyropoulos, J. V. Foreman, and M. J. Bloemer, “Thermal emission from a metamaterial wire medium slab,” *Opt. Express*, vol. 20, no. 9, p. 9784, 2012.

[57] D. R. Smith, S. Schultz, P. Markoš, and C. M. Soukoulis, “Determination of effective permittivity and permeability of metamaterials from reflection and transmission coefficients,” *Phys. Rev. B - Condens. Matter Mater. Phys.*, vol. 65, no. 19, pp. 1–5, 2002.

[58] S. Anantha Ramakrishna, “Physics of negative refractive index materials,” *Reports Prog. Phys.*, vol. 68, no. 2, pp. 449–521, 2005.

[59] L. V. Alekseyev and E. Narimanov, “Slow light and 3D imaging with non-magnetic negative index systems,” *Opt. Express*, vol. 14, no. 23, p. 11184, 2006.

[60] T. Skauli *et al.*, “Improved dispersion relations for GaAs and applications to nonlinear optics,” *J. Appl. Phys.*, vol. 94, no. 10, pp. 6447–6455, 2003.

[61] H. U. Yang, J. D’Archangel, M. L. Sundheimer, E. Tucker, G. D. Boreman, and M. B. Raschke, “Optical dielectric function of silver,” *Phys. Rev. B - Condens. Matter Mater. Phys.*, vol. 91, no. 23, pp. 1–11, 2015.

[62] T. Suhara and M. Fujimura, *Waveguide Nonlinear-Optic Devices*, 1st ed. Springer-Verlag Berlin, 2003.

[63] M. Fox, *Optical Properties of Solids*, 1st ed. Oxford University Press, 2001.

[64] S. J. B. Yoo, R. Bhat, C. Caneau, and M. A. Koza, “Quasi-phase-matched second-harmonic generation in AlGaAs waveguides with periodic domain inversion achieved by wafer-bonding,” *Appl. Phys. Lett.*, vol. 66, no. 25, pp. 3410–3412, 1995.

[65] J. B. Pendry, A. J. Holden, D. J. Robbins, and W. J. Stewart, “Low frequency plasmons in thin-wire structures,” *J. Phys. Condens. Matter*, vol. 10, pp. 4785–4809, 1998.

[66] V. G. Dmitriev, Gurzadyan, and D. N. Nikogosyan, *Handbook of Nonlinear Optical Crystals*, Third Revi. Springer, 1999.

[67] S. Shingubara, “Fabrication of Nanomaterials Using Porous Alumina Templates,” *J. Nanoparticle Res.*, vol. 5, no. 3, pp. 17–30, 2003.

[68] N. R. De Tacconi and K. Rajeshwar, “Semiconductor nanostructures in an alumina template matrix: Micro- versus macro-scale photoelectrochemical behavior,” *Electrochim. Acta*, vol. 47, no. 16, pp. 2603–2613, 2002.

[69] G. D. Sulka, L. Zaraska, and W. J. Stępniowski, “Anodic porous alumina as a template for nanofabrication,” *Encycl. Nanosci. Nanotechnol.*, vol. 11, no. March 2016, pp. 261–349, 2011.

[70] M. A. Noginov and V. A. Podolskiy, *Tutorials in Metamaterials*. CRC Press, 2012.

[71] R. Sutherland, *Handbook of Nonlinear Optics*, 2nd ed. Marcel Dekker, 2003.

[72] Y. Ma, X. Li, and L. Tong, “Direct measurements of propagation losses in silver nanowires,” *Opt. Lett.*, vol. 35, no. 8, pp. 1160–1162, 2010.

[73] J. D. Bierlein and H. Vanherzeele, “Potassium titanyl phosphate: properties and new applications,” *J. Opt. Soc. Am. B*, vol. 6, no. 4, p. 622, 1989.

[74] U. Heitmann, M. Kötteritzsch, S. Heitz, and A. Hese, “Efficient generation of tunable VUV laser radiation below 205 nm by SFM in BBO,” *Appl. Phys. B Photophysics Laser Chem.*, vol. 55, no. 5, pp. 419–423, 1992.

[75] K. Moutzouris *et al.*, “Second-harmonic generation through optimized modal phase matching in semiconductor waveguides,” *Appl. Phys. Lett.*, vol. 83, no. 4, pp. 620–622, 2003.

[76] S. Ducci, L. Lanco, V. Berger, A. De Rossi, V. Ortiz, and C. M, “Continuous-wave second-harmonic generation in modal phase matched semiconductor waveguides,” *Appl. Phys. Lett*, vol. 84, no. 16, pp. 2974–2976, 2004.

[77] Y. Song, K. Choi, D.-H. Jun, and J. Oh, “Nanostructured GaAs solar cells via metal-assisted chemical etching of emitter layers,” *Opt. Express*, vol. 25, no. 20, p. 23862, 2017.

[78] M. Dejarld *et al.*, “Formation of high aspect ratio GaAs nanostructures with metal-assisted chemical etching,” *Nano Lett.*, vol. 11, no. 12, pp. 5259–5263, 2011.

[79] H. Asoh, Y. Suzuki, and S. Ono, “Metal-assisted chemical etching of GaAs using Au catalyst deposited on the backside of a substrate,” *Electrochim. Acta*, vol. 183, pp. 8–14, 2015.

[80] Z. L. Mei, J. Bai, and T. J. Cui, “Gradient index metamaterials realized by drilling hole arrays,” *J. Phys. D. Appl. Phys.*, vol. 43, no. 5, 2010.

[81] SYNOPSYS, “RSoft FullWave User Guide,” V. 2019.03., 2019.

[82] SYNOPSYS, “RSoft CAD User Guide,” V. 2019.03., 2019.

Appendix A

FDTD Simulations Using RSoft Tool

The finite-difference time-domain (FDTD) technique is the FullWave® simulation tool of RSoft® Component Design Suite. It computes electromagnetic fields inside a structure as a function of time and space as a response to electromagnetic excitation. In this work, version v2019.03 of the FullWave® was used [81], [82].

A.1 Drawing Structure

A new design starts by clicking on the "RSoft CAD Layout" icon. Select "File" and then "New" from the taskbar menu. The "Startup Window", as shown in Fig. A.1, will then open. Select "FullWave" and "2D" (two-dimensional) in this window and click "OK". A new window will open with a different taskbar menu, as shown in Fig. A.2. Click on "Utility" to open a smaller inset window, where you can select "Array Layout".

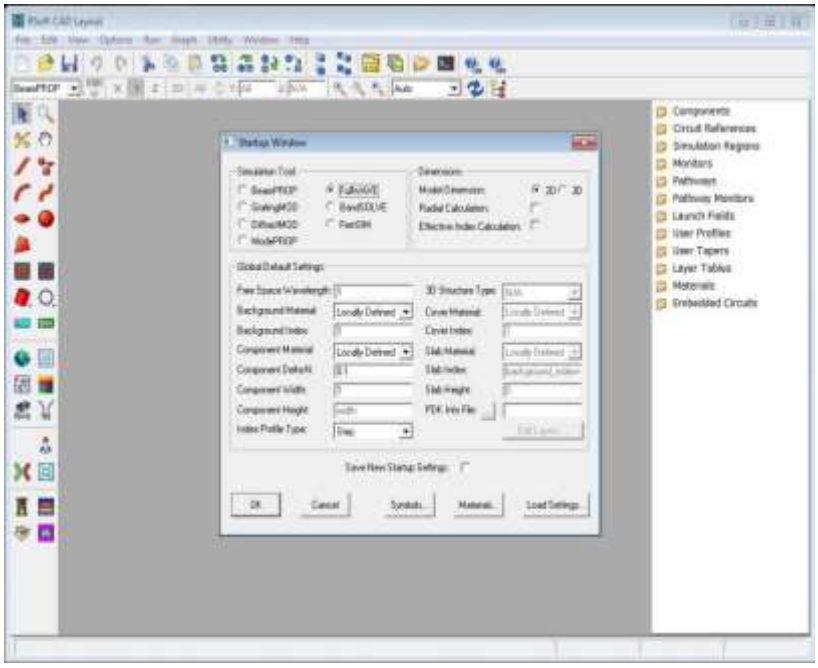

Figure A.1: Window starting new design.

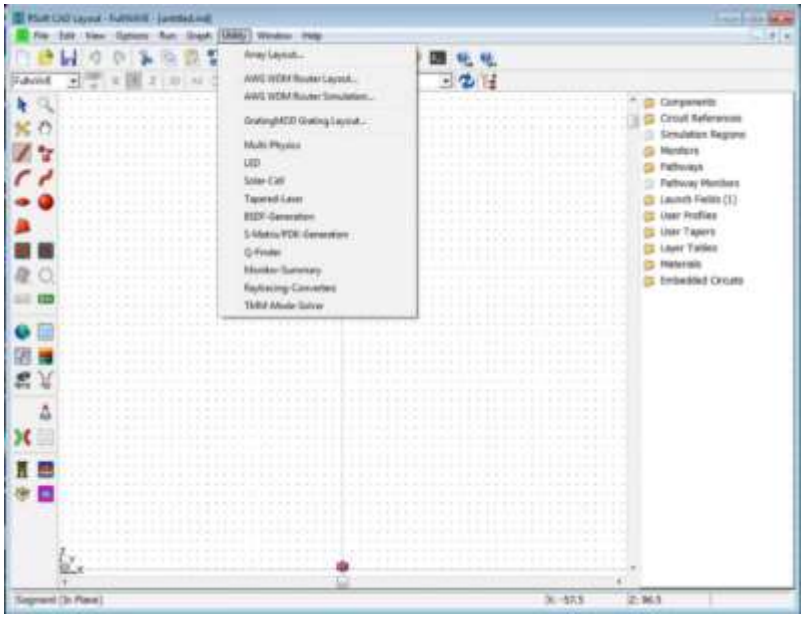

Figure A.2: Layout window for new design.

.

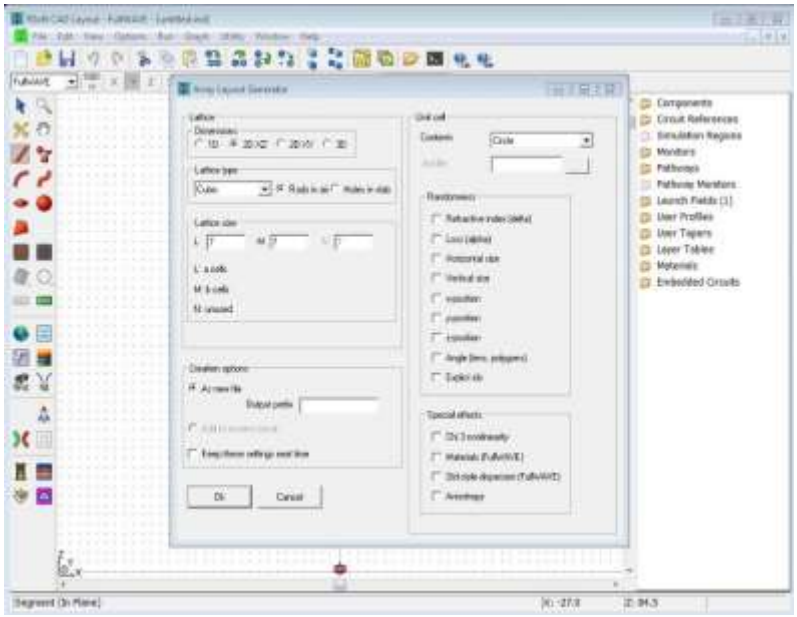

Figure A.3: Array layout generator.

Figure A.3 shows the “Array Layout Generator” window, where you can edit the size and type of the array’s lattice. Our case is a 2D array of size L × M in the X and Z directions. Cubic lattice of size 33 × 33 and cylindrical shape elements were selected. “Thesis” is the name given to the new design. The name is written in the space at the bottom of the

window. After writing the name of the design and hitting “OK”, a window appears displaying the top view of the array’s layout, as shown Fig. A.4. Inserting the geometrical parameters and the materials properties is a crucial step in the design. RSoft has many material properties in its library, but material can also be added to the library. In the left toolbar, there is an icon to insert the geometrical parameters of the structure, such as the array period and cylindrical element radius.

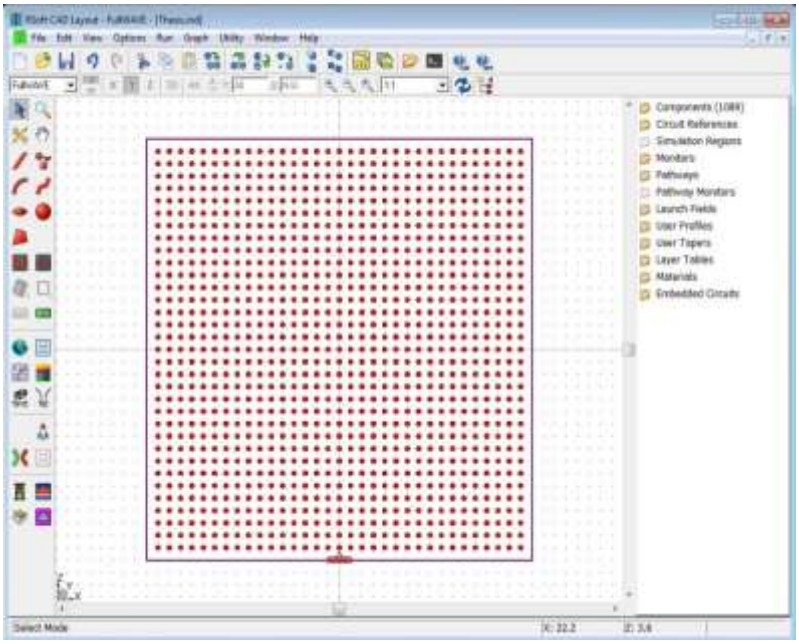

Figure: A.4: Top view of size 33×33 cubic lattice and cylindrical shape elements.

A.2 Adding Material

Adding new material to the library of the FullWave is supported by RSoft. Specifically, RSoft supports dispersive, anisotropic, and second-order nonlinear materials.

Clicking on the “Edit Material” icon on the left toolbar will open a window where you can add new material, as shown in Fig. A.5. Select “New Material” and give a name to the material to be added. In the same window is the icon “Import NK Data”, where you can upload the material data. The data should be in three columns: the first column is for wavelength; the second is for refractive index (N); and the third is for absorption index (K). We used this feature to add experimental measured data of gallium arsenide (GaAs) and

silver (Ag) to the library. Theoretical data for GaAs and Ag are already in the library, but our goal is to use experimental data.

Figure A.5: Adding new material to RSoft library.

A.3 Run Simulation

To run the simulation, an excitation field must be applied to the structure. In the right toolbar, click on the "Launch Field" folder to open a window where you can add and edit excitation field parameters such as location, type, frequency, or orientation. In our case, we used a "Pulsed" and "Plane Wave" field, as shown in the bottom of the structure in Fig. A.6.

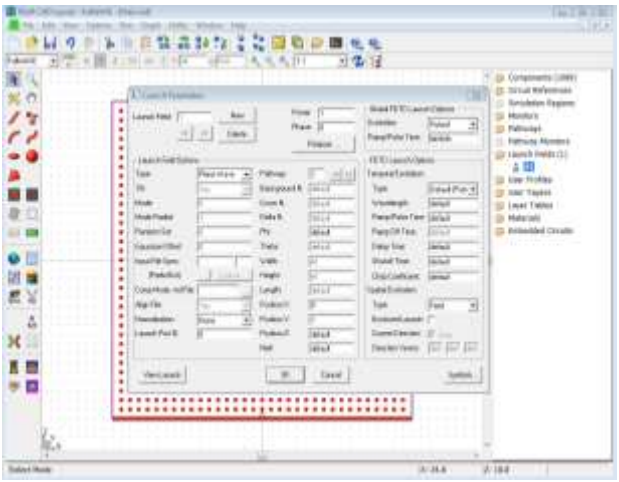

Figure A.6: Window showing addition of excitation field.

Further, because we are interested in finding the *S*-parameters of the structure, S_{11} and S_{21}, we added two ports to the top and bottom of the structure to compute the S-parameters,

as shown in Fig. A.7. Prior to starting the simulation, the boundary conditions of the structure should be defined. In our case, we applied a periodic boundary condition along the direction perpendicular to the wave propagation (x axis), while a perfectly matched layer (PML) boundary condition was applied at the end of the wave propagation direction (z axis). Based on the retrieving techniques of computing *S*-parameters [50], [51] to use a thin layer of structures to compute the *S*-parameters, a unit-cell was selected. It maintained the same boundary conditions mentioned above, as shown in Fig. A.8.

The simulation starts by clicking on the simulation icon on the left toolbar. A new window will open for editing the simulation parameters, as shown in Fig. A.9. In this window, you can select grid size, field polarization, enabling or disabling dispersive/nonlinearity properties, excitation field type, output display, boundary conditions, and more. Please refer to reference [81] for more details on how to edit simulation parameters.

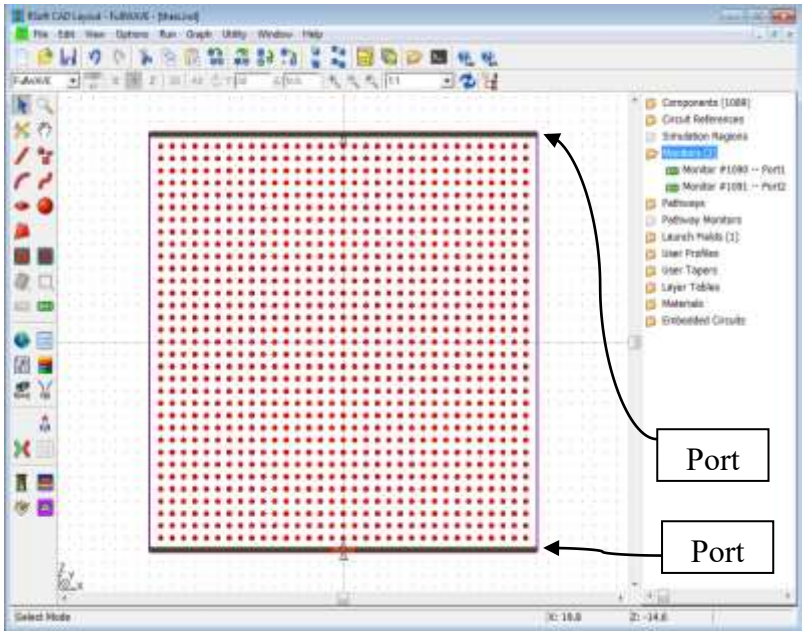

Figure A.7: Adding two ports to compute *S*-parameters.

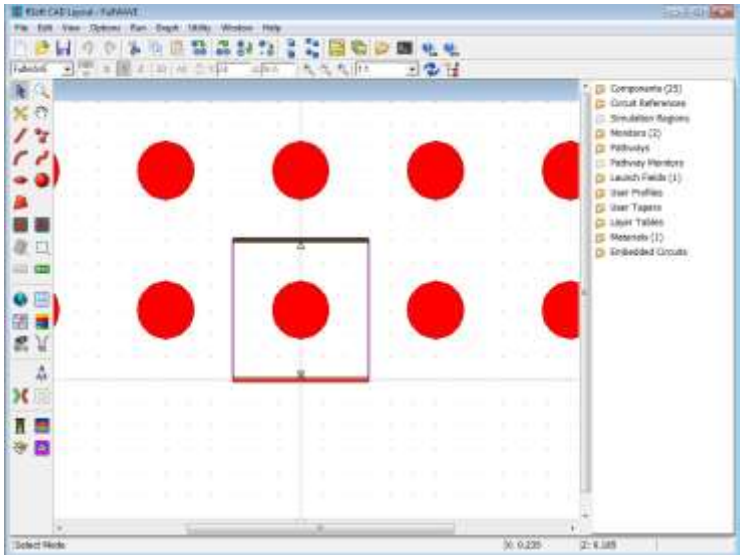

Figure A.8: Unit cell of structure.

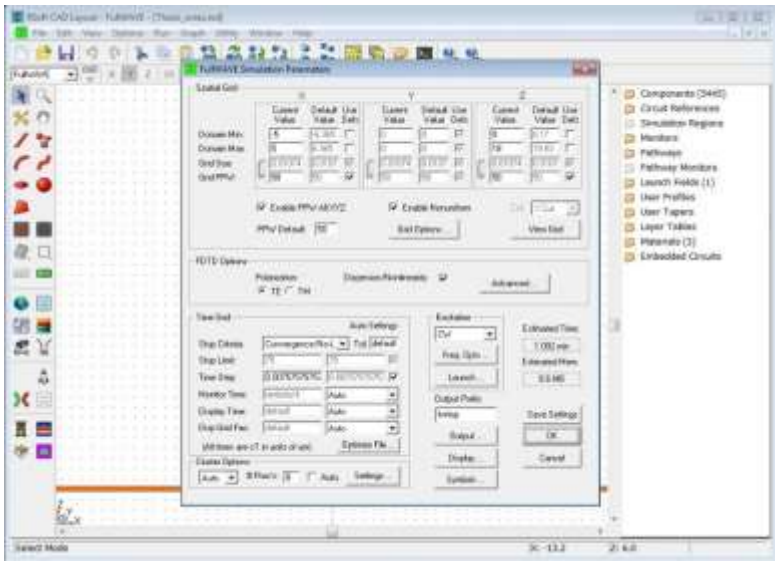

Figure A.9: Window to edit simulation parameters.

The simulation results are usually in file distribution, but you can obtain data of the *S*-parameters if you insert the two ports at the end of the structure, as shown in Fig. A. 7. The *S*-parameters files will be saved in the directory where the RSoft was installed, as shown in Fig. A.10. The files, thesis_port1_olap and thesis_port2_olap, are data files in text

format for S_{11} and S_{21}, respectively. These data can be transferred to MATLAB to compute the refractive indices.

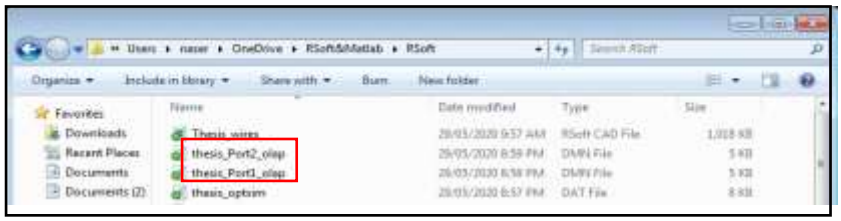

Figure: A.10: Files of *S*-parameters data.

.

Appendix B

MATLAB Codes for The Wire Medium -Drude Model

```
clc;
clearvars;
% Constants ----------------------------------------
prompt = 'What is value of x? x=1(no=1,n2=GaAs),x=2(no=GaAs,n2=GaAs , x=3 (no=n2=1)) ';
x=input(prompt); % x is the boundaries of the slab structure
prompt = 'What is value of d? ';
d = input(prompt); % “d” is the wire period
prompt = 'What is value of r? ';
r = input(prompt); % “r” is the wire radius
prompt = 'What is value of z? ';
z=input(prompt); % “z “is the slab thickness
prompt = 'What is value of kk?';
kk=input(prompt); % “kk” is the iteration loop number
r1=r*10^-9;
d1=d*10^-9;
C=3*10^8;
h=6.63*10^-34;
segma=6.28*10^7;% conductivity of silver
epson=8.8542*10^-12; % permittivity in the free space
%-----------------------------------------------------------------
load GaAs_d1.txt; % reading GaAs data
x1=GaAs_d1(:,1);
y1=GaAs_d1(:,2);
xx1=rot90(x1);
yy1=rot90(y1);
%---------------------------------------
% GaAs and Au optical properties for W3
% (1) GaAs
 ev_GaAs_3=xx1;
 n_GaAs_x_3=yy1;
 naser1=xx1;
 naser2=fliplr(naser1);
 o=naser1+naser2;
 %w1 calculations
ev1=fliplr(xx1);
GaAs1= fliplr(yy1);
prompt = 'What is value of value of n , ev_1(n)? ';
n=input(prompt);
ev_1=ev1(n);
n_GaAs_1=GaAs1(n);
```

```
eGaAs_1=n_GaAs_1^2;
landa_1=1.24./ev_1;
w1=2*pi*C*10^6./landa_1;
gama=(1i*epson*2*pi*(C^2))/(segma*(pi*r1^2)*log(d1/r1));
wp_s=2*pi*(C^2)./((d1^2)*eGaAs_1*log(d1/r1));
effz=eGaAs_1*(1-(wp_s/(w1*(w1+gama))));
neffz=real(sqrt(effz));
keffz=imag(sqrt(effz));
% Interpolation
 % (1) GaAs
 % w3 calculations
  ev_3=linspace(0.07,ev_1-0.07,kk);
  landa_3=(1.24./ev_3);
  w3=2*pi*C*10^6./landa_3;
n_GaAs_3=interp1(ev_GaAs_3,n_GaAs_x_3,ev_3,'spline');
 %-----------------------------------------------
  % w2 calculations
 ev_2=fliplr(ev_3);
 landa_2=(1.24./ev_2);
 w2=2*pi*C*10^6./landa_2;
 n_GaAs_2=fliplr(n_GaAs_3);
%----------------------------------
beta1=neffz*(w1/C);
beta2= n_GaAs_2.*(w2/C);
beta3= n_GaAs_3.*(w3/C);
fy=(beta1-beta3-beta2)./beta1;
%----------------------
% Transfer Matrix Method
% Loss Calculations
ev=linspace(1.24,0.07,kk);
GaAs=interp1(ev1,GaAs1,ev,'spline');
eGaAs=GaAs.^2;
landa=(1.24./ev);
w=2*pi*C*10^6./landa;
gama=(1i*epson*2*pi*(C^2))/(segma*(pi*r1^2)*log(d1/r1));
wp_s=2*pi*(C^2)./((d1^2)*eGaAs*log(d1/r1));
landa_p=(2*pi*C*10^6)./sqrt(wp_s);
ez=eGaAs.*(1-(wp_s./(w.*(w+gama))));
ne=real(sqrt(ez));
ke=imag(sqrt(ez));
n1=ne-ke*1i;
alpha=(4*pi.*ke)./landa;
if x==1
n2=GaAs;
no=1;
elseif x==2
```

```
no=GaAs;
n2=GaAs;
else
   no=1.00;
   n2=1.00;
end
delta=(1i*2*pi*z*n1)./(landa);
dem=(no+n1).*(n1+n2).*exp(delta)+(no-n1).*(n1-n2).*exp(-delta);
rr=((no-n1).*(n1+n2).*exp(delta)+(no+n1).*(n1-n2).*exp(-delta))./dem;
tt=(4.*no.*n1)./dem;
R=abs(rr.^2);
T=abs(tt.^2);
A=1-R-T
 plot(landa_3,fy); hold on ; title('phase mismatch');figure; plot(landa,T)
title('Transmssion');figure; plot(landa,A);title('absorption')
figure;plot(landa,R);title('Reflection ')
figure;plot(landa,ne) ;title('real_permitivity');hold on
figure
plot(landa,ke)
plot(landa,alpha)
match=fy;
for nn=1:kk-1
   if match(nn+1)>=0 && match(nn)<=0
      nx=nn;
      kp=keffz;
      np=neffz ;
      ns=n_GaAs_2(nx);
      ni=n_GaAs_3(nx);
      landa_3_m=(landa_3(nn+1)+landa_3(nn))./2;
       landa_2_m=(landa_1*landa_3_m)/(landa_3_m-landa_1);
       ev_m_3=1.24/landa_3_m;
       ev_m_2=1.24/landa_2_m;
      ev_m_1= ev_m_2+ev_m_3;
   end
end
```

Appendix C

MATLAB Codes for The Effective Medium Theory

```
clc;
clearvars;
% Constants
prompt = 'What is value of kk?';
kk=input(prompt);
q=0.0;
C=3*10^8;
prompt = 'What is value of r? ';
r = input(prompt);
prompt = 'What is value of d? ';
d = input(prompt);
ff=pi*(r^2/d^2);
rr=2*pi*r;
load GaAs_d1.txt;
x1=GaAs_d1(:,1);
y1=GaAs_d1(:,2);
y2=GaAs_d1(:,3);
y3=GaAs_d1(:,4);
xx1=rot90(x1);
yy1=rot90(y1);
yy2=rot90(y2);
yy3=rot90(y3);
%---------------------------------------
    ev_GaAs_3=xx1;
    n_GaAs_x_3=yy1;
% (2) Au
   ev_Au_3=xx1;
   n_Au_x_3=yy2./yy2;
   k_Au_x_3=0.0*yy3;
 %-----------------------------------------
 ev1=fliplr(xx1);
GaAs1= fliplr(yy1);
 for n=1:90
ev_1=ev1(n);
n_GaAs_1=GaAs1(n);
eGaAs_1=n_GaAs_1^2;
landa_1=1.24./ev_1;
w1=2*pi*C*10^6./landa_1;
landa_1_n=landa_1.*10^3;
dpfxy_1= 0.5 -((2/9)*(rr./landa_1_n).^3)*1i;
n_Au_1=1.0;
```

```
k_Au_1=0.0;
N_Au_1=n_Au_1+1j*k_Au_1;
emetalyz1=(N_Au_1).^2;
eGaAsyz1=(n_GaAs_1).^2;
zz1=(emetalyz1-eGaAsyz1);
effyz1=eGaAsyz1+((ff*eGaAsyz1.*zz1)./(eGaAsyz1+dpfxy_1.*(1-ff)*zz1));
neffyz1=real(sqrt(effyz1));
 %  Interpolation
 % w3
ev_3=linspace(0.07,ev_1-0.07,kk);
landa_3=(1.24./ev_3);
w3=2*pi*C*10^6./landa_3;
n_GaAs_3=interp1(ev_GaAs_3,n_GaAs_x_3,ev_3);
n_Au_3=interp1(ev_Au_3,n_Au_x_3,ev_3);
k_Au_3=interp1(ev_Au_3,k_Au_x_3,ev_3);
N_Au_3=complex(n_Au_3,k_Au_3);
landa_3_n=landa_3.*10^3;
dpfxy_3= 0.5 -((2/9)*(rr./landa_3_n).^3)*1i;
emetalx_w3=(N_Au_3).^2;
eGaAsx_w3=(n_GaAs_3).^2;
z=(emetalx_w3-eGaAsx_w3);
effx_w3=eGaAsx_w3+((ff*eGaAsx_w3.*z)./(eGaAsx_w3+dpfxy_3.*(1-ff).*z));
neffx_w3=real(sqrt(effx_w3));
keffx_w3=imag(sqrt(effx_w3));
  % w2
ev_2=fliplr(ev_3);
landa_2=(1.24./ev_2);
w2=2*pi*C*10^6./landa_2;
n_GaAs_2=fliplr(n_GaAs_3);
N_Au_2=fliplr(N_Au_3);
emetalx_w2=(N_Au_2).^2;
eGaAsx_w2=(n_GaAs_2).^2;
effx_w2=(1-ff)*eGaAsx_w2+ff*emetalx_w2;
neffx_w2=real(sqrt(effx_w2));
beta1=neffyz1*(w1/C);
beta2=neffx_w2.*(w2/C);
beta3=neffx_w3.*(w3/C);
fy=(beta1-beta3-beta2)./beta1;
figure;plot(ev_3,fy);plot(landa_3,fy); hold on ;plot(landa_3, real(effx_w3))
figure;plot(landa_3,imag(effx_w3));plot(landa_2,real(effx_w2));figure;
plot(landa_2,imag(effx_w2));plot(landa_3,fom);figure
plot(landa_3,imag(emetalx_w3)); figure
if n== 1
plot(landa_2,neffx_w2,landa_3,neffx_w3);
figure;plot(landa_2,n_GaAs_2);
end
```

```
plot(landa_3,neffx_w3,landa_2,neffx_w2,landa_3,n_GaAs_3);
figure;plot(landa_3,neffx_w3);hold on;plot(landa_2,neffx_w2);
loss=real(effx_w3)./imag(effx_w3);
loss=keffx_w3./neffx_w3;
figure;plot(landa_3,imag(effx_w3))
match=fy;
for nn=1:kk-1
   if match(nn+1)>=0 && match(nn)<=0
       q=q+1;
      l3(q)=(landa_3(nn+1)+landa_3(nn))./2;
      l2(q)=(landa_1*l3(q))/(l3(q)-landa_1);
      l1(q)=landa_1;
      e3(q)=1.24./l3(q);
      e2(q)=1.24./l2(q);
      e1(q)=e2(q)+e3(q);
   end
end
end
hold off
figure;plot(l1,l3,l1,l2)
Amax=max(l1);
Amin=min(l1);
%----------------------
l1_x=Amin:0.001:Amax;
l2_x=interp1(l1,l2,l1_x,'spline');
l3_x=interp1(l1,l3,l1_x,'spline');
g=1;
while l2_x(g)<l3_x(g)
   L2(g)=l2_x(g);
   L3(g)=l3_x(g);
   L1(g)=l1_x(g);
   g=g+1;
end
plot(L1,L3,L1,L2)


      L1=rot90(L1);
L2=rot90(L2);
L3=rot90(L3);
save('L1_GaAs.txt','L1','-ascii');
save('L2_120_25.txt','L2','-ascii');
save('L3_120_25.txt','L3','-ascii');
```

Appendix D

Copyright Permission Letters

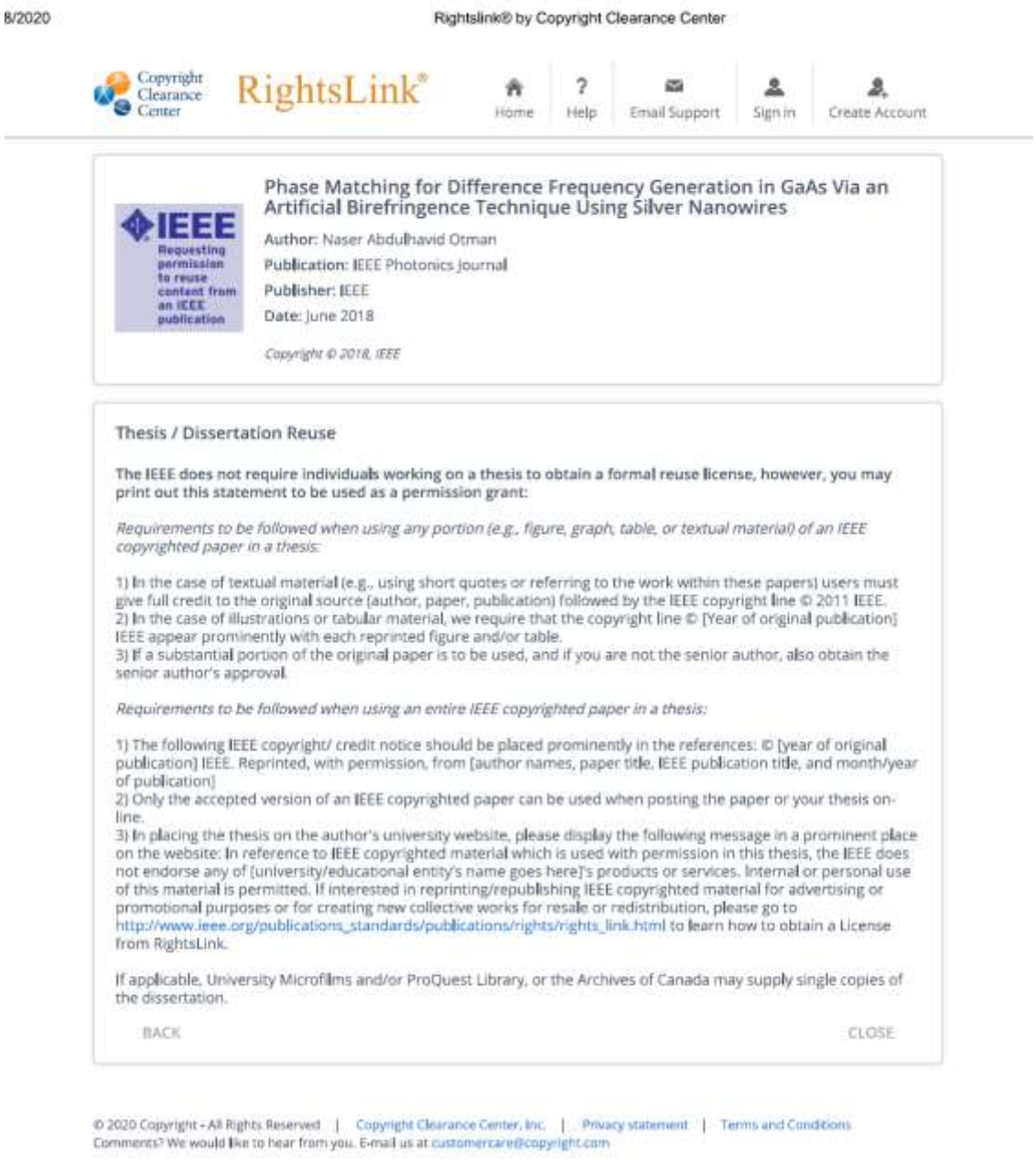

8/2020 Rightslink® by Copyright Clearance Center

Copyright Clearance Center RightsLink®

Home | Help | Email Support | Sign in | Create Account

IEEE Requesting permission to reuse content from an IEEE publication

Phase Matching for Difference Frequency Generation in GaAs Via an Artificial Birefringence Technique Using Silver Nanowires

Author: Naser Abdulhavid Otman

Publication: IEEE Photonics Journal

Publisher: IEEE

Date: June 2018

Copyright © 2018, IEEE

Thesis / Dissertation Reuse

The IEEE does not require individuals working on a thesis to obtain a formal reuse license, however, you may print out this statement to be used as a permission grant:

Requirements to be followed when using any portion (e.g., figure, graph, table, or textual material) of an IEEE copyrighted paper in a thesis:

1) In the case of textual material (e.g., using short quotes or referring to the work within these papers) users must give full credit to the original source (author, paper, publication) followed by the IEEE copyright line © 2011 IEEE.
2) In the case of illustrations or tabular material, we require that the copyright line © [Year of original publication] IEEE appear prominently with each reprinted figure and/or table.
3) If a substantial portion of the original paper is to be used, and if you are not the senior author, also obtain the senior author's approval.

Requirements to be followed when using an entire IEEE copyrighted paper in a thesis:

1) The following IEEE copyright/ credit notice should be placed prominently in the references: © [year of original publication] IEEE. Reprinted, with permission, from [author names, paper title, IEEE publication title, and month/year of publication]
2) Only the accepted version of an IEEE copyrighted paper can be used when posting the paper or your thesis on-line.
3) In placing the thesis on the author's university website, please display the following message in a prominent place on the website: In reference to IEEE copyrighted material which is used with permission in this thesis, the IEEE does not endorse any of [university/educational entity's name goes here]'s products or services. Internal or personal use of this material is permitted. If interested in reprinting/republishing IEEE copyrighted material for advertising or promotional purposes or for creating new collective works for resale or redistribution, please go to http://www.ieee.org/publications_standards/publications/rights/rights_link.html to learn how to obtain a License from RightsLink.

If applicable, University Microfilms and/or ProQuest Library, or the Archives of Canada may supply single copies of the dissertation.

BACK CLOSE

© 2020 Copyright - All Rights Reserved | Copyright Clearance Center, Inc. | Privacy statement | Terms and Conditions
Comments? We would like to hear from you. E-mail us at customercare@copyright.com